Fast Quantitative Microwave Imaging Based on Calibration Measurements

FAST QUANTITATIVE MICROWAVE IMAGING BASED ON CALIBRATION MEASUREMENTS

By

Sheng Tu, M.Sc., B.Sc.

A Thesis
Submitted to the School of Graduate Studies
in Partial Fulfillment of the Requirements
for the Degree
Doctor of Philosophy

McMaster University

DOCTOR OF PHILOSOPHY (2015) McMASTER UNIVERSITY
(Electrical and Computer Engineering) Hamilton, Ontario

TITLE: **Fast Quantitative Microwave Imaging Based on Calibration Measurements**

AUTHOR: Sheng Tu
M. Sc.
School of Electric Engineering
(Xidian University, Xi'an, Shaanxi, China)

SUPERVISORS: N. K. Nikolova, Professor
Ph. D. (University of Electro-Communications)
Canada Research Chair in High Frequency Electromagnetics
Fellow, IEEE
Fellow, Canadian Academy of Engineering
P. Eng. (Ontario)

John W. Bandler, Professor
D. Sc. (Eng.) (University of London)
Life Fellow, IEEE
Fellow, IET
Fellow, EIC
Fellow, Royal Society of Canada
Fellow, Canadian Academy of Engineering
P. Eng. (Ontario)

Matiar R. Howlader, Adjunct Assistant Professor
Ph. D. (Kyushu University)

NUMBER OF PAGES: XIX, 144

ABSTRACT

This thesis contributes to the solution of the inverse electromagnetic (EM) scattering problems arising in microwave imaging. A calibration technique based on measurements of specific objects is proposed and a fast quantitative imaging method based on such measurements is developed.

The calibration measurements are performed on two known objects: the reference object representing the scatterer-free measurement and the calibration object representing a small scatterer embedded in the reference object. The inversion method does not need analytical or numerical approximations of the forward model as those are replaced by the measurement-based model. It is particularly valuable in short-range imaging, where analytical models of the incident field do not exist while the fidelity of the simulation models is often inadequate. In this thesis, it is demonstrated that the implementation of the calibration technique in the sensitivity-based imaging improves both the imaging efficiency as well as the image quality.

A quantitative imaging method is further developed based on the calibration measurements where a direct inversion in real space is employed. The electrical properties of dielectric objects are reconstructed using a resolvent kernel in the

forward model, which is extracted from the calibration measurements. The experimentally determined resolvent kernel inherently includes the particulars of the measurement setup, including all transmitting and receiving antennas. The inversion is fast, allowing for quasi-real-time image reconstruction.

The theoretical limitations of the fast quantitative imaging method have been investigated and its performance with noisy data has been examined. It is found that the proposed method has limitations which are more flexible than those of the linear Born model. The method is also robust to random noise.

Both the calibration technique and the fast quantitative imaging method are validated through synthetic, simulation and/or experimental examples. The proposed concept of experimentally derived resolvent kernel in the forward model is general and may be valuable in other imaging modalities such as ultrasound, photonic imaging, electrical-impedance tomography, etc.

ACKNOWLEDGEMENTS

First and foremost, I would like to express my sincere appreciation and thanks to my supervisor, Dr. Natalia K. Nikolova. Her expert guidance and advice on both my research and career have been priceless. I could not have imagined having a better mentor for my Ph.D. studies. It has been my great honor to work with her, and I will always be thankful for her remarkable wisdom and continuous support.

I would also like to thank my co-supervisors, Dr. John W. Bandler and Dr. Matiar R. Howlader, as well as my committee members, Dr. Aleksandar Jeremic, Dr. Thomas E. Doyle and Dr. Qingsha S. Cheng, for their insightful comments and stimulating discussions throughout my Ph.D. program.

I am also grateful to my colleagues in our Computational Electromagnetics Research Laboratory. Special thanks go to Dr. Yifan Zhang and Justin McCombe for sharing their expertise and assisting with the experiments. Many thanks go to my other friends as well, Dr. Li Liu, Dr. Reza Amineh, Dr. Kaveh Moussakhani, Massoud Ghassemi, Yona Baskharoun, Mohamed H. El Sherif, Sadegh Dadash, Haohan Xu, Yu Zhang, Jeff Thompson, Denys S. Shumakov, and Alex Beaverston, who have made my long journey joyful.

Words cannot express how grateful I am to my parents for all of their encouragements, sacrifices and unwavering supports. Finally, I would like to thank my dear friends, James Jiang, Quentin Shao and Janice He, for being by my side and making my life worth living.

Contents

List of Figures

List of Abbreviations

2D	Two Dimensional
3D	Three Dimensional
CO	Calibration Object
EM	Electromagnetic
GWN	Gaussian White Noise
LN	Localized Nonlinear
LS	Least Square
LU	Lower Upper
MoM	Method of Moments
MRI	Magnetic Resonance Imaging
OUT	Object Under Test
PSF	Point-Spread Function
QA	Quasi-Analytic
RO	Reference Object
RRMSE	Relative Root-Mean-Square Error
Rx	Receiving
SNR	Signal to Noise Ratio
TEM	Transverse Electromagnetic

Tx	Transmitting
VNA	Vector Network Analyzer

Chapter 1

INTRODUCTION

1.1 MOTIVATION

The ability of microwaves to penetrate many optically opaque mediums such as living tissue, wood, ceramics, soil, fog, etc., has been utilized in imaging dielectric bodies for decades. The *long-range* techniques of microwave radar have been widely applied in civilian and military applications for remote sensing as well as target detection and tracking [1]-[4].

Recently, active microwave imaging has been extensively studied in a variety of *short-range* applications such as medical diagnostics, through-the-wall imaging, concealed weapon detection, nondestructive testing, etc., [5]-[13]. The terminology "short-range" indicates that, opposite to the long-range, the inspected object is relatively close to the microwave source and the sensing antennas, i.e., at a distance comparable or smaller than at least one of the following three measures: (i) the target's size, (ii) the size of the antenna or the sensor array, and (iii) the wavelength. Short-range imaging is also referred to as the *near-field* imaging.

The microwave imaging methods have shown their potential in a number of emerging applications. For instance, microwave imaging is a candidate of an alternative imaging modality for breast cancer detection where the current common screening modality is mammography (often supplemented by ultrasound). An alternative is needed because mammography suffers from low sensitivity, involves ionizing radiation exposure as well as patient discomfort [8]-[10]. Through-the-wall microwave imaging is considered promising in military, security and civilian applications such as the knock-and-announce missions on the urban battlefield, the rescue missions after earthquake and avalanche, etc., [11]. Also, the security checks at the airport and other public places are expected to become more comfortable and convenient for examinees by employing microwave equipment and devices [12]. Most of the applications would benefit from an imaging system which features compact size, low cost, and real-time performance while at the same time generating high-quality images.

Microwave imaging research covers a wide range of subjects from hardware design to the reconstruction algorithms. The former involve various topics such as antenna and circuit design, sensor arrangement, data-acquisition approach and calibration approaches, SNR (signal-to-noise ratio) reduction, etc., [14]-[20]. The focus of the later is on the forward model of electromagnetic (EM) scattering and the problem of inverse scattering [21]-[33]. The associated reconstruction algorithm constitute the core of imaging methods.

The task of microwave imaging is to reconstruct the dielectric properties of the imaged region as a function of position. The dielectric properties of interest are, for example, the real and imaginary parts of the complex permittivity. In *quantitative imaging*, these functions yield values that estimate the actual property distributions in the imaged region. In contrast, *qualitative imaging* is only able to localize abnormalities, i.e., regions where the properties differ from those in the normal state of the object, and to estimate their shape.

Among the quantitative methods, the Born iterative methods [22]-[23] and the model-based optimization methods [7] are the most common in microwave near-field imaging. All of these methods employ iterative strategies where numerical forward models, e.g., simulations, are updated to match the measured data. Thus, the reconstruction is often time-consuming and its convergence is critically dependent on the fidelity of the forward model. In the near-field imaging of complex objects such as tissues, luggage or structural components, achieving adequate fidelity of the forward model is particularly challenging [24]. The numerical accuracy of the solution, which can be ensured by proper discretization strategies, is not the only factor. Most critically, the model fidelity depends on the complete representation of the acquisition setup, a representation that is always limited by factors such as fabrication tolerances, electromagnetic interference, positioning errors of mechanical nature, environmental impact, etc. Errors in the forward model, both systematic and

stochastic, add to the system uncertainties and have a detrimental impact on the inverse-problem solution similar to that of noise in the measured data.

The qualitative reconstruction methods employed in active microwave imaging include holographic [25]-[29], confocal [15], [30]-[31], sensitivity-based [32]-[33], as well as time-reversal methods [34]-[36]. Since these methods employ linearized scattering models, typically based on the Born approximation [21], their applicability is limited and their formulation does not allow for quantitative reconstruction. On the other hand, they offer direct inversion with fast processing, typically in real time.

A major hindrance to the application of the direct inversion methods in near-field imaging is the assumption that the incident field and/or the Green function are in the form of a plane, cylindrical or spherical wave. Such analytical models are rarely valid in near-field imaging where the inspected object is in the near zone of the transmitting and receiving antennas and where the background medium is rarely vacuum. In [27]-[29] and [32]-[33], this limitation is overcome by making use of simulation models of the incident field and the Green function distributions in the imaged volume. Note that it is the product of these two distributions, which is needed in the inversion. Unfortunately, the fidelity of the simulation models, although significantly better than the analytical approximations, may also be questionable for the same reasons as the simulations used in the optimization-based reconstruction methods. Moreover, the incident-field simulation models do not

change the fact that the near-field methods of [27]-[29] and [32]-[33] employ the linear Born approximation and are, therefore, limited to applications with weak scattering.

To solve the problem of modeling errors, this thesis proposes a calibration technique for the sensitivity-based microwave imaging, which directly acquires the desired incident-field information from measurements. This eliminates the need for analytical and/or simulation models which may have insufficient fidelity. Besides a baseline measurement of the known *reference object* (RO), the calibration technique requires additional measurements of known *calibration objects* (CO). Here, the RO is the known environment formed by the background medium and the acquisition system. The CO is the same as the RO except for containing an electrically small ("point") scatterer, the property contrast of which is known as well. The proposed calibration technique is validated through an implementation with the qualitative sensitivity-based imaging method in examples using synthetic response data and experimental data, respectively.

It is shown in this thesis that, the acquired response with the CO is the system point-spread function (PSF). In the context of scattering, it is the product of the RO's Green function, the total field at the point scatterer and the known contrast of the point scatterer. The total field, in turn, is very accurately represented by the localized nonlinear approximation [37]. Thus, the point scatterer in the CO effectively serves as a scattering probe inside the RO that provides sampling of the resolvent kernel of

the scattering problem specific to the acquisition setup. The measured PSF and its respective resolvent kernel characterize the imaging system quantitatively. Moreover, they provide higher fidelity than any analytical or simulation model.

Based on the understanding of the CO, this thesis develops a direct-inversion imaging method, which yields quantitative images while offering real-time performance similar to that of the qualitative approaches [32]-[33]. The quantitative reconstruction becomes possible due to the calibration measurement of the known electrically very small (point) scatterer placed in the RO. As a first-order approximation, the proposed method views the scattering from the *object under test* (OUT) as a convolution of its contrast function with the resolvent kernel. Unlike existing deconvolution techniques, e.g., [38]-[39], here the inversion is performed in real space, i.e., Fourier transforms are not employed. Most importantly, the images are quantitative, which, to our knowledge, is not achieved by any of the existing direct-inversion methods.

The utility of the proposed method is two-fold: (i) fast quantitative solution of weak-scattering problems where multiple scattering is negligible, and (ii) providing a good starting point for an iterative reconstruction of complex targets.

The quantitative imaging method is demonstrated and validated through examples using simulation and experimental data. Its performance with noisy data is examined by adding Gaussian white noise (GWN) to the “noise-free” raw data acquired from simulations. Other imaging modalities, such as ultrasound, photonic

imaging and electrical-impedance tomography, would benefit from the concept of experimentally determined resolvent kernel in the forward model.

1.2 CONTRIBUTIONS

The author has contributed substantially to a number of original developments presented in this thesis. These are briefly described next.

(1) A practical calibration technique for imaging system characterization via measurements of a known CO; published in [40]-[42].

(2) General inversion procedure of sensitivity-based imaging integrated with the calibration technique; published in [41].

(3) Application of the sensitivity-based imaging with measured data of lossy (tissue) phantoms; published in [41].

(4) A novel fast quantitative imaging approach employing experimentally determined resolvent kernel; published in [40][42].

(5) Theoretical limitations of the fast quantitative imaging method; published in [42].

(6) Noise analysis of the fast quantitative imaging method using synthetic noisy data; published in [42].

(7) Simulation models emulating measurements of the RO, the CO and the OUT using planar raster-scanning acquisition system; published in [40][42].

(8) A SNR evaluation method for imaging system using measured data; published in [42].

1.3 OUTLINE OF THE THESIS

This thesis presents: (i) an experimental approach to the characterization of the imaging system via calibration measurements with known objects, (ii) a fast quantitative imaging method based on the calibration measurements, (iii) study of the limitations of the proposed technique, and (iv) study of the method's robustness to random noise.

Chapter 2 starts with a comprehensive review of the original sensitivity-based imaging that relies on the use of analytical or simulation models. The setup of the planar raster-scanning system adopted for data acquisition is described in detail. Subsequently, the calibration technique, which allows for the replacement of the analytical or simulation models with measurements, is presented. The complete imaging-formation procedure is summarized and validated via synthetic and simulation examples. The significance of the reflection signal for the imaging resolution is addressed in the last section of this chapter and is demonstrated via synthetic and experimental examples as well.

Chapter 3 presents the fast quantitative imaging method. The extraction of the resolvent kernel from measurement data is derived by using the localized

nonlinear approximation. The concept of *power map* is defined in this chapter and is derived from the principles of the sensitivity-based imaging approach. The power map is further treated as an initial qualitative imaging result. To obtain quantitative images, the relations between the OUT and CO power maps are cast into a least square (LS) problem, the solution of which yields an estimation of the dielectric-property distribution. Method limitations of the proposed imaging method are also given with theoretical proof. In the end of this chapter, validation examples using simulation data are presented with discussions.

Chapter 4 addresses the impacts of random noise on the performance of the proposed fast quantitative imaging method. The implementation of adding GWN to raw simulation data using a MATLAB function is first explained, followed by the noise analysis via simulation and experimental examples. The SNR of the experimental data acquired with a real imaging system is also evaluated and compared with that of the simulation example. The influence of random noise on the uniqueness of the inverse problem is also investigated via a theoretical expression.

The thesis concludes in Chapter 5 with a summary and suggestions for future research.

REFERENCES

[1] D. M. Pozar, *Microwave Engineering*, 2nd ed., Hoboken, NJ: John Wiley & Sons, Inc., 1998.

[2] J. B. Campbell, *Introduction to Remote Sensing*, 3rd ed., New York: Guilford Press, 2002.

[3] J. D. Taylor (Editor), *Ultra-wideband Radar Technology*, FL: CRC Press, Sept. 2000.

[4] S. Khorram, F. H. Koch, C. F. van der Wiele, and S. A. C. Nelson, *Remote Sensing*, Springer, 2012.

[5] M. Pastorino, *Microwave Imaging*, Hoboken, NJ: John Wiley & Sons, Inc., 2010.

[6] R. W. Y. Habash, *Bioeffects and Therapeutic Applications of Electromagnetic Energy*, Boca Raton, FL: CRC Press, 2008.

[7] K. D. Paulsen, P. M. Meaney, and L. C. Gilman (Eds.), *Alternative Breast Imaging: Four Model Based Approaches*, Springer, 2005.

[8] L. E. Larsen and J. H. Jacobi, *Medical Applications of Microwave Imaging*, New York: IEEE, 1986. N. K. Nikolova, "Microwave imaging for breast cancer," *IEEE Microw. Mag.*, vol. 12, no. 7, pp. 78−94, Dec. 2011.

[9] N. K. Nikolova, "Microwave imaging for breast cancer," *IEEE Microw. Mag.*, vol. 12, no. 7, pp. 78−94, Dec. 2011.

[10] N. K. Nikolova, "Microwave biomedical imaging," *Wiley Encyclopedia of Electrical and Electronics Engineering*, pp. 1−22, Apr. 2014.

[11] M. G. Amin (Editor), *Through-the-Wall Radar Imaging*, Boca Raton, FL: CRC Press, 2011.

[12] A. J. Nanzer, *Microwave and Millimeter-Wave Remote Sensing for Security Applications*, Norwood, MA: Artech House, 2011.

[13] R. Zoughi, *Microwave Non-destructive Testing and Evaluation*, Dordrecht, The Netherlands: Kluwer Academic, 2000.

[14] P. M. Meaney, M. W. Fanning, D. Li, S. P. Poplack, and K. D. Paulsen, "A clinical prototype for active microwave imaging of the breast," *IEEE Trans. Microw. Theory Tech.*, vol. 48, no. 1, pp. 1841−1853, Nov. 2000.

[15] M. Klemm, I. J. Craddock, J. A. Leendertz, A. Preece, and R. Benjamin, "Radar-based breast cancer detection using a hemispherical antenna aray—experimental results," *IEEE Trans. Antennas Propag.*, vol. 57, no.6, pp. 1692−1704, June 2009.

[16] R. K. Amineh, M. Ravan, A. Trehan, and N. K. Nikolova, "Near-field microwave imaging based on aperture raster scanning with TEM horn antennas," *IEEE Trans. Antennas Propag.*, vol. 59, no. 3, pp. 928−940, Mar. 2011.

[17] M. J. Burfeindt, N. Behdad, B. D. VanVeen, and S. C. Hagness, "Quantitative microwave imaging of realistic numerical breast phantoms using an enclosed

array of multiband, miniaturized patch antennas," *IEEE Antennas Wireless Progag. Lett.*, vol. 11, pp. 1626−1629, Oct. 2012.

[18] M. Ostadrahimi, A. Zakaria, J. LoVetri, and L. Shafai, "A near-field dual polarized (TE-TM) microwave imaging system," *IEEE Trans. Microw. Theory Tech.*, vol. 61, no. 3, pp. 1376−1384, Mar. 2013.

[19] M. Bassi, M. Caruso, M. S. Khan, A. Bevilacqua, A.-D. Capobianco, and A. Neviani, "An integrated microwave imaging radar with planar antennas for breast cancer detection," *IEEE Trans. Microw. Theory Tech.*, vol. 61, no. 5, pp. 2108−2118, May 2013.

[20] J. J. McCombe, "Noise reduction in microwave imaging and detection," M.A.Sc., Dept. Elect. Comput. Eng., McMaster Univ., Hamilton, ON, Canada, 2014

[21] W. C. Chew, *Waves and Fields in Inhomogeneous Media*, New York: IEEE Press, 1995.

[22] Y. M. Wang and W. C. Chew, "An iterative solution of the two-dimensional electromagnetic inverse scattering problem," *Int. J. Imag. Syst. Technol.*, vol. 1, no. 1, pp. 100−108, Feb. 1989.

[23] W. C. Chew and Y. M. Wang, "Reconstruction of two-dimensional permittivity distribution using the distorted Born iterative method," *IEEE Trans. Med. Imag.*, vol. 9, no. 2, pp. 218−225, June 1990.

[24] M. Ostadrahimi, P. Mojabi, C. Gilmore, A. Zakaria, S. Noghanian, S. Pistorius, and J. LoVetri, "Analysis of incident field modeling and incident/scattered field calibration techniques in microwave tomography," *IEEE Antennas Wireless Progag. Lett.*, vol. 10, pp. 900−903, Sept. 2011.

[25] D. M. Sheen, D. L. McMakin, and T. E. Hall, "Three-dimensional millimeter-wave imaging for concealed weapon detection," *IEEE Trans. Microw. Theory Tech.*, vol. 49, no. 9, pp. 1581−1592, Sept. 2001.

[26] M. Elsdon, D. Smith, M. Leach, and S. J. Foti, "Experimental investigation of breast tumor imaging using indirect microwave holography," *Microw. Opt. Technol. Letters,* vol. 48, no. 3, pp. 480−482, Mar. 2006.

[27] M. Ravan, R. K. Amineh, and N. K. Nikolova, "Two-dimensional near-field microwave holography," *Inverse Problems*, vol. 26, 055011, 2010.

[28] R. K. Amineh, M. Ravan, N. K. Nikolova, and A. Khalatpour, "Three-dimensional near-field microwave holography using reflected and transmitted signals," *IEEE Trans. Antennas Propag.*, vol. 59, no. 12, pp. 4777−4789, Dec. 2011.

[29] R. K. Amineh, A. Khalatpour, H. Xu, Y. Baskharoun, and N. K. Nikolova, "Three-dimensional near-field microwave holography for tissue imaging," *Int. J. Biomed. Imag.*, article ID 291494, 2012.

[30] E. C. Fear, X. Li, S. C. Hagness, and M. A., "Confocal microwave imaging for breast cancer detection: localization of tumors in three dimensions," *IEEE Trans. Biomed. Eng.*, vol. 49, no. 8, pp. 812−822, Aug. 2002.

[31] H. B. Lim, N. T. T. Nhung, P. E. Li, and N. D. Thang, "Confocal microwave imaging for breast cancer: delay-multiply-and-sum image reconstruction algorithm," *IEEE Trans. Biomed. Eng.*, vol. 55, no. 6, pp. 1697−1704, June 2008.

[32] L. Liu, A. Trehan, and N. K. Nikolova, "Near-field detection at microwave frequencies based on self-adjoint response sensitivity analysis," *Inverse Problems*, vol. 26, 105001, 2010.

[33] Y. Zhang, S. Tu, R. K. Amineh and N. K. Nikolova, "Resolution and robustness to noise of the sensitivity-based method for microwave imaging with data acquired on cylindrical surfaces," *Inverse Problems*, vol. 28, 115006, 2012.

[34] A. J. Devaney, *Mathematical Foundations of Imaging, Tomography and Wavefield Inversion*, Cambridge UK: Cambridge University Press, 2012.

[35] P. Kosmas and C. M. Rappaport, "Time reversal with the FDTD method for microwave breast cancer detection," *IEEE Trans. Microw. Theory Tech.*, vol. 53, no. 7, pp. 2317−2323, July 2005.

[36] P. Kosmas and C. M. Rappaport, “FDTD-based time reversal for microwave breast cancer detection-localization in three dimensions,” *IEEE Trans. Microw. Theory Tech.*, vol. 54, no. 4, pp. 1921−1927, Apr. 2006.

[37] T. M. Habashy, R. W. Groom, and B. R. Spies, “Beyond the Born and Rytov approximations: a nonlinear approach to electromagnetic scattering,” *J. Geophys. Res.*, vol. 98, no. B2, pp. 1759−1775, Feb. 1993.

[38] T. G. Savelyev and A. G. Yarovoy, “Fast image by 3-D deconvolution in short-range UWB radar for concealed weapon detection,” *The 9th European Radar Conf. (EuRAD 2012)*, pp. 26−29, Oct. 2012.

[39] T. Sakamoto, T. G. Savelyev, P. Aubry, and A. G. Yarovoy, “Fast range point migration method for weapon detection using ultra-wideband radar,” *The 9th European Radar Conf. (EuRAD 2012)*, pp. 230−233, Oct. 2012.

[40] S. Tu, Y. Zhang, J. J. McCombe, and N. K. Nikolova, “Sensitivity-based quantitative imaging using planar raster scanning,” *IEEE AP-S/URSI Int. Symp. on Antennas and Propagation*, Memphis, TN, US, July 2014.

[41] S. Tu, Y. Zhang, J. J. McCombe, and N. K. Nikolova, “Sensitivity-based reconstruction in microwave imaging using near-field calibration measurements,” *European Microwave Conference (EuMC) 2014*, Rome, Italy, Oct. 2014.

[42] S. Tu, J. McCombe, D. S. Shumakov and N. K. Nikolova, "Fast quantitative microwave imaging with resolvent kernel extracted from measurements," *Inverse Problem*, vol. 31, 045007, 2015.

Chapter 2

Sensitivity-Based Microwave Imaging Exploiting Calibration Measurements

2.1 INTRODUCTION

Sensitivity-based microwave imaging was first proposed in 2008 by Y. Song *et al.*, who have initially applied self-adjoint sensitivity analysis to the Jacobian calculation in wideband microwave imaging [1]. In 2010, the first qualitative algorithm for sensitivity-based microwave imaging was proposed by L. Liu *et al.* with validation using EM simulations [2]. A study of the imaging resolution achieved with sensitivity-based imaging using data acquired with a circular array has been performed by Y. Zhang *et al.* in 2012. This study indicates that: i) in the far field, the resolution of sensitivity-based microwave imaging is subject to the diffraction limit, and ii) in the near field, the resolution is a fraction of the array radius of the circular data-acquisition system [3].

Sensitivity-based microwave imaging aims to detect targets in a reference object (RO). Both the target and the RO are dielectric, possibly with loss. The RO serves as the known background environment that presents the normal state of the

object under test (OUT) as close as possible. The measurements of both the RO and the OUT acquire the respective response of interest, i.e., the *S*-parameters. The *S*-parameter is referred to as the *reflection signal* when it is acquired with the same antenna serving as receiving (Rx) and transmitting (Tx) antenna, otherwise, it is referred to as the *transmission signal*. The differences between the signals of the RO and the OUT are used to form a response-difference function. With discretization of the imaged volume into image cells, i.e., voxels, the derivatives of the function with respect to the complex permittivity of each voxel are calculated to generate the Jacobian (or Fréchet derivative) maps. The possible abnormalities in the OUT, where the dielectric properties differ from those in the RO, are expected to be localized in those maps.

Real-time computation of the Fréchet derivatives is achieved by applying the self-adjoint sensitivity analysis of the *S*-parameters [4]-[5]. It requires the *a priori* knowledge of the incident-field distributions in the RO, which are caused by every antenna of the data-acquisition system. Note that the self-adjoint sensitivity computation requires the incident field due to not only each Tx antenna but also each Rx antenna when this antenna operates in a transmitting mode. It is common in microwave imaging, sensitivity-based imaging included, that such information is obtained from approximate analytical or EM simulation models.

Unfortunately, the simulation of the field distributions in a realistic near-field acquisition system is usually time intensive. Also, the fidelity of such simulation

models is inadequate in the case of near-field imaging of heterogeneous objects such as living tissue, where analytical models do not exist either. The low fidelity is not because of the numerical errors, which can be reduced at the expense of growing computational demand. It is mostly due to the modeling errors, i.e., the inability to take into account factors such as positioning, manufacturing of the antennas, power leakage, etc. The detrimental impact of the modeling errors on the image quality is similar to that of noise and uncertainties in the measured data.

Here, a calibration technique is proposed to extract the desired incident-field information experimentally. It requires additional measurements of the CO that is the same as the RO except for containing a "point" scatterer. The scatterer has a sufficiently small size with known dielectric properties and location in the RO. The idea of characterizing the data-acquisition system via measurements on a small scatterer has been initially explored in short-range radar [6]-[7]. We have adopted this concept and developed it for the purpose of microwave near-field imaging employing the sensitivity-based method. The proposed calibration technique avoids the troublesome use of analytical and simulation models and provides reliable incident-field information.

The imaging formation calibration technique is explained in the context of planar raster-scanning data-acquisition. The method is validated by examples using synthetic and experimental data. The synthetic data is obtained with an analytical model, while the experimental data acquisition is carried out with a real microwave

planar raster-scanning system based on scattering-parameter measurement with a vector network analyzer (VNA).

2.2 BACKGROUND

2.2.1 Review of sensitivity-based microwave imaging

The classic mathematical model for the scattering problem states that the total field at the observation point is a superposition of the incident field and the scattered field [8]. For a microwave network consist of N_r receivers and N_t transmitters, when the j-th transmitter and the i-th receiver are on, for the m-th frequency f_m, this relationship can be expressed as [8]

$$\mathbf{E}_j^{(m)\mathrm{tot}}(\mathbf{r}_i) = \mathbf{E}_j^{(m)\mathrm{inc}}(\mathbf{r}_i) + \mathbf{E}_j^{(m)\mathrm{sc}}(\mathbf{r}_i),\ \mathbf{r}_i \notin V_\mathrm{s}, \tag{2.1}$$

where $\mathbf{E}_j^{(m)\mathrm{tot}}(\mathbf{r}_i)$ and $\mathbf{E}_j^{(m)\mathrm{inc}}(\mathbf{r}_i)$ are the total and incident electric field vectors observed by the i-th Rx position $\mathbf{r}_i$. $\mathbf{E}_j^{(m)\mathrm{sc}}(\mathbf{r}_i)$ is the scattered electric field due to the scattering volume V_s where the dielectric properties differ from those in the background medium. It is given by the scattering integral [8]:

$$\mathbf{E}_j^{(m)\mathrm{sc}}(\mathbf{r}_i) \approx \int_{V_\mathrm{s}} k_m^2 \Delta\varepsilon^{(m)}(\mathbf{r}')\underline{\mathbf{G}}(\mathbf{r}_i, \mathbf{r}') \cdot \mathbf{E}_j^{(m)\mathrm{tot}}(\mathbf{r}') d\mathbf{r}',\ \mathbf{r}' \in V_\mathrm{s}. \tag{2.2}$$

Here, k_m is the wave number in the background medium at the m-th frequency, $\mathbf{E}_j^{(m)\mathrm{tot}}(\mathbf{r}')$ is the internal total field in the scattering volume V_s, and $\varepsilon^{(m)}$ is the *relative* complex permittivity expressed as

$$\varepsilon^{(m)}(\mathbf{r}') = \varepsilon'^{(m)}(\mathbf{r}') - \mathrm{i}\varepsilon''^{(m)}(\mathbf{r}') . \tag{2.3}$$

In (2.3), the real part $\varepsilon'^{(m)}(\mathbf{r}')$ is the relative permittivity while the imaginary part $\varepsilon''^{(m)}(\mathbf{r}')$ can be expressed in terms of the conductivity $\sigma^{(m)}(\mathbf{r}')$ as $\varepsilon''^{(m)}(\mathbf{r}') = \sigma^{(m)}(\mathbf{r}') / (2\pi f_m \varepsilon_0)$ with ε_0 being the permittivity of vacuum. For brevity, $\varepsilon'^{(m)}(\mathbf{r}')$ is referred to as the *real permittivity*, and $\varepsilon''^{(m)}(\mathbf{r}')$ is the *imaginary permittivity*. $\Delta\varepsilon^{(m)}(\mathbf{r}')$ represents the property difference (or contrast) between the volume V_s and the background medium. $\mathbf{G}(\mathbf{r},\mathbf{r}')$ is the Green's function tensor for the vector Helmholtz equation in this background medium. It satisfies the equation

$$\nabla \times \nabla \times \underline{\mathbf{G}}(\mathbf{r},\mathbf{r}') - k_m^2 \varepsilon'^{(m)} \underline{\mathbf{G}}(\mathbf{r},\mathbf{r}') = \underline{\mathbf{I}}\delta(\mathbf{r}-\mathbf{r}') \tag{2.4}$$

where $\underline{\mathbf{I}}$ is the identity tensor and δ is the Dirac delta function.

On the other hand, according to [2], the electric-field $\mathbf{E}_j^{(m)}(\mathbf{r}_i)$, i.e., the field generated by the j-th transmitter and observed by the i-th receiver, can be related to the measured S-parameter through [2]

$$S_n^{(m)} \equiv \boldsymbol{\rho}_i^{(m)} \cdot \mathbf{E}_j^{(m)}(\mathbf{r}_i) , \tag{2.5}$$

where the S-parameter $S_n^{(m)} \equiv S_{ij}^{(m)}$ corresponds to the n-th signal channel formed by the i-th Rx and the j-th Tx, and $\boldsymbol{\rho}_i^{(m)}$ is the polarization vector of the i-th Rx antenna. The N_r by N_t network provides $N_\mathrm{s} = N_\mathrm{r} \times N_\mathrm{t}$ signals denoted as $S_n^{(m)}$ (n = 1, …, N_s) at each sample frequency f_m (m = 1, …, N_f). When there is no scattering, $\mathbf{E}_j^{(m)}(\mathbf{r}_i) \equiv \mathbf{E}_j^{(m)\mathrm{inc}}(\mathbf{r}_i)$; otherwise, $\mathbf{E}_j^{(m)}(\mathbf{r}_i) \equiv \mathbf{E}_j^{(m)\mathrm{tot}}(\mathbf{r}_i)$. From (2.1), it can be seen that the variation of an S-parameter $S_n^{(m)}$ from its value when there are no scatters is directly related to the scattered field $\mathbf{E}_j^{(m)\mathrm{sc}}(\mathbf{r}_i)$ through [2]

$$\Delta S_n^{(m)} \equiv \boldsymbol{\rho}_i^{(m)} \cdot \mathbf{E}_j^{(m)\mathrm{sc}}(\mathbf{r}_i). \tag{2.6}$$

Let $S_{\mathrm{OUT},\,n}^{(m)}$ and $S_{\mathrm{RO},\,n}^{(m)}$ be the signals of the RO and the OUT measurements, respectively. The sensitivity-based imaging operates on the scattered signals (2.6) for the OUT expressed by

$$\Delta S_{\mathrm{OUT},\,n}^{(m)} = S_{\mathrm{OUT},\,n}^{(m)} - S_{\mathrm{RO},\,n}^{(m)}. \tag{2.7}$$

Further, the response-difference function is defined as [2]

$$F^{(m)}\left[\varepsilon_{\mathrm{RO}}^{(m)}(\mathbf{r}')\right] = \frac{1}{N_\mathrm{s}} \sum_{n=1}^{N_\mathrm{s}} \left|\Delta S_{\mathrm{OUT},\,n}^{(m)}\right|^2, \tag{2.8}$$

which is considered as a function with respect to the relative complex permittivity distribution $\varepsilon_{\mathrm{RO}}^{(m)}(\mathbf{r}')$ in the RO. The derivative of (2.8) with respect to the property variable $g^{(m)}(\mathbf{r}')$ ($g = \varepsilon'_{\mathrm{RO}},\ \varepsilon''_{\mathrm{RO}}$) in the RO is calculated by

$$
\begin{aligned}
D_{\mathrm{OUT},\,g}^{(m)}(\mathbf{r}') &= \frac{\partial F^{(m)}}{\partial g^{(m)}(\mathbf{r}')} \\
&= -\frac{1}{N_{\mathrm{s}}}\sum_{n=1}^{N_{\mathrm{s}}} \mathrm{Re}\left\{\left[\Delta S_{\mathrm{OUT},\,n}^{(m)}\right]^{*}\cdot\frac{\partial S_{\mathrm{RO},\,n}^{(m)}}{\partial g^{(m)}(\mathbf{r}')}\right\}\Bigg|_{g=\varepsilon'_{\mathrm{RO}},\,\varepsilon''_{\mathrm{RO}}},
\end{aligned}
\tag{2.9}
$$

where

$$
\frac{\partial S_{\mathrm{RO},\,n}^{(m)}}{\partial g^{(m)}(\mathbf{r}')} = \begin{cases} \kappa^{(m)}\left[\mathbf{E}_{\mathrm{RO},\,i}^{(m)}(\mathbf{r}')\cdot\mathbf{E}_{\mathrm{RO},\,j}^{(m)}(\mathbf{r}')\right]\Big|_{g=\varepsilon'_{\mathrm{RO}}} \\ \mathrm{i}\kappa^{(m)}\left[\mathbf{E}_{\mathrm{RO},\,i}^{(m)}(\mathbf{r}')\cdot\mathbf{E}_{\mathrm{RO},\,j}^{(m)}(\mathbf{r}')\right]\Big|_{g=\varepsilon''_{\mathrm{RO}}} \end{cases}. \tag{2.10}
$$

In (2.9), $\left[\Delta S_{\mathrm{OUT},\,n}^{(m)}\right]^{*}$ is the complex conjugate of $\Delta S_{\mathrm{OUT},\,n}^{(m)}$. In (2.10), $\mathbf{E}_{\mathrm{RO},\,\xi}^{(m)}(\mathbf{r}')$ $(\xi = i,\, j)$ is the incident field at $\mathbf{r}'$ within the RO when the ξ-th antenna transmits. The constant $\kappa^{(m)}$ in the case of a current-density excitation is given as [4]

$$
\kappa^{(m)} = -\mathrm{i}\frac{2\pi f_m \varepsilon_0 \Omega(\mathbf{r}')}{J^{(m)}(\mathbf{r}_j)\Omega(\mathbf{r}_j)}, \tag{2.11}
$$

where $\Omega(\mathbf{r}')$ is the volume of the voxel located at $\mathbf{r}'$ and $\Omega(\mathbf{r}'_j)$ is the volume of the voxel where the current-density excitation $J^{(m)}(\mathbf{r}_j)$ resides. In the case of a port excitation, the constant $\kappa^{(m)}$ has the form [5]:

$$
\kappa^{(m)} = -\mathrm{i}\frac{\omega_m}{2V_i^{\mathrm{inc}}V_j^{\mathrm{inc}}}, \tag{2.12}
$$

where

$$
V_i^{\mathrm{inc}} = \iint_{S_\xi}\left(\mathbf{E}_\xi^{\mathrm{inc}}\times\mathbf{h}_\xi\right)\cdot d\mathbf{s},\ \xi = i,\, j. \tag{2.13}
$$

V_{ξ}^{inc} (ξ=i, j) is the modal magnitude of the incident wave at the ξ-th port. $\mathbf{E}_{\xi}^{\text{inc}}$ is the incident field at the ξ-th port, $\mathbf{h}_{\xi}$ is the dual (or magnetic) modal vector and $\omega_m = 2\pi f_m$.

It is important to note that $D_{\text{OUT},\,g}^{(m)}(\mathbf{r}')$ is a function of the voxel location $\mathbf{r}'$ and it generates the Jacobian map as a qualitative imaging result. Sometimes, the Jacobian map is referred to as the sensitivity map.

The procedure of the sensitivity-based microwave imaging mainly consists of the following steps [3]:

<u>Step 1</u> Compute maps $D_{\text{OUT},\,g}^{(m)}(\mathbf{r}')$ at each frequency f_m (m = 1, 2, …, N_{f}) with (2.9) and (2.10).

<u>Step 2</u> Normalize $D_{\text{OUT},\,g}^{(m)}(\mathbf{r}')$ to obtain the *frequency Jacobian map* $\underset{\cdot}{D}_{\text{OUT},\,g}^{(m)}(\mathbf{r}')$ through

$$\underset{\cdot}{D}_{\text{OUT},\,g}^{(m)}(\mathbf{r}') = \frac{D_{\text{OUT},\,p}^{(m)}(\mathbf{r}')}{\dfrac{1}{N_{\text{s}}}\sqrt{\sum_{n=1}^{N_{\text{s}}}\left|\Delta S_{\text{OUT},n}^{(m)}\right|^2}\sqrt{\sum_{i=1}^{N_{\text{r}}}\sum_{j=1}^{N_{\text{t}}}\left|\mathbf{E}_{\text{RO},\,i}^{(m)}(\mathbf{r}')\cdot\mathbf{E}_{\text{RO},\,j}^{(m)}(\mathbf{r}')\right|^2}}. \tag{2.14}$$

<u>Step 3</u> Average the frequency Jacobian maps at all sample frequencies to form the *averaged frequency Jacobian map*:

$$\overline{\underset{\cdot}{D}}_{\text{OUT},\,g}^{(m)}(\mathbf{r}') = \frac{1}{N_{\text{f}}}\sum_{m=1}^{N_{\text{f}}}\underset{\cdot}{D}_{\text{OUT},\,g}^{(m)}(\mathbf{r}'). \tag{2.15}$$

Step 4 Normalize the averaged frequency Jacobian map with respect to its maximum:

$$\bar{\ddot{D}}^{(m)}_{\mathrm{OUT},\,g}(\mathbf{r}') = \frac{\left|\bar{\dot{D}}^{(m)}_{\mathrm{OUT},\,g}(\mathbf{r}')\right|}{\left|\bar{\dot{D}}^{(m)}_{\mathrm{OUT},\,g}(\mathbf{r}')\right|_{\max}} \tag{2.16}$$

where $\left|\bar{\dot{D}}^{(m)}_{\mathrm{OUT},\,g}(\mathbf{r}')\right|_{\max}$ is the maximum value of $\left|\bar{\dot{D}}^{(m)}_{\mathrm{OUT},\,g}(\mathbf{r}')\right|$. The linear-scale map $\bar{\ddot{D}}^{(m)}_{\mathrm{OUT},\,g}(\mathbf{r}')$ can be plotted as it is or in a logarithmic scale:

$$\bar{\ddot{D}}^{(m)}_{\mathrm{OUT},\,g}(\mathbf{r}')_{\mathrm{dB}} = 10\log_{10}\bar{\ddot{D}}^{(m)}_{\mathrm{OUT},\,g}(\mathbf{r}')\,. \tag{2.17}$$

Notice that the sensitivity-based imaging solves the inverse problem in real space. Direct inversion is achieved by computing the imaging map values from one voxel to another, which is a fast real-time computation. There are two kinds of maps generated depending on the choice of the property variable $g = \varepsilon'_{\mathrm{RO}},\ \varepsilon''_{\mathrm{RO}}$, see (2.9), which reflect the property contrast in the real permittivity and the imaginary permittivity of the OUT, respectively. It should be pointed out that the sensitivity-based imaging only generates qualitative results with no value attached to the voxels' dielectric properties.

2.2.2 Planar raster-scanning system

Planar raster-scanning is a data-acquisition approach widely employed in microwave imaging [9]-[14]. Fig. 2.1 shows a general configuration of the system as an example. Two antennas, one transmitting and one receiving, are separated by a

distance d facing each other along their boresight, i.e., the z direction. During the scan, the two antennas move together in the top and bottom scanning planes, respectively, along the route that is shown with a dash-line in Fig. 2.1. The finite space between the top and bottom scanning planes is the imaged volume, where the measured object, e.g., the RO or the OUT, is placed. There are N_x and N_y sample points with the sampling intervals Δx and Δy along x and y, respectively. The sampling position $\mathbf{r}_{uv} = (x_u, y_v)$ with indices u = 1, 2, …, N_x and v = 1, 2, …, N_y is a function of the two coordinates x and y. If N_s' responses are acquired at a sample point $\mathbf{r}_{uv}$, then $N_s = N_s' \times N_x \times N_y$ responses can be obtained in one complete scan at each frequency. Practically, the scanning system has multiple selections of antennas or antenna arrays, such as horns [9][13], dipoles [10]-[12], bow-tie array [14], etc.

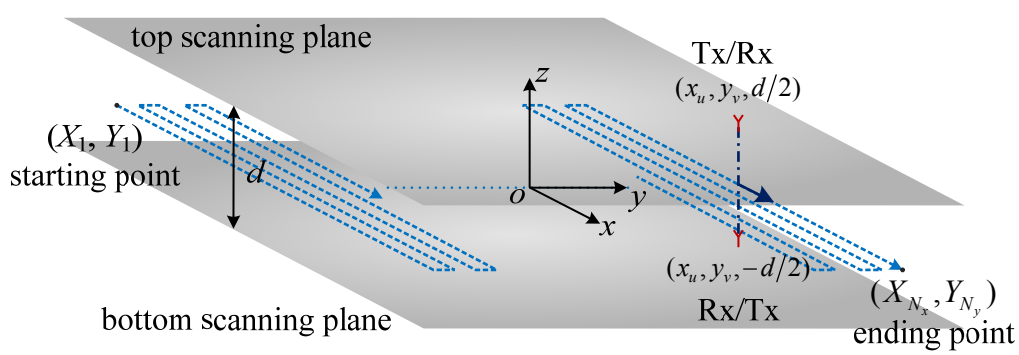

Fig. 2.1 Illustration of the planar raster-scanning acquisition system with two antennas aligned along their boresight (i.e., z direction) which scan at the top and the bottom planes along the route indicated by the dash-line.

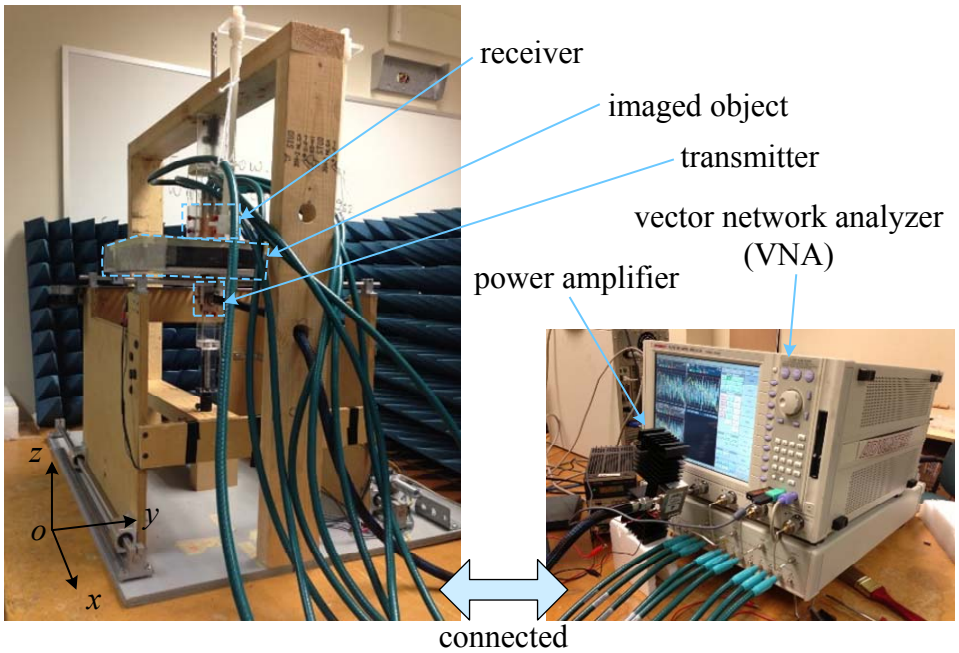

Fig. 2.2 Setup of the experimental planar raster-scanning system for data acquisition.

Fig. 2.2 shows an experimental planar raster-scanning system. The receiver of the experimental system is equipped with an antenna array, while the transmitter is a horn antenna. The imaged object, placed between the Rx and Tx antennas, moves along x and y to be scanned while the antennas remains still. The Rx and Tx antennas are separated by a vertical distance of approximately 6 cm with gaps of less than 2 mm to the object's surface. The scanning system is connected to the vector network analyzer (VNA) to measure the S-parameters. In order to boost the illumination power, a power amplifier is added between the VNA output port and the Tx antenna.

Only transmission signals can be acquired with the system setup. One complete scanning of the system with 21 sample points along both x and y (i.e., $N_x = N_y = 21$) and 81 sample frequencies (i.e., $N_f = 81$) needs about 2 hours. The scan time can be dramatically speeded up if electrical switch array is used.

In the work of this thesis, the data-acquisition procedure employs the planar raster-scanning, which is either emulated in an analytical model, or is simulated with full-wave EM solvers, or is performed with the experimental scanning system shown in Fig. 2.2.

2.3 CALIBRATION TECHNIQUE FOR SENSITIVITY-BASED MICROWAVE IMAGING

2.3.1 Calibration measurements

The proposed calibration technique aims to acquire the field distributions in (2.10) via measurements in order to avoid the use of analytical or simulation models. According to the definition of complex permittivity in (2.3), (2.10) is rewritten using the chain rule to obtain

$$\frac{\partial S_{\mathrm{RO},\,n}^{(m)}}{\partial g^{(m)}(\mathbf{r}')} = \begin{cases} \left.\dfrac{\partial S_{\mathrm{RO},\,n}^{(m)}}{\partial \varepsilon_{\mathrm{RO}}^{(m)}(\mathbf{r}')}\right|_{g=\varepsilon'_{\mathrm{RO}}} \\ -\mathrm{i}\left.\dfrac{\partial S_{\mathrm{RO},\,n}^{(m)}}{\partial \varepsilon_{\mathrm{RO}}^{(m)}(\mathbf{r}')}\right|_{g=\varepsilon''_{\mathrm{RO}}} \end{cases}, \tag{2.18}$$

which indicates that the derivatives $\partial S_{\mathrm{RO},\,n}^{(m)} \big/ \partial g^{(m)}(\mathbf{r}')$ $\left(g = \varepsilon'_{\mathrm{RO}},\ \varepsilon''_{\mathrm{RO}}\right)$ can be obtained from the derivative $\partial S_{\mathrm{RO},\,n}^{(m)} \big/ \partial \varepsilon_{\mathrm{RO}}^{(m)}(\mathbf{r}')$. Here, $g^{(m)}(\mathbf{r}')$ is a real number, while $\varepsilon_{\mathrm{RO}}^{(m)}(\mathbf{r}')$ is a complex number.

In order to evaluate $\partial S_{\mathrm{RO},\,n}^{(m)} \big/ \partial \varepsilon_{\mathrm{RO}}^{(m)}(\mathbf{r}')$ experimentally, the finite difference method is applied: at the *m*-th frequency, the dielectric property of the examined voxel at $\mathbf{r}'$ is perturbed to induce the corresponding variations in the responses. In practice, the property perturbation is realized by inserting a small scatterer into the RO at $\mathbf{r}'$. The RO together with the inserted small scatterer is the CO. The small scatterer has the same size as that of the image voxel, which is electrically small and below the imaging resolution. It also has the known complex permittivity of $\left[\varepsilon_{\mathrm{RO}}^{(m)} + \delta\varepsilon_{\mathrm{CO}}^{(m)}\right]$, where $\varepsilon_{\mathrm{RO}}^{(m)}$ represents the dielectric property of the RO and $\delta\varepsilon_{\mathrm{CO}}^{(m)}$ is the property contrast of the scatterer.

Then, for a particular voxel at $\mathbf{r}'$, the respective derivative can be approximated by

$$\frac{\partial S_{\mathrm{RO},\,n}^{(m)}}{\partial \varepsilon_{\mathrm{RO}}^{(m)}(\mathbf{r}')} \approx \frac{\Delta S_{\mathrm{CO},\,\mathbf{r}',\,n}^{(m)}}{\delta \varepsilon_{\mathrm{CO}}^{(m)}}, \tag{2.19}$$

where the response difference $\Delta S_{\mathrm{CO},\,\mathbf{r}',\,n}^{(m)}$ is calculated by

$$\Delta S_{\mathrm{CO},\,\mathbf{r}',\,n}^{(m)} = S_{\mathrm{CO},\,\mathbf{r}',\,n}^{(m)} - S_{\mathrm{RO},\,n}^{(m)}. \tag{2.20}$$

Notice that the subscript "$\mathbf{r}'$" in $S^{(m)}_{\mathrm{CO},\,\mathbf{r}',\,n}$ implies the location of the small scatterer. In other words, $S^{(m)}_{\mathrm{CO},\,\mathbf{r}',\,n}$ is obtained from the measurement of the CO that has the known small scatterer at $\mathbf{r}'$.

In addition, for the imaged volume discretized into N_{v} voxels, we can calculate the *complex* Jacobian map at the m-th frequency using

$$C^{(m)}_{\mathrm{OUT}}(\mathbf{r}'_P) = \frac{\partial F^{(m)}}{\partial \varepsilon^{(m)}_{\mathrm{RO}}(\mathbf{r}'_p)} = -\frac{1}{N_{\mathrm{s}}}\sum_{n=1}^{N_{\mathrm{s}}}\left[\Delta S^{(m)}_{\mathrm{OUT},\,n}\right]^{*}\cdot\frac{\partial S^{(m)}_{\mathrm{RO},\,n}}{\partial \varepsilon^{(m)}_{\mathrm{RO}}(\mathbf{r}'_p)}, \tag{2.21}$$

where p = 1, 2, …, N_{v} is the voxel index and the p-th voxel is at $\mathbf{r}'_p$. By substituting (2.19) to (2.21), we obtain

$$C^{(m)}_{\mathrm{OUT}}(\mathbf{r}'_p) = -\frac{1}{N_{\mathrm{s}}}\sum_{n=1}^{N_{\mathrm{s}}}\left[\Delta S^{(m)}_{\mathrm{OUT},\,n}\right]^{*}\cdot\frac{\Delta S^{(m)}_{\mathrm{CO},\,p,\,n}}{\delta \varepsilon^{(m)}_{\mathrm{CO}}}. \tag{2.22}$$

Here, for the sake of simplicity, we denote $\Delta S^{(m)}_{\mathrm{CO},\,\mathbf{r}'_p,\,n}$ as $\Delta S^{(m)}_{\mathrm{CO},\,p,\,n}$, where the subscript "$p$" indicates the p-th voxel at $\mathbf{r}'_p$. It is clear that the computation of (2.22) requires measurement data only, those of the RO, and the CO and the OUT.

Meanwhile, from (2.18) and (2.21), the maps in (2.9) can be represented by the complex Jacobian map in (2.22) simply through

$$D^{(m)}_{\mathrm{OUT},\,g}(\mathbf{r}'_p) = \begin{cases} \mathrm{Re}\left[C^{(m)}_{\mathrm{OUT}}(\mathbf{r}'_p)\right]\Big|_{g=\varepsilon'_{\mathrm{RO}}} \\ \mathrm{Im}\left[C^{(m)}_{\mathrm{OUT}}(\mathbf{r}'_p)\right]\Big|_{g=\varepsilon''_{\mathrm{RO}}} \end{cases}. \tag{2.23}$$

Here after, for brevity, we refer to the map $D_{\mathrm{OUT},\,g}^{(m)}(\mathbf{r}_p')$ as the *real map* when $g = \varepsilon_{\mathrm{RO}}'$ and the *imaginary map* when $g = \varepsilon_{\mathrm{RO}}''$.

The physical meaning behind the calibration technique can be also interpreted with the linear Born approximation, which is valid for weak scattering of small scattering volume with low property contrast [8]. It assumes that the internal total-field $\mathbf{E}_j^{(m)\mathrm{tot}}(\mathbf{r}')$ can be replaced by the incident field $\mathbf{E}_j^{(m)\mathrm{inc}}(\mathbf{r}')$ in the background medium, which reduces the scattering integral of (2.2) to

$$\mathbf{E}_j^{(m)\mathrm{sc}}(\mathbf{r}_i) \approx \int_{V_\mathrm{s}} k_m^2 \Delta\varepsilon^{(m)}(\mathbf{r}')\underline{\mathbf{G}}(\mathbf{r}_i,\mathbf{r}')\cdot\mathbf{E}_j^{(m)\mathrm{inc}}(\mathbf{r}')d\mathbf{r}',\ \ \mathbf{r}'\in V_\mathrm{s}\,. \tag{2.24}$$

When V_s is small, given (2.6), we can write (2.24) for the S-parameters as

$$\Delta S_n^{(m)} \approx k_m^2 \Delta\varepsilon^{(m)}(\mathbf{r}')\Omega_\mathrm{s}\boldsymbol{\rho}_i^{(m)}\cdot\underline{\mathbf{G}}(\mathbf{r}_i,\mathbf{r}')\cdot\mathbf{E}_j^{(m)\mathrm{inc}}(\mathbf{r}')\ \ . \tag{2.25}$$

For the CO with the small scatterer at $\mathbf{r}'$, the integral volume Ω_s is determined by the scatterer's electrical size $\overline{L}$, and we have $\Delta S_n^{(m)} \equiv \Delta S_{\mathrm{CO},\,\mathbf{r}',\,n}^{(m)}$ and $\Delta\varepsilon^{(m)}(\mathbf{r}') \equiv \delta\varepsilon_{\mathrm{CO}}^{(m)}$. If $\delta\varepsilon_{\mathrm{CO}}^{(m)}$ together with $\overline{L}$ satisfies the constraints of the linear Born approximation, then it can be shown rigorously that the S-parameter derivative $\partial S_{\mathrm{RO},\,n}^{(m)} \big/ \partial\varepsilon_{\mathrm{RO}}^{(m)}(\mathbf{r}')$ can be expressed as [2]

$$\frac{\partial S_{\mathrm{RO},\,n}^{(m)}}{\partial\varepsilon_{\mathrm{RO}}^{(m)}(\mathbf{r}')} = \lim_{\overline{L}\,\delta\varepsilon_{\mathrm{CO}}^{(m)}\to 0}\left[\frac{\Delta S_{\mathrm{CO},\,\mathbf{r}',\,n}^{(m)}}{\delta\varepsilon_{\mathrm{CO}}^{(m)}}\right]. \tag{2.26}$$

(2.26) implies the implementation of finite difference in (2.19) in our case is valid.

Also, the agreement between the linear Born approximation and the self-adjoint formula of (2.10) has been already proven in [2]. The latter can be derived from the former by replacing the product of Green's function and the polarization $\boldsymbol{\rho}_i^{(m)} \cdot \underline{\mathbf{G}}(\mathbf{r}_i, \mathbf{r}')$ in (2.25) with the incident field $\mathbf{E}_{\mathrm{RO},\,i}^{(m)}(\mathbf{r}')$ via reciprocity. Mathematically, the kernel of the self-adjoint formula, i.e., the product of the two incident fields $\left[\mathbf{E}_{\mathrm{RO},\,i}^{(m)}(\mathbf{r}') \cdot \mathbf{E}_{\mathrm{RO},\,j}^{(m)}(\mathbf{r}')\right]$, can be explicitly represented by the scattered signal $\Delta S_{\mathrm{CO},\,\mathbf{r}',\,n}^{(m)}$; see (2.10) and (2.19). This indicates that the whole product $\left[\mathbf{E}_{\mathrm{RO},\,i}^{(m)}(\mathbf{r}') \cdot \mathbf{E}_{\mathrm{RO},\,j}^{(m)}(\mathbf{r}')\right]$ can be experimentally assessed without knowing the individual incident-field distributions of $\mathbf{E}_{\mathrm{RO},\,i}^{(m)}(\mathbf{r}')$ and $\mathbf{E}_{\mathrm{RO},\,j}^{(m)}(\mathbf{r}')$. Thus, the proposed calibration technique provides all the RO field information needed to perform imaging with the self-adjoint approach.

2.3.2 Implementation of coordinate translation

The need of implementing coordinate translation stems from the fact that the CO measurements can be prohibitively long. According to (2.22), a CO measurement is required for a small scatterer placed at each voxel of the imaged volume. Hence, the generation of an image consisting of N_{v} voxels requires the measurements of N_{v} different COs. This is unacceptable since N_{v} often exceeds hundreds and thousands.

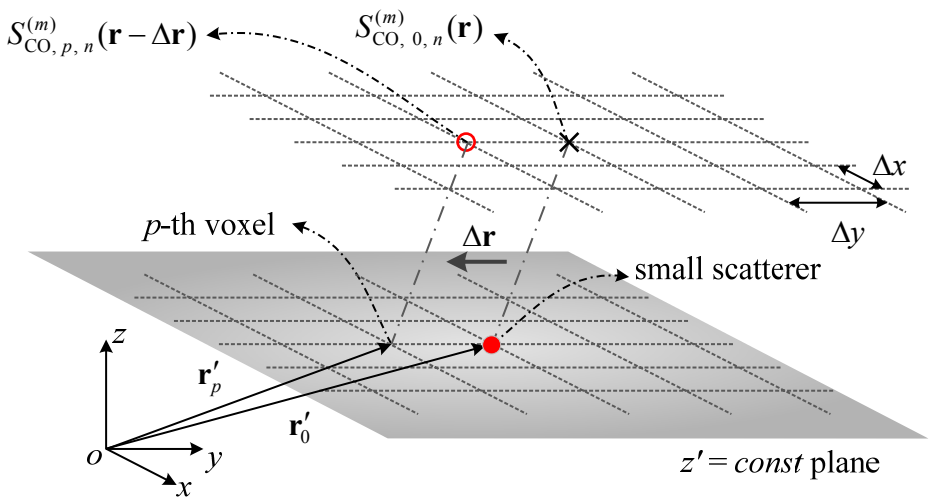

Fig. 2.3 Illustration of the coordinate translation using the response data of one calibration measurement for the $z' = const$ plane of interest.

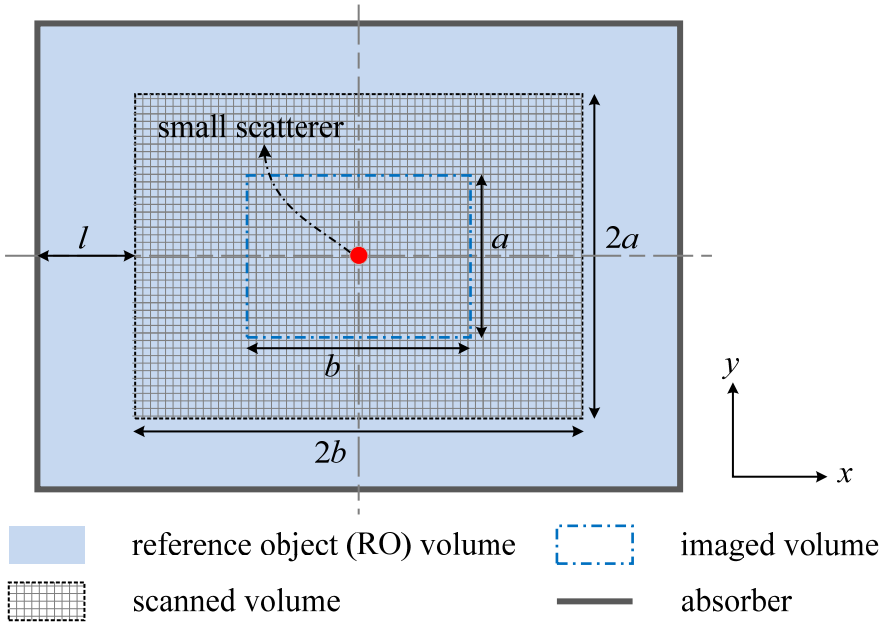

Fig. 2.4 Illustration of the RO volume, the imaged volume and the scanned volume in the RO and CO measurements using the planar raster-scanning data acquisition.

Fortunately, if the background medium (the RO) is assumed homogeneous in all 3 dimensions (x, y and z) or invariant in at least one of the coordinate variable, the number of the necessary calibration measurements can be drastically reduced. This is because the response corresponding to a scatterer position along any coordinate variable, with respect to which the background properties are constant, can be obtained from a single measurement via coordinate translation.

The assumption of a homogeneous or layered background is common in imaging. It is also exploited here for the planar raster-scanning system. Fig. 2.3 illustrates the implementation of coordinate translation. For each layer of interest (e.g., the $z' = const$ plane), only one CO measurement is required with the small scatter at the plane center $\mathbf{r}_0' = (x_0', y_0', z')$. We denote the respective acquired responses as $S_{\mathrm{CO},\,0,\,n}^{(m)}(\mathbf{r})$. Then, for another ($p$-th) voxel at $\mathbf{r}_p' = (x_p', y_p', z')$, the corresponding responses $S_{\mathrm{CO},\,p,\,n}^{(m)}(\mathbf{r})$ can be obtained from $S_{\mathrm{CO},\,0,\,n}^{(m)}(\mathbf{r})$ by a simple translation

$$S_{\mathrm{CO},\,p,\,n}^{(m)}(\mathbf{r}) = S_{\mathrm{CO},\,0,\,n}^{(m)}(\mathbf{r} - \Delta\mathbf{r}), \tag{2.27}$$

where

$$\Delta\mathbf{r} = \mathbf{r}_p' - \mathbf{r}_0' = (x_p' - x_0', y_p' - y_0', 0). \tag{2.28}$$

If the imaged volume has N_z layers, the planar raster-scanning system is characterized only by N_z calibration measurements when using coordinate

translation. In near-field microwave imaging, N_z is typically less than 10, which implies overall calibration time on the order of couple of hours with a mechanically scanned system such as the one shown in Fig. 2.2.

Fig. 2.4 shows the top view of the RO volume, the imaged volume and the scanned volume in the RO and CO measurements using the planar raster-scanning system. In the measurements, the aperture of the scanned volume ($2a \times 2b$) is twice larger than that of the imaged volume ($a \times b$), so that the coordinate translation (2.27) can be performed. In practice, the edges of the RO may violate the translational invariance. Thus, the scanned volume should be away from the RO's edges with a sufficient distance of l. Additionally, absorbers can be attached onto the edges to reduce reflection. The scanned aperture of the OUT measurement is the same as that of the imaged volume.

2.3.3 Image formation employing calibration measurements

Here, the procedure of image formation is summarized for the planar raster-scanning system; however, it can be easily modified for other data-acquisition schemes. At the m-th frequency and for all the $z' = const$ planes of interest, the procedural steps are summarized below.

A. Calibration steps

<u>Step 1</u> Acquire the RO responses $S_{\mathrm{RO},\,n}^{(m)}(\mathbf{r}_{uv})$ via RO measurements.

Step 2 Acquire the CO responses $S^{(m)}_{\mathrm{CO},\,0,\,n}(\mathbf{r}_{uv})$ via CO measurements with the small scatterer at the center $\mathbf{r}'_0$ of each desired $z' = const$ plane.

Step 3 Obtain all the CO responses $S^{(m)}_{\mathrm{CO},\,p,\,n}(\mathbf{r}_{uv})$ from $S^{(m)}_{\mathrm{CO},\,0,\,n}(\mathbf{r}_{uv})$ using coordinate translation (2.27), $p = 1, 2, \ldots, N_{\mathrm{v}}$.

Step 4 Obtain $\Delta S^{(m)}_{\mathrm{CO},\,p,\,n}(\mathbf{r}_{uv})$ using

$$\Delta S^{(m)}_{\mathrm{CO},\,p,\,n}(\mathbf{r}_{uv}) = S^{(m)}_{\mathrm{CO},\,p,\,n}(\mathbf{r}_{uv}) - S^{(m)}_{\mathrm{RO},\,n}(\mathbf{r}_{uv})\,. \tag{2.29}$$

B. OUT imaging steps

Step 5 Acquire the OUT responses $S^{(m)}_{\mathrm{OUT},\,n}(\mathbf{r}_{uv})$ via OUT measurements.

Step 6 Obtain $\Delta S^{(m)}_{\mathrm{OUT},\,n}(\mathbf{r}'_{uv})$ using

$$\Delta S^{(m)}_{\mathrm{OUT},\,n}(\mathbf{r}'_{uv}) = S^{(m)}_{\mathrm{OUT},\,n}(\mathbf{r}'_{uv}) - S^{(m)}_{\mathrm{RO},\,n}(\mathbf{r}_{uv})\,. \tag{2.30}$$

Step 7 Compute the complex Jacobian map using

$$C^{(m)}_{\mathrm{OUT}}(\mathbf{r}'_p) = -\frac{1}{N_x N_y N'_{\mathrm{s}}} \sum_{u=1}^{N_x} \sum_{v=1}^{N_y} \sum_{n=1}^{N'_{\mathrm{s}}} \left[\Delta S^{(m)}_{\mathrm{OUT},\,n}(\mathbf{r}'_{uv})\right]^* \cdot \frac{\Delta S^{(m)}_{\mathrm{CO},\,p,\,n}(\mathbf{r}'_{uv})}{\delta\varepsilon^{(m)}_{\mathrm{CO}}} \tag{2.31}$$

for all N_{v} imaging voxels.

Step 8 Generate the real-permittivity map and/or the imaginary-permittivity map $D^{(m)}_{\mathrm{OUT},\,g}(\mathbf{r}'_p)\Big|_{g=\varepsilon'_{\mathrm{RO}},\,\varepsilon''_{\mathrm{RO}}}$ using (2.23).

Step 9 Normalize each map $D^{(m)}_{\mathrm{OUT},\,g}(\mathbf{r}'_p)$ using the energy normalization [2] for all N_{v} imaging voxels:

$$\underset{\cdot}{D}^{(m)}_{\mathrm{OUT},\,g}(\mathbf{r}'_p) = \frac{D^{(m)}_{\mathrm{OUT},\,g}(\mathbf{r}'_p)}{\frac{1}{N_{\mathrm{v}}}\sqrt{\sum_{p=1}^{N_{\mathrm{v}}}\left|D^{(m)}_{\mathrm{OUT},\,g}(\mathbf{r}'_p)\right|^2}} \tag{2.32}$$

<u>Step 10</u> Average the maps $\underset{\cdot}{D}^{(m)}_{\mathrm{OUT},\,g}(\mathbf{r}'_p)$ to form the *frequency averaged map* with the N_{f} frequency samples:

$$\overline{\underset{\cdot}{D}}^{(m)}_{\mathrm{OUT},\,g}(\mathbf{r}'_p) = \frac{1}{N_{\mathrm{f}}}\sum_{m=1}^{N_{\mathrm{f}}}\underset{\cdot}{D}^{(m)}_{\mathrm{OUT},\,g}(\mathbf{r}'_p)\,. \tag{2.33}$$

Notice that only measured data are required in the whole procedure. Analytical or simulation models are replaced by models derived from calibration measurements, which ensures better model fidelity and ultimately better imaging results. At the same time, the real-time performance of the original sensitivity-based imaging is preserved. With planar raster scanning, the algorithm above generates 3D images in sets of 2D (slice) images for all N_z range locations. However, at this stage, the imaging results remain qualitative.

2.3.4 Validation example using synthetic data

This validation example employs synthetic data obtained from an analytical model implemented with Matlab [15]. The planar raster-scanning system shown in Fig. 2.1 is emulated for scanning aperture of 20 cm × 20 cm with a scanning interval of 0.25 cm along both x and y directions. The distance between the two scanning planes is d

= 5 cm. The isotropic point probe and the isotropic scalar wave source are adopted as receiving and transmitting antennas, respectively.

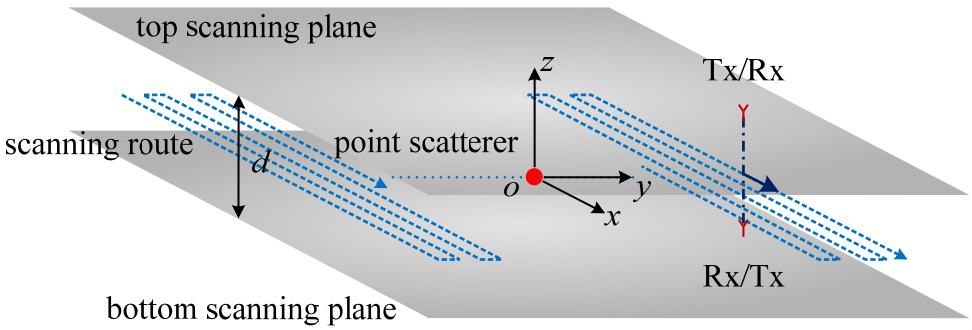

(a)

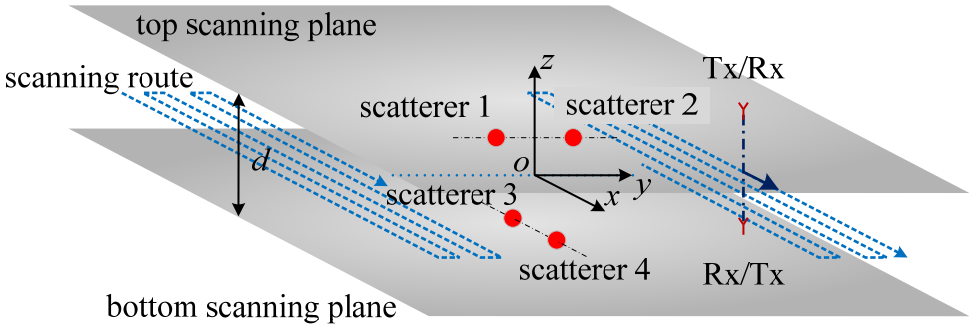

(b)

Fig. 2.5 Configuration of the analytical model: (a) the CO and (b) the OUT. The scanning route is indicated by the dash-line. The point scatterer is indicated by the red spot.

For the m-th frequency, the incident field at the observation point $\mathbf{r}'$ due to the j-th transmitter located at $\mathbf{r}'_j$ is calculated by

$$E_{\mathrm{RO},j}^{(m)}(\mathbf{r}') = \frac{e^{-\mathrm{i}k_m|\mathbf{r}'-\mathbf{r}'_j|}}{4\pi|\mathbf{r}'-\mathbf{r}'_j|}, \tag{2.34}$$

where k_m is the wave number of the background medium (i.e., the RO) at the m-th frequency.

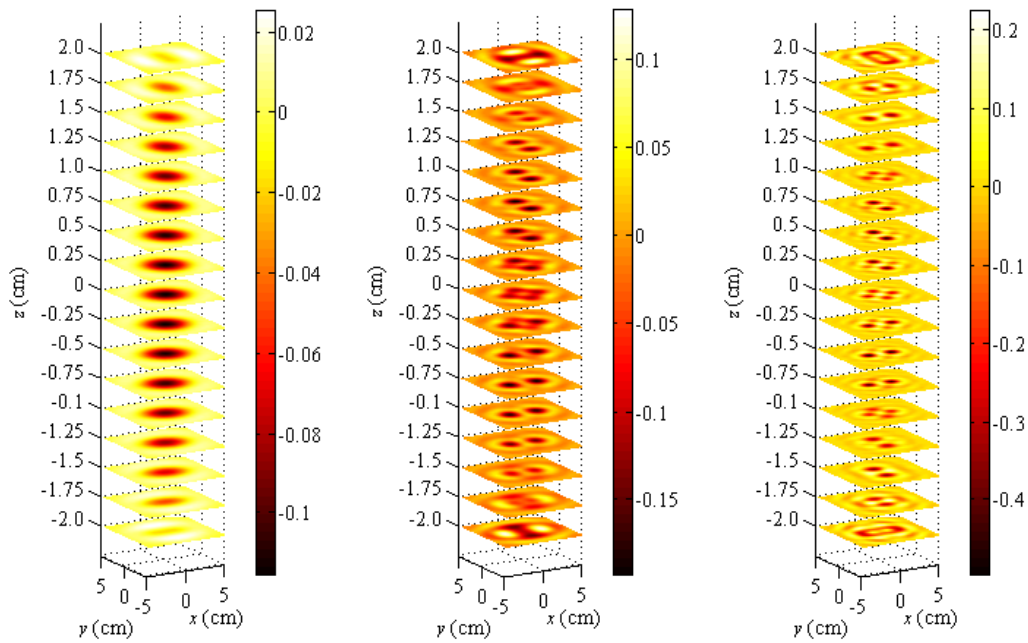

Fig. 2.6 3D normalized real maps of the four scatterers in the OUT shown in Fig. 2.5(b) at: (a) 3GHz, (b) 6 GHz, and (c) 9 GHz.

With the presence of a point scatter at $\mathbf{r}'$, the scattered field $E_j^{(m)\mathrm{sc}}(\mathbf{r}_i')$ detected by the i-th antenna is calculated using the linear Born approximation of (2.24). Since the Rx antenna is an isotropic point probe with all-ones polarization vector, we let the acquired responses be the scalar field values detected by the probe. In the case of multiple scatters, the point scatters are separated with a sufficient distance (more than half a wavelength) so that mutual coupling is negligible.

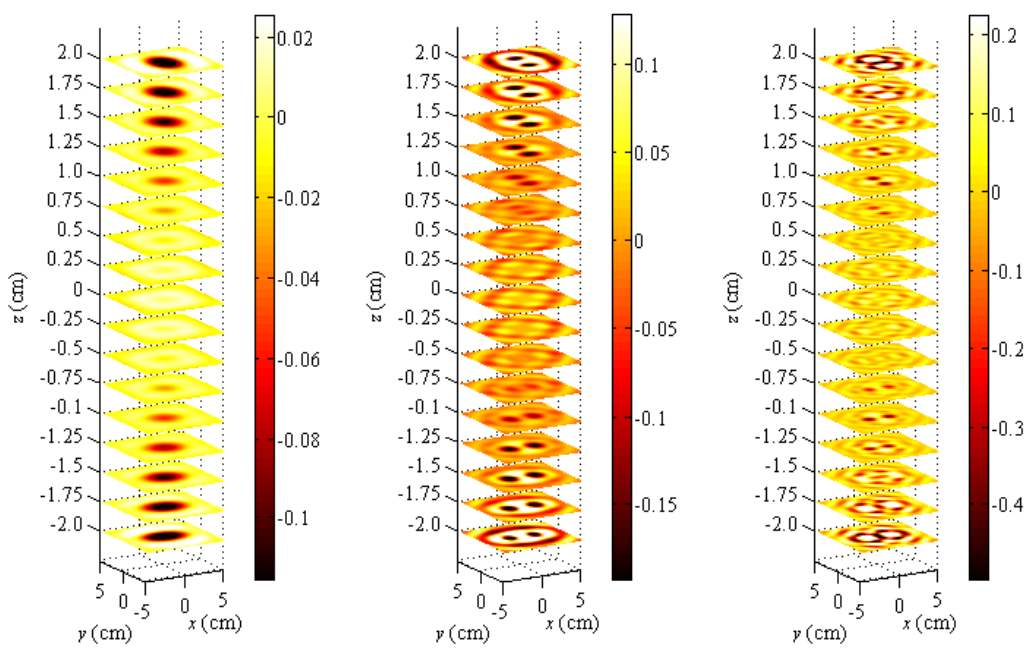

Fig. 2.7 3D normalized imaginary maps of the four scatterers in the OUT shown in Fig. 2.5(b) at: (a) 3GHz, (b) 6 GHz, and (c) 9 GHz.

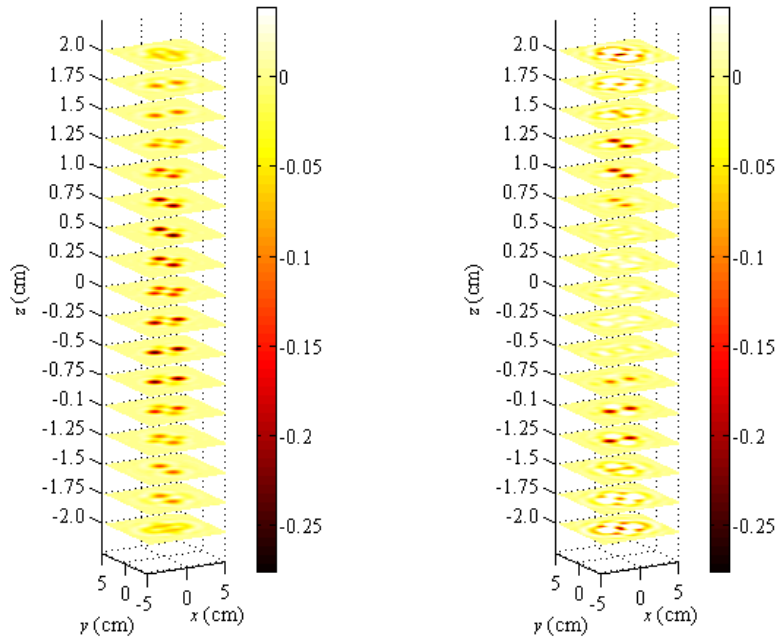

(a) (b)

Fig. 2.8 3D frequency averaged maps of the four scatterers in the OUT shown in Fig. 2.5(b): (a) real map and (b) imaginary map.

In this example, the RO is air. The configurations of the CO and the OUT measurements are shown in Fig. 2.5(a) and Fig. 2.5(b), respectively. In the CO measurements, a point scatterer with a unit property contrast of 1 (i.e., $\delta\varepsilon_{\text{co}}^{(m)} = 1$) is placed at the center of each range plane of interest, e.g., the $z' = 0$ cm plane. In the OUT measurement, four identical point scatterers, which have the same properties as that in the CO, are placed in two different layers. One pair of them, i.e., the scatterers 1 and 2, are placed along y axis with a separation of 3 cm in the $z' = 0.5$ cm plane. The other pair, i.e., the scatterers 3 and 4, are placed along the x axis with the same

separation in the $z' = -0.5$ cm plane. The top scanning plane is at $z' = 2.5$ cm, and the bottom scanning plane is at $z' = -2.5$ cm. The sample frequencies are from 3 GHz to 10 GHz with an interval of 1 GHz.

Fig. 2.6 shows the 3D normalized real maps $D^{(m)}_{\mathrm{OUT},\,\varepsilon'_{\mathrm{RO}}}$ at the frequencies of 3 GHz, 6 GHz, and 9 GHz, while Fig. 2.7 shows the normalized imaginary maps $D^{(m)}_{\mathrm{OUT},\,\varepsilon''_{\mathrm{RO}}}$ at the same frequencies. These maps are obtained at Step 9 of the image-formation procedure in Section 2.3.3. In the real maps, the peak values show at each frequency where the targets actually reside; see the $z' = 0.5$ cm and $z' = -0.5$ cm planes in Fig. 2.6. On the contrary, in the respective imaginary maps, the map values tend to be zero at those two layers; see the $z' = 0.5$ cm and $z' = -0.5$ cm planes in Fig. 2.7. This is compliant with the fact that the four point scatterers only have nonzero property contrast in their real permittivity while their imaginary permittivity contrast is zero. However, in both maps, strong artifacts are observed at the top and bottom layers, e.g., $z' = 1.25$ cm and $z' = -1.25$ cm planes, which varies as the frequency changes. In general, the image resolution improves as the frequency increases. At lower frequencies such as 3 GHz, the four targets merge together but become distinguishable at higher frequencies such as 9 GHz.

Notice that the normalized maps are obtained essentially from the Fréchet derivative of the response difference; see (2.31). Thus, the signs of the map values are opposite to the sign of the respective property contrast. For instance, at the real

locations of the four targets where the real permittivity contrast is positive, negative values show in the real maps of Fig. 2.6(a)-(b).

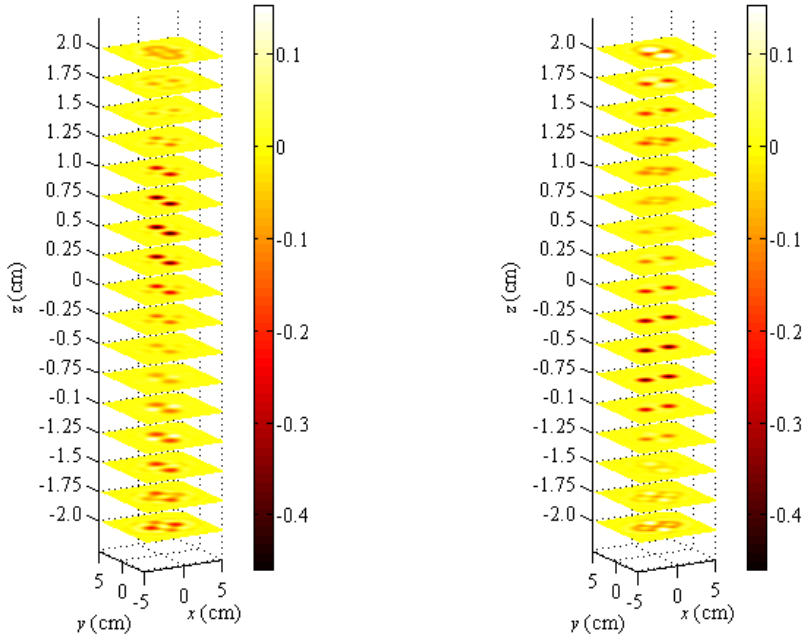

Fig. 2.9 3D frequency averaged maps of the four different OUT scatterers, two of permittivity 1 + i0 and two of permittivity 0 − i1, located as shown in Fig. 2.5(b): (a) real map and (b) imaginary map.

Fig. 2.8 shows the 3D frequency averaged real map $\bar{D}^{(m)}_{\text{OUT},\,\varepsilon'_{\text{RO}}}$ and imaginary-map $\bar{D}^{(m)}_{\text{OUT},\,\varepsilon''_{\text{RO}}}$, which are obtained at Step 10 of the image-formation procedure in Section 2.3.3. The artifacts in both maps have been somewhat canceled out after the frequency averaging and the image quality is improved. The four targets are

successfully detected and clearly shown in the frequency averaged real map while some artifacts are observed in the frequency averaged imaginary map.

Next, changes are made to the point scatterer's permittivity in the OUT: the property contrasts of the scatterers 3 and 4 are both changed to $0 - i1$, while those of the scatterers 1 and 2 remain the same, i.e., $1 + i0$. Fig. 2.9 shows the respective 3D frequency averaged real and imaginary maps. Compared with the maps in Fig. 2.8, although artifacts still exist, the scatterers 3 and 4 correctly disappear in the frequency averaged real map and appear in the frequency averaged imaginary map at their real locations. Meanwhile, the scatterers 1 and 2 correctly remain in the real map and do not show in the imaginary map.

2.3.5 Validation example using experimental data

2.3.5.1 Detection of two dielectric cylinders in lossy dielectric material

The experiment is performed with the planar raster-scanning system shown in Fig. 2.2. The Rx antenna is equipped with a 9-element bow-tie array [14] that has 5 bow-tie elements polarized along x and 4 polarized along y. The Tx antenna is a TEM (transverse electromagnetic) horn [16] polarized along x. Together with the imaged object, the Tx and Rx antennas form a 10-port network that allows for the measurement of 9 transmission signals for each sample position. Additionally, the measurements are also performed with the imaged object flipped over, which is

equivalent to switching the Tx and Rx locations. Consequently, the total number of acquired transmission signals at one sample position is N_s = 18. There are N_f = 86 equally spaced sampling points from 3 GHz to 8.95 GHz.

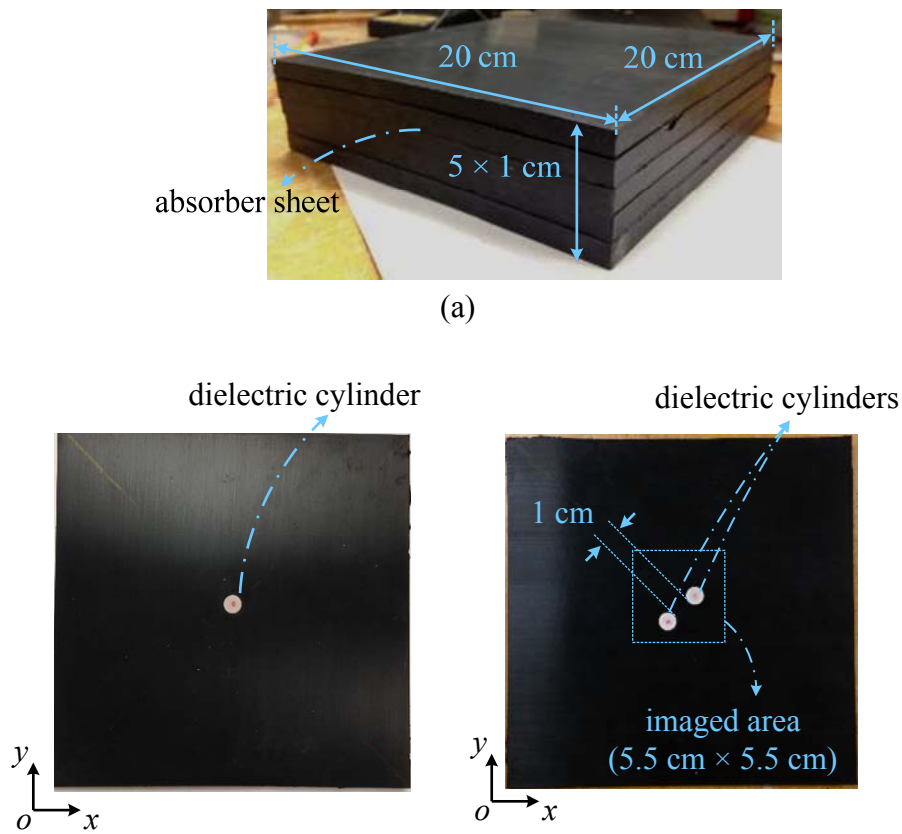

Fig. 2.10 Configuration of the imaged objects in the experiment: (a) the RO made of 5 stacked absorber sheets; (b) the layer of the CO with a dielectric cylinder inserted; (c) the middle layer of the OUT.

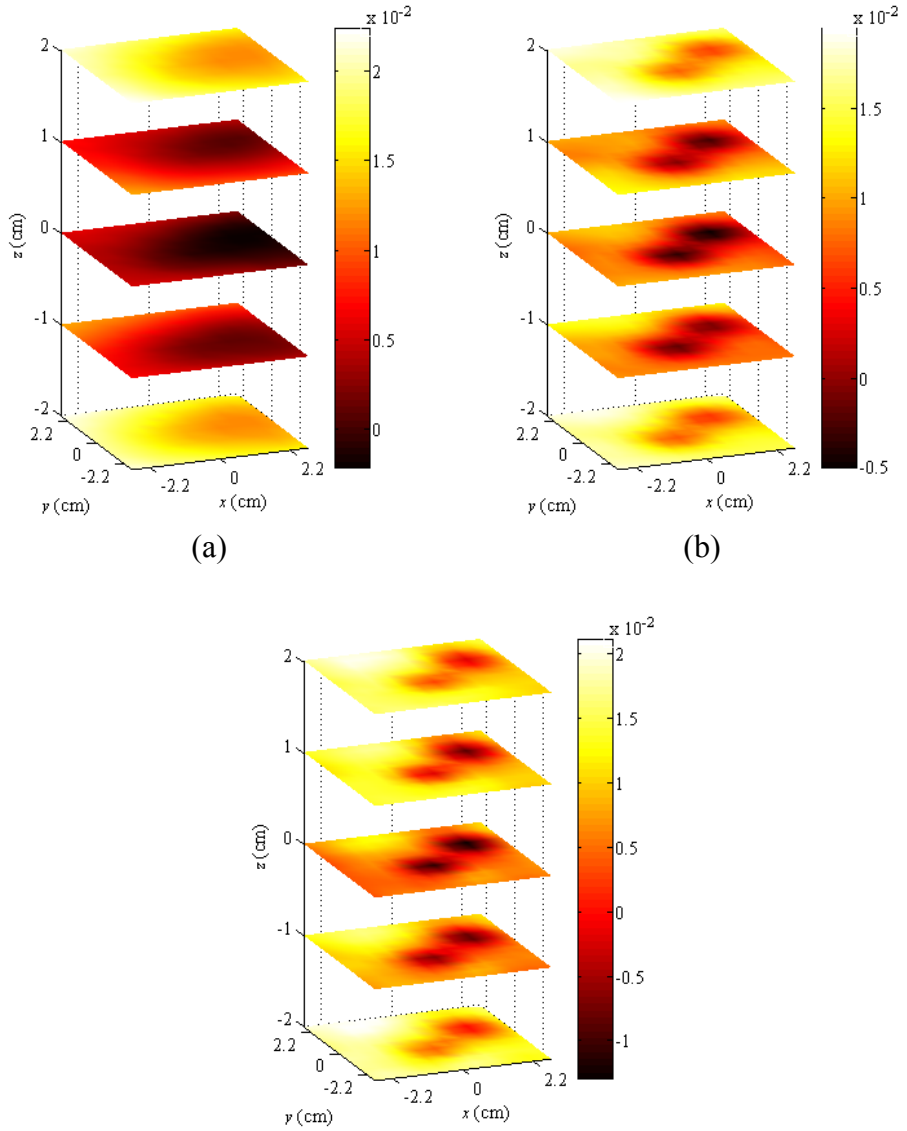

Fig. 2.11 3D normalized real maps of the two dielectric cylinders at: (a) 3.63GHz, (b) 6.08 GHz, and (c) 8.53 GHz.

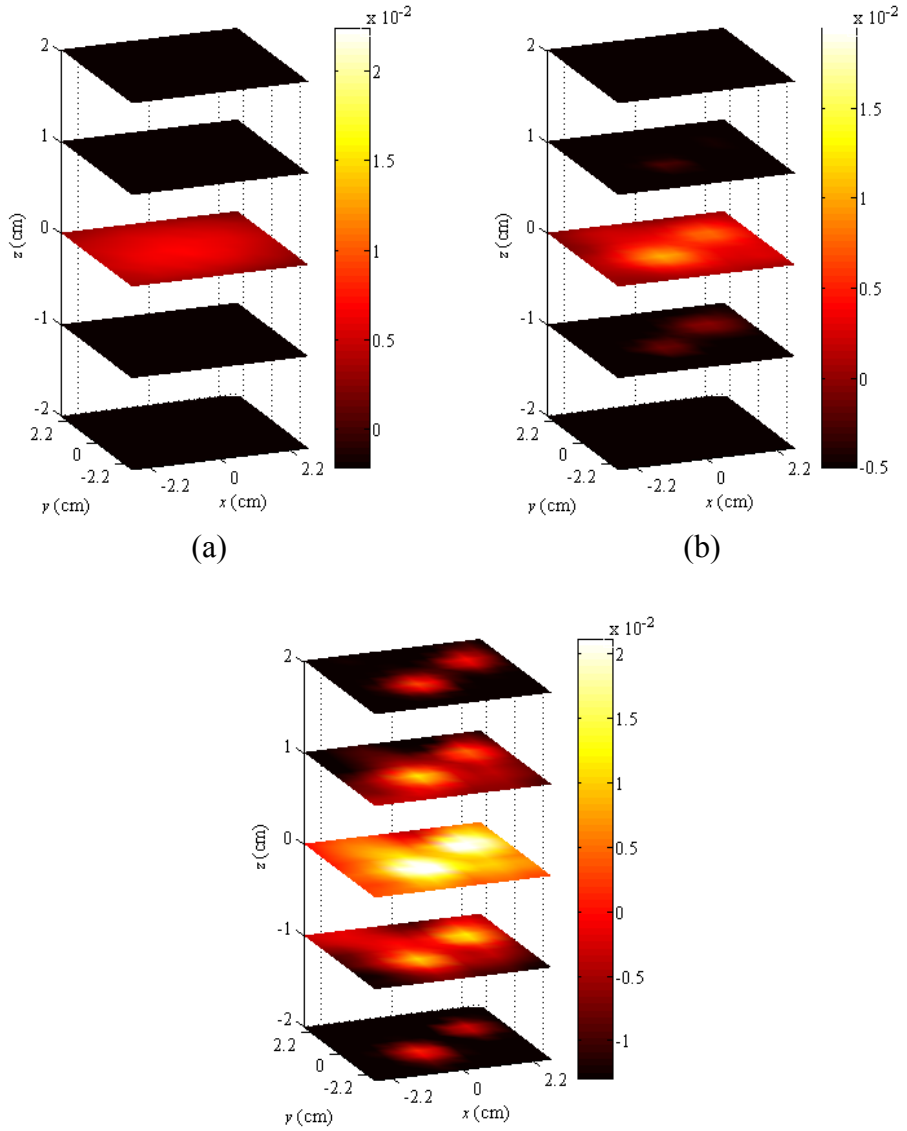

Fig. 2.12 3D normalized imaginary maps of the two dielectric cylinders at: (a) 3.63GHz, (b) 6.08 GHz, and (c) 8.53 GHz.

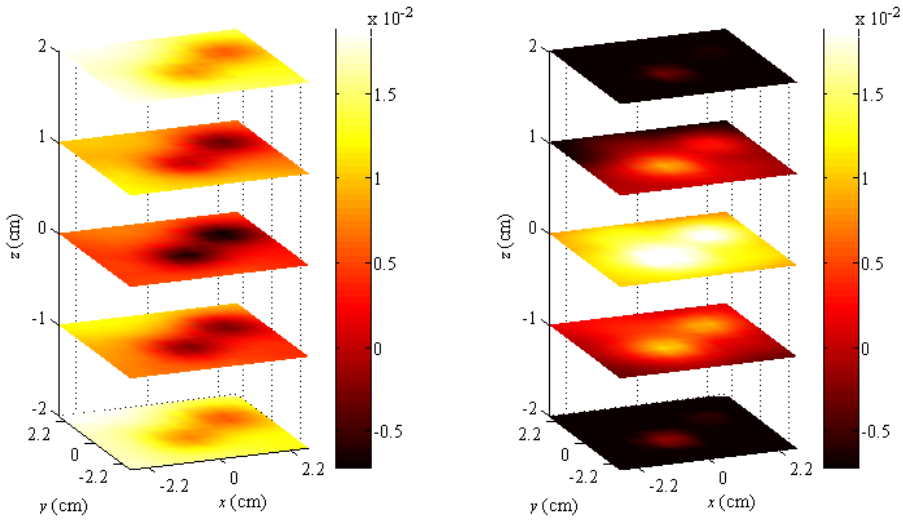

(a) (b)

Fig. 2.13 3D frequency averaged maps of the two dielectric cylinders: (a) real map and (b) imaginary map.

The RO in this example is made of 5 absorber sheets [17] as shown in Fig. 2.10(a). Each absorber sheet has the dimensions of 20 cm × 20 cm × 1cm with the mean complex permittivity of 10 – i5 over the frequency band.

The CO is the same as the RO except that a dielectric cylinder [17] is inserted at the center of the layer of interest in the RO; see Fig. 2.10(b). The dielectric cylinder has a diameter of 1 cm and a height of 1 cm with the mean complex permittivity of 15 – i0.003 over the frequency band.

The OUT is the same as the RO except that two dielectric cylinders are inserted in the middle layer of the RO; see Fig. 2.10(c). The two dielectric cylinders

in the OUT are the same as that in the CO. They are placed next to each other at an edge-to-edge distance of 1 cm, which is roughly equal to the anticipated spatial resolution. The imaged area is also shown in Fig. 2.10(c), which is a 5.5 cm × 5.5 cm square.

Fig. 2.11 shows the 3D normalized real maps at the frequencies of 3.63 GHz, 6.08 GHz, and 8.53 GHz, while Fig. 2.12 shows the normalized imaginary maps at the same frequencies. Fig. 2.13 shows the 3D real and imaginary maps after frequency averaging. Each slice shown in the figures represents one absorber sheet. The absorber sheet in the middle layer, in which the two dielectric cylinders reside, is at the $z' = 0$ cm plane. In all results, the two dielectric cylinders are successfully detected.

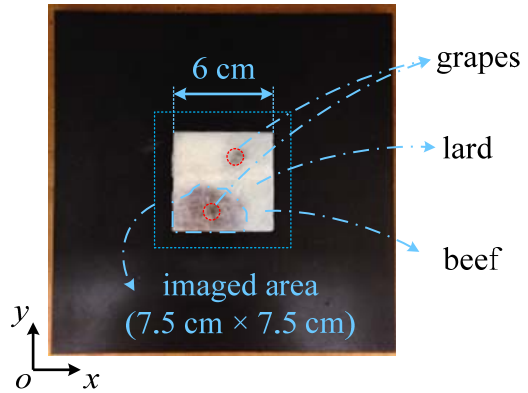

Fig. 2.14 Configuration of the middle layer of the OUT used in the experiment.

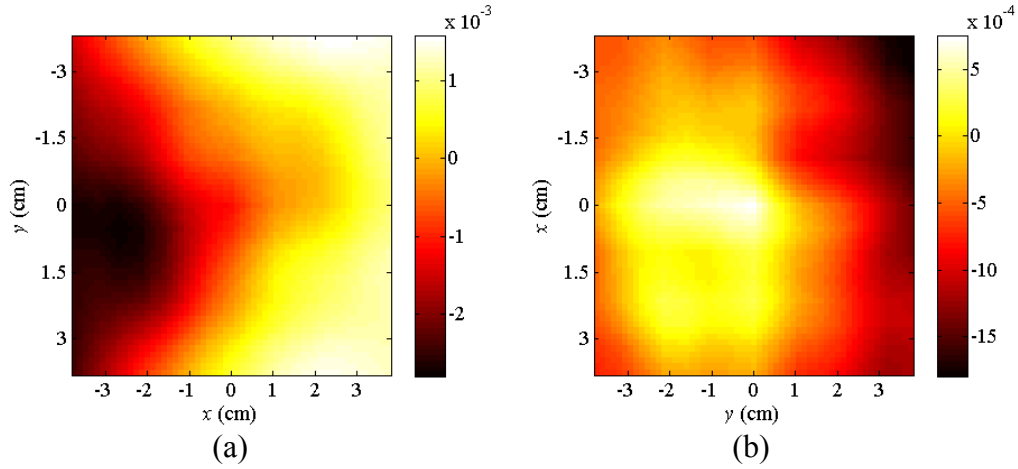

(a) (b)

Fig. 2.15 2D frequency averaged maps for the middle layer of the tissue phantom: (a) the real map and (b) the imaginary map. The measurement data of the RO1 and the CO1 are used in this case.

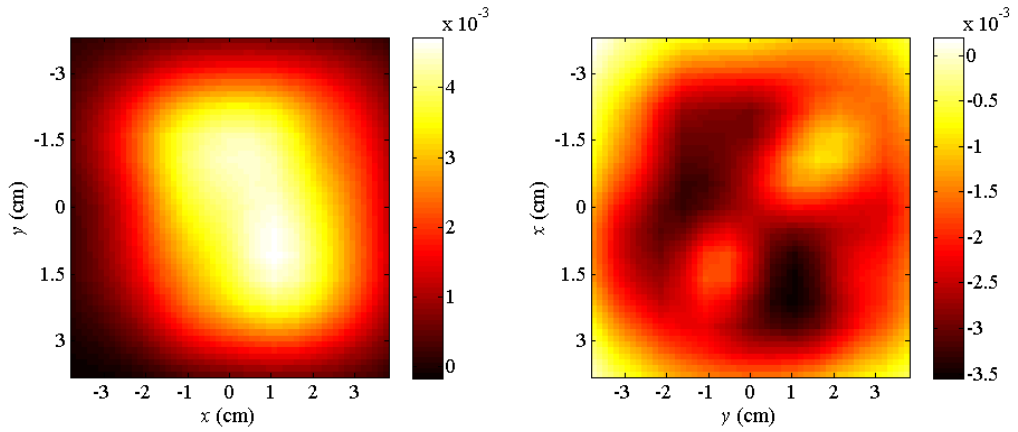

(a) (b)

Fig. 2.16 2D frequency averaged maps for the middle layer of the tissue phantom: (a) the real-map and (b) the imaginary map. The measurement data of the RO2 and the CO2 are used in this case.

Similarly to the synthetic example, it is observed that: (i) the imaging resolution becomes better at higher frequencies; (ii) artifacts vary as the frequency changes, (iii) often, artifacts are canceled out after frequency averaging, and (iv) the sign of the map values are opposite to the sign of the respective property contrast.

2.3.5.2 Detection of grape inclusions in lossy tissue phantom

The experiment is performed with the planar raster-scanning system shown in Fig. 2.2. The Rx is equipped with the same 9-element bow-tie array [14] as that used in the previous example. However, the Tx antenna is a 2-port quad-ridge dual-polarized horn. Together with the imaged object, the Tx and Rx antennas form an 11-port network that allows for the measurement of 18 transmission signals at each sample position. Also, the imaged object is flipped over along the x and y axis, respectively, in the measurements to acquire more responses. Equivalently, the total number of acquired transmission signals at each sample position is N_s = 54. The sample frequencies are equally spaced between 3 GHz to 8.95 GHz with the number of samples being N_f = 86.

The OUT here is a lossy tissue phantom that is the same as the RO of 5-layer absorber sheets except for the middle layer, which is partially filled with porcine and bovine meat samples as well as grape inclusions. As shown in Fig. 2.14, the cut-off area of the absorber sheet is mostly filled with lard, while some beef fills the small area at the left corner. There are two grapes, one embedded in the lard and the other embedded in the beef, each of which has a size smaller than 1 cm^3. The mean

complex permittivities of the lard, the beef and the grapes over the frequency band are 2.3 – i0.03, 35.7 – i19.3 and 51.8 – i24.9, respectively. The imaged area is a square of 7.5 cm × 7.5 cm as shown in Fig. 2.14. The goal of the experiment is to detect the small targets, i.e., the grapes in the OUT.

First, the calibration measurement with the RO and the CO in the previous example of detecting two dielectric cylinders are used for the image formation; see Fig. 2.10(a) and (b). To distinguish with the later implementation, the RO and the CO are referred to as the RO1 and the CO1. Fig. 2.15(a) shows the 2D frequency averaged real map for the middle layer of the OUT, while Fig. 2.15(b) shows the respective imaginary map. The results fail to show the grapes clearly although the beef area seems detectable in the imaginary map; see Fig. 2.15(b). This is expected given that the grapes are embedded in a medium (a mix of lard and beef) which differ significantly from that of the RO1. In this situation, the linear Born approximation is violated due to the nonuniform high-contrast large-size target. This has a detrimental effect on the results obtained with on our imaging method, the forward model of which relies on the linear Born approximation to present the scattering process.

Next, a second set of RO2 and CO2 is introduced and is measured as part of the system calibration. RO2 is made by replacing the middle layer of the RO1 with a layer of lard with roughly the same dimensions as the OUT. The CO2 is the same as the RO1 except for containing a grape inserted at the center of the middle layer. Fig.

2.16 shows the 2D frequency averaged real and imaginary maps for the middle layer of the OUT. Now, the two grapes are clearly detected as peaks in the imaginary map (see Fig. 2.16(b)). The “beef” area is also detected. On the other hand, the real map (see Fig. 2.16(a)) remains inconclusive. This may be because the mediums, i.e., the lard, beef, grapes and absorber sheet, have relatively lower contrast in the real permittivity than that in the imaginary permittivity.

The above experiments confirm that the image quality of the proposed method depends strongly on the choice of the background medium, i.e., the RO, as well as the small scatterer permittivity in the CO. The closer the RO is the majority of the OUT volume, the better the imaging results. This limitation stems from the linearized scattering model (i.e., the linear Born approximation) employed by the technique. It is also worth emphasizing that the grapes cannot be detected in the maps generated with simulated incident-field distributions regardless of the selection of the RO. This is due to the inability of the simulations to properly represent the incident-field distributions in the RO. Additionally, the simulation of such a complicated scenario including the tissue phantom and experimental setup is prohibitively slow.

2.4 SIGNIFICANCE OF THE REFLECTION SIGNALS FOR THE IMAGING RESOLUTION

An important phenomenon has been observed during the implementation of the proposed imaging method with the planar raster-scanning system. The reflection signals have great significance for the range resolution, i.e., the resolution along the *z*-direction when the antennas scan *x*-*y* planes; see Fig. 2.1 and Fig. 2.2. We refer to the resolution in the *x*-*y* plane as the cross-range resolution.

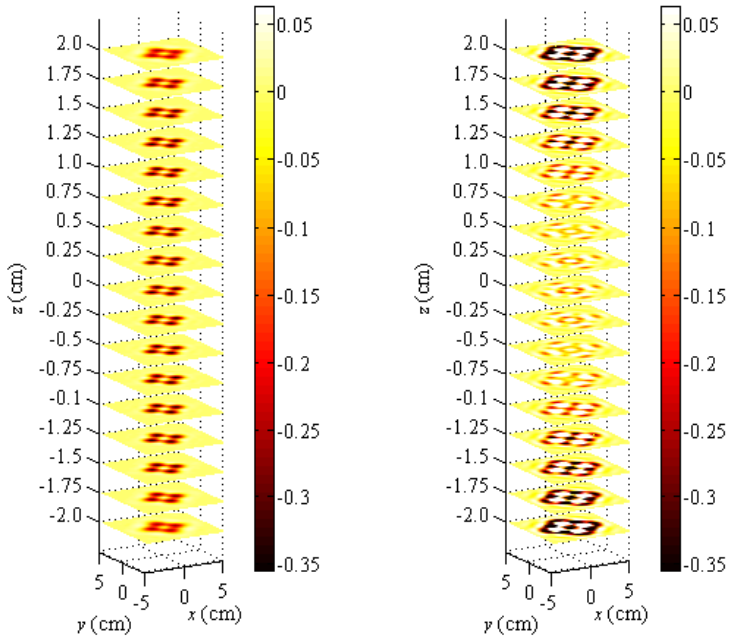

(a) (b)

Fig. 2.17 3D frequency averaged maps of the four scatterers of same contrast: (a) real map and (b) imaginary map. Only transmission signals are used in this case.

Let us revisit the example using synesthetic data in Section 2.3.4, where the OUT contains two targets in the $z' = -0.5$ cm plane and two targets in the $z' = -0.5$ cm plane. In this example, the pair of the isotropic point probe and the isotropic scalar wave source forms a 2-port network. At each sample point, we acquire the transmission signals $S_{21}^{(m)}$ and $S_{12}^{(m)}$ as well as the reflection signals $S_{11}^{(m)}$ and $S_{22}^{(m)}$ ($i = 1, 2; j = 1, 2$).

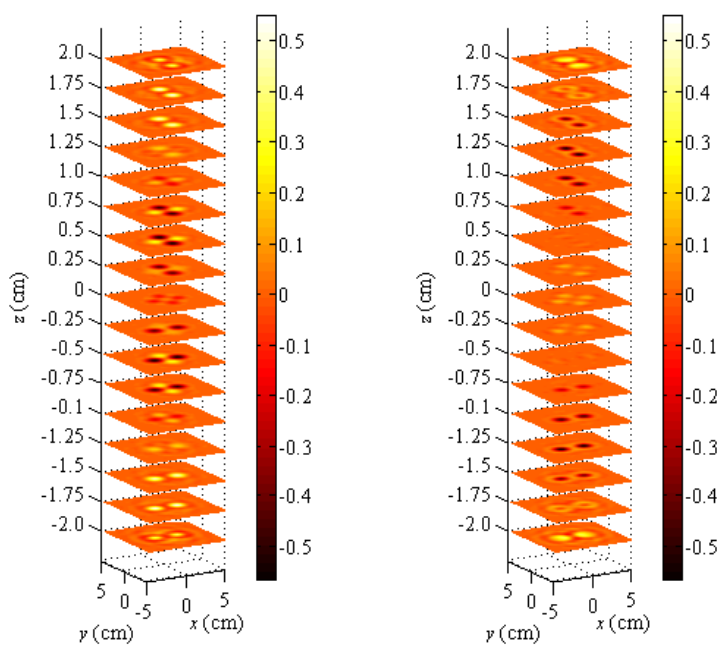

(a) (b)

Fig. 2.18 3D frequency averaged maps of the four scatterers of same contrast: (a) real map and (b) imaginary map. Only reflection signals are used in this case.

Fig. 2.17 shows the imaging results generated using transmission signals only, while Fig. 2.18 shows the results generated using reflection signals only. Similar patterns appear at different layers in the maps of Fig. 2.17, where the depth information of the four targets is lost. On the contrary, the four targets appear correctly at the proper layers in Fig. 2.18, the results of which are also similar to that of Fig. 2.8. However, the results of Fig. 2.8 are generated using both transmission and reflection signals. In addition, it is evident that the cross-range resolution, either in Fig. 2.17 or in Fig. 2.18, appears similar.

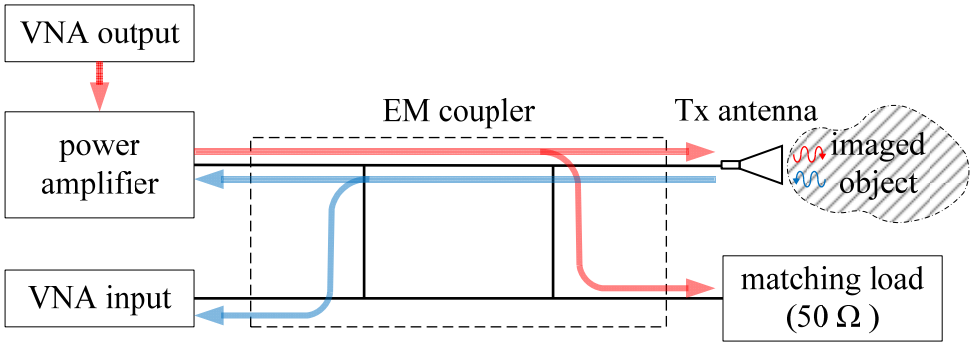

Fig. 2.19 Schematic diagram of the experimental setup for the reflection signal acquisition using a VNA, a power amplifier and a coupler.

The same study has been performed with measured data as well. The experimental system shown in Fig. 2.2 is adjusted so that reflection signals can be acquired. In the original experimental setup, the use of a directional device such as a power amplifier at the Tx output prevents the acquisition of reflection signals.

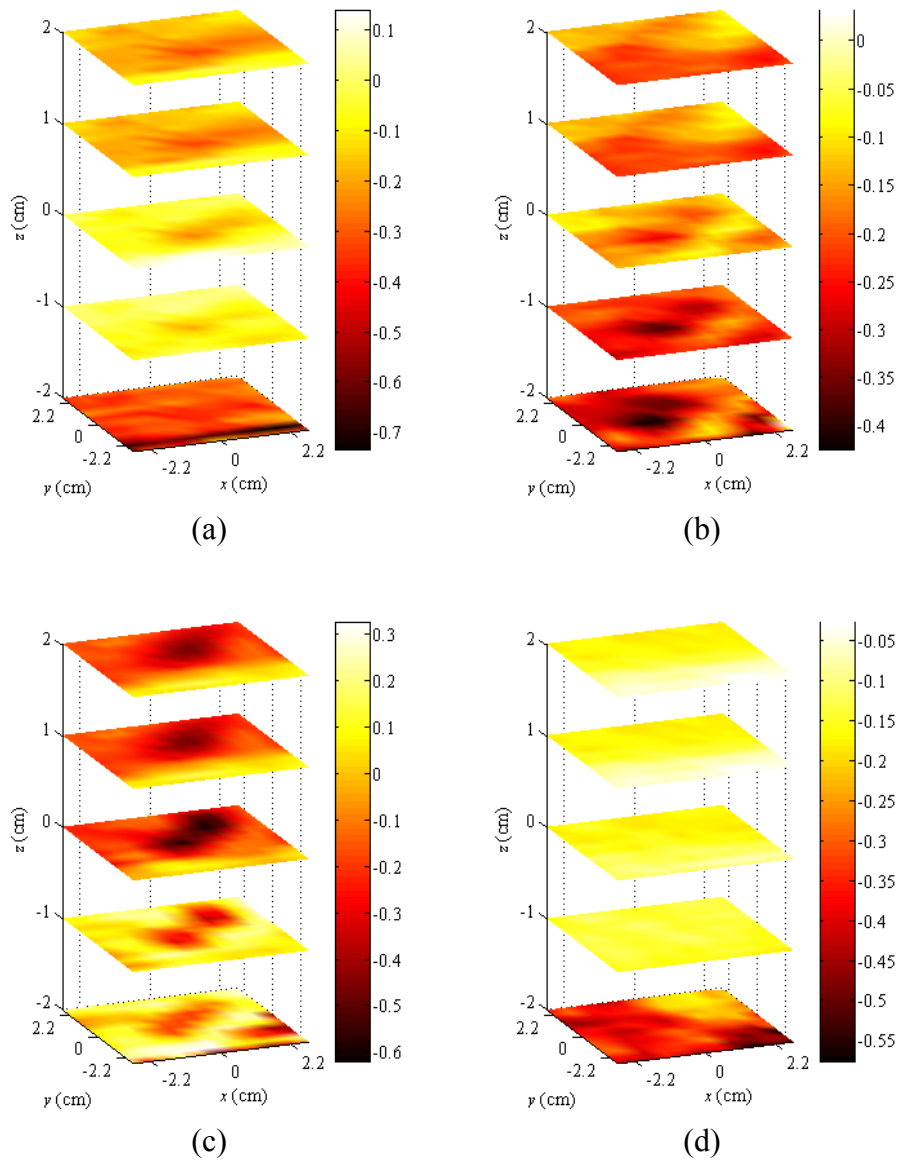

Fig. 2.20 3D normalized real maps of the two dielectric cylinders at: (a) 3.49 GHz, (b) 4.61 GHz, (c) 5.17 GHz, and (d) 7.69 GHz. Only reflection signals are used in this case.

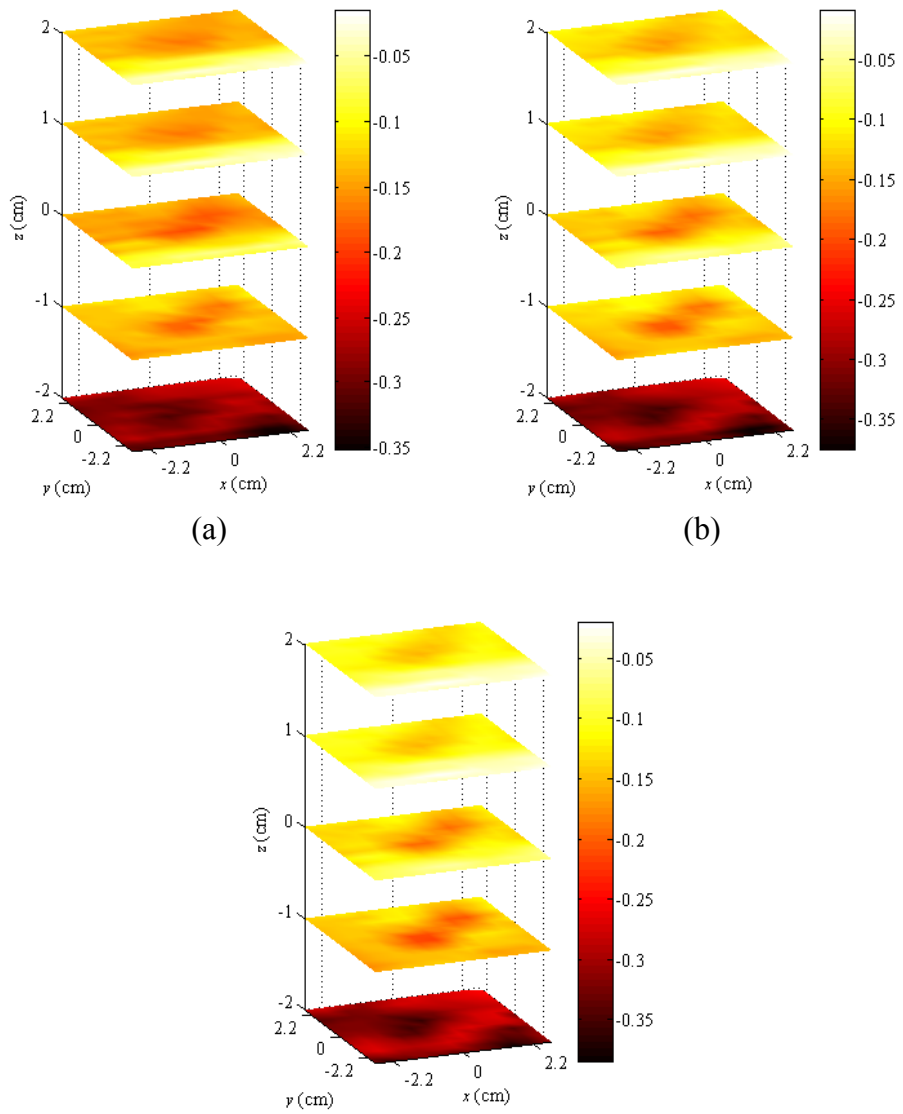

Fig. 2.21 3D frequency averaged real maps of the two dielectric cylinders over different frequency bands: (a) 3 GHz to 9 GHz, (b) 3 GHz to 7.2 GHz, and (c) 3.63 GHz to 7.2 GHz. Only reflection signals are used in this case.

Moreover, the VNA (ADVANTEST R3370) also has limited four ports. To solve this problem, a 20dB hybrid coupler is added between the antenna (i.e., the TEM horn) and the VNA as shown in Fig. 2.19. The signal from the VNA output is first boosted by the power amplifier and then fed to the Tx antenna via the coupler along the red path in Fig. 2.19. The reflected signal is picked up by the same antenna and transported to another VNA port via the coupler along the blue path in Fig. 2.19.

We revisit the experimental example in Section 2.3.5.1 where two dielectric cylinders are imaged. There, the two cylinders in the middle layer are successfully detected in the maps generated with only transmission signals; see Fig. 2.11 to Fig. 2.13. However, if we move the two cylinders from the middle layer (i.e., the $z' = 0$ cm plane) to one layer below (i.e., the $z' = -1$ cm plane) in the OUT and use transmission signals only, the imaging results remain similar to those in Fig. 2.11 to Fig. 2.13. In other words, the depth (range) position of the two cylinders is not captured in the maps. The lateral (cross-range) position is captured well.

Now, we use only reflection signals acquired with the adjusted scanning system to generate images. Fig. 2.20 shows the 3D normalized real-maps at frequencies of 3.49 GHz, 4.61 GHz, 5.17 GHz and 7.69 GHz, respectively. Fig. 2.20 (a) to (c) consistently show the two cylinders at the layer where they really reside, although Fig. 2.20 (d) fails to detect the targets due to the weak signal levels caused by the high-frequency attenuation. Additionally, strong artifacts can be seen at the very bottom layer (i.e., the $z' = -2$ cm plane) as well. In general, the depth of the

two dielectric cylinders is shown correctly. Again, this illustrates the importance of reflection signals to the range resolution. This result is predicted by the general theory of radar range and cross-range resolution [12][18].

Moreover, the image quality improves further after the frequency averaging. Fig. 2.21 shows the 3D frequency averaged real maps over different frequency bands: 3 GHz to 9 GHz, 3 GHz to 7.2 GHz and 3.63 GHz to 7.2 GHz, respectively. Compared with Fig. 2.20, the two cylinders are detected better at the $z' = -2$ cm plane where they really reside.

Nonetheless, the imaginary maps stay inclusive from the point view of detection, which may be due to the weak signal level.

To summarize, it is clear that the reflection signals are crucial for the range resolution of our imaging method when the planar raster-scanning acquisition is used. The phenomenon is well known and analyzed through numerous studies; see [11]-[12], [18]-[20].

2.5 CONCLUSIONS

A novel calibration technique is proposed for the sensitivity-based microwave imaging, which relies on the measurements of a known CO. The necessary incident-field information, previously derived from analytical or simulation models, can be acquired experimentally providing much better fidelity of the forward model. In

addition, lengthy EM simulations are avoided and replaced with the calibration procedure that characterizes the imaging system automatically, which is much appreciated in practical applications. Meanwhile, the speed of the inversion procedure is not affected and remains fast enough to allow for real-time imaging.

To reduce the number of CO measurements to an acceptable level, coordinate translation is recommended. This is admissible when the background medium is uniform or translationally invariant.

Finally it should be noted that, the concept of system calibration via known objects may be valuable in other imaging modalities such as ultrasound, photonic imaging, electrical-impedance tomography, etc., since all of them depend critically on the assumed forward model.

The sensitivity-based imaging employing the proposed calibration technique is validated via synthetic and experimental examples using the planar raster-scanning system. In each example, the targets can be successfully detected.

The importance of the reflection signals has been unambiguously demonstrated via additional studies, proving that they are critical for the imaging range resolution.

Finally, it is worth emphasizing that the imaging method at its current form, although armed with calibration technique, is still a qualitative imaging approach.

REFERENCES

[1] Y. Song and N. K. Nikolova, "Memory-efficient method for wideband self-adjoint sensitivity analysis," *IEEE Trans. Microw. Theory Tech.*, vol. 56, no. 8, pp. 1917−1927, Aug. 2008.

[2] L. Liu, A. Trehan, and N. K. Nikolova, "Near-field detection at microwave frequencies based on self-adjoint response sensitivity analysis," *Inverse Problems*, vol. 26, 105001, 2010.

[3] Y. Zhang, S. Tu, R. K. Amineh and N. K. Nikolova, "Resolution and robustness to noise of the sensitivity-based method for microwave imaging with data acquired on cylindrical surfaces," *Inverse Problems*, vol. 28, 115006, 2012.

[4] N. K. Nikolva, X. Zhu, Y. Song, A. Hasib, and M. H. Bakr, "*S*-parameter sensitivities for electromagnetic optimization based on volume field solutions," *IEEE Trans. Microw. Theory Tech.*, vol. 57, no. 6, pp. 1526−1538, June 2009.

[5] M. S. Dadash, N. K. Nikolova, and J. W. Bandler, "Analytical adjoint sensitivity formula for the scattering parameters of metallic structures," *IEEE Trans. Microw. Theory Tech.*, vol. 60, no. 9, pp. 2713−2722, Sept. 2012.

[6] T. G. Savelyev and A. G. Yarovoy, "Fast image by 3-D deconvolution in short-range UWB radar for concealed weapon detection," *The 9th European*

Radar Conf. (EuRAD 2012), pp. 26−29, Oct. 2012.

[7] T. Sakamoto, T. G. Savelyev, P. Aubry, and A. G. Yarovoy, "Fast range point migration method for weapon detection using ultra-wideband radar," *The 9th European Radar Conf. (EuRAD 2012)*, pp. 230−233, Oct. 2012.

[8] W. C. Chew, *Waves and Fields in Inhomogeneous Media*, New York: IEEE Press, 1995.

[9] L. E. Larsen and J. H. Jacobi, *Medical Applications of Microwave Imaging*, New York: IEEE, 1986.

[10] C. Yu, M. Yuan, Y. Zhang, J. Stang, R. T. George, G. A. Ybarra, W. T. Joines, and Q. H. Liu, "Microwave imaging in layered media: 3-D image reconstruction from experimental data," *IEEE Trans. Antennas Propag.*, vol. 58, no. 2, pp. 440−448, Feb. 2010.

[11] M. Ravan, R. K. Amineh, and N. K. Nikolova, "Two-dimensional near-field microwave holography," *Inverse Problems*, vol. 26, 055011, 2010.

[12] R. K. Amineh, M. Ravan, N. K. Nikolova, and A. Khalatpour, "Three-dimensional near-field microwave holography using reflected and transmitted signals," *IEEE Trans. Antennas Propag.*, vol. 59, no. 12, pp. 4777−4789, Dec. 2011.

[13] Y. Zhang, S. Tu, R. K. Amineh, and N. K. Nikolova, "Sensitivity-based microwave imaging with raster scanning," *2012 IEEE MIT-S Int. Microw. Symp. Dig.*, pp. 1-3, June 2012.

[14] R. K. Amineh, J. J. McCombe, A. Khalatpour, and N. K. Nikolova, "Microwave holography using point-spread functions measured with calibration objects," *IEEE Trans. Instrument. Meas.*, vol. 64, no. 2, pp. 403−417, Feb. 2015.

[15] The MathWorks, MATLAB. Natick, MA, USA, Feb. 2010, [Online] http://www.mathworks.com/products/matlab

[16] R. K. Amineh, M. Ravan, A. Trehan, and N. K. Nikolova, "Near-field microwave imaging based on aperture raster scanning with TEM horn antennas," *IEEE Trans. Antennas Propag.*, vol. 59, no. 3, pp. 928−940, Mar. 2011.

[17] Emerson&Cuming Microwave Products, Inc., Randolph, MA, US.

[18] I. Walterscheid, A. R. Brenner, and J. H. G. Ender, "Results on bistatic synthetic aperture radar," *IEEE Electron. Lett.*, vol. 40, no. 19, pp. 1224−1225, 2004.

[19] D. Sheen, D. McMakin, and T. Hall, "Near-field three-dimensional radar imaging techniques and applications," *Applied Optics*, vol. 49, no. 19, pp. E83−E93, 2010.

[20] D. J. Kurrant and E. C. Fear, "An improved technique to predict the time-of-arrival of a tumor response in radar-based breast imaging," *IEEE Trans. Biomed. Eng.*, vol. 56, no. 4, pp. 1200−1208, 2009.

Chapter 3

Fast Quantitative Microwave Imaging

3.1 INTRODUCTION

As discussed in Chapter 1, the imaging approaches can be divided into two types: the qualitative and the quantitative approaches. The goal of the quantitative imaging is to reconstruct the dielectric-property distribution inside the imaged object. However, most of the quantitative imaging techniques, e.g., the Born iterative methods [1]-[2] and the model-based optimization methods [3], are time-consuming due to the employment of numerical forward models (e.g., EM simulations) in their iterative strategies. Until now, our sensitivity-based microwave imaging, although very efficient computationally, has been a qualitative method.

In this chapter, we proposed a novel quantitative imaging method with real-time performance, which also applies the calibration technique introduced in Section 2.3 of Chapter 2 and bears certain similarities with the original sensitivity-based imaging. Measurements are required to be performed on three different objects, i.e., the RO, the CO and the OUT.

The responses acquired through the CO measurements represent the system's point-spread function (PSF) that, mathematically, is the product of the Rx antenna

polarization vector, the RO Green's function, the total field at the CO center, and the known CO contrast. A resolvent kernel in the forward model can be extracted from the system's PSF, which includes the particulars of the measurement setup, including all Tx and Rx antennas. The scattering from any OUT can be expressed as the convolution of the resolvent kernel with its property distribution. Unlike other deconvolution techniques, e.g., [4]-[5], here the inversion is performed in real space without applying Fourier transforms. The direct-inversion approach, similar to the sensitivity-based imaging, is primarily applied to generate *power maps* for the COs and the OUT, which are qualitative results. By interpreting the power maps of both the CO and the OUT in the least-square sense, quantitative images can be eventually achieved.

Theoretically, we show that the proposed method is subject to limitations more relaxed than those of the linear Born approximation. In its current form, the major limitation of the approach is that the mutual coupling among the scattering centers (e.g., multiple scattering) is not taken into account. It may lead to image artifacts in the case of prominent multiple scattering. However, the method can be used to provide a good starting point for an iterative reconstruction toward a refine image. Also, it is shown that better estimation accuracy can be achieved when the small scatterer in the CO has properties comparable to the examined voxel in the OUT.

The imaging procedure is summarized below for the planar raster-scanning system. Since the method does not need analytical or numerical approximations of the forward model, it is particularly valuable in short-range imaging applications, where such analytical models do not exist while the fidelity of the simulation models is often inadequate.

The proposed technique is demonstrated and validated through an example using simulated data. 3D quantitative imaging results are given in the example with discussions. The *relative root-mean-square error* (RRMSE) is also defined here to evaluate the estimation accuracy of the technique.

3.2 EXTRACTION OF RESOLVENT KERNEL OF THE IMAGING SYSTEM

In Chapter 2, the scattered field can be computed by the scattering integral (2.2), which is related to the *S*-parameter response difference via (2.6). Here, we express the relation between the *S*-parameter response difference and the scattered field in a more generic form. Staying with the microwave network of N_{r} receivers and N_{t} transmitters, when the *j*-th Tx antenna is excited by a voltage $V_j^{(m)}$, it generates the field $\mathbf{E}_j^{(m)}$, which induces the voltage signal $V_i^{(m)}$ at the terminals of the *i*-th Rx antenna. For the *m*-th frequency, the respective *S*-parameter signal

$S_n^{(m)} \equiv S_{ij}^{(m)} = V_i^{(m)} \big/ V_j^{(m)}$ is a linear functional of $\mathbf{E}_j^{(m)}$:

$$S_n^{(m)} = R_i^{(m)} \left\{ \overline{\mathbf{E}}_j^{(m)}(\mathbf{r}) \right\}, \tag{3.1}$$

where $\mathbf{r}$ denotes position in the observation domain, $R_i^{(m)}\{\ \}$ is the linear operator, which describes how the i-th Rx antenna converts the field distribution in its vicinity into a voltage signal, and $\overline{\mathbf{E}}_j^{(m)}(\mathbf{r}) = \mathbf{E}_j^{(m)}(\mathbf{r}) / V_j^{(m)}$ is the normalized field distribution. To simplify the notations, in the following, the normalized field distribution will be simply denoted as $\mathbf{E}_j^{(m)}(\mathbf{r})$.

In the p-th CO, the "point" scatterer (i.e., the small voxel-size scatterer with known property contrast $\delta\varepsilon_{\mathrm{CO}}^{(m)}$) is placed at the p-th voxel. Given (3.1), the scattered signals of the p-th CO become

$$\Delta S_{\mathrm{CO},\,p,\,n}^{(m)} = R_i^{(m)} \left\{ \overline{\mathbf{E}}_{\mathrm{CO},\,p,\,j}^{(m)\mathrm{sc}}(\mathbf{r}) \right\}. \tag{3.2}$$

Substituting the scattering integral (2.2) into (3.2), we have

$$\Delta S_{\mathrm{CO},\,p,\,n}^{(m)} \approx R_i^{(m)} \left\{ \int_{V_p} k_m^2 \Delta\varepsilon^{(m)}(\mathbf{r}'_p) \underline{\mathbf{G}}(\mathbf{r}_i, \mathbf{r}'_p) \cdot \mathbf{E}_j^{(m)\mathrm{tot}}(\mathbf{r}'_p) d\mathbf{r}'_p \right\}, \ \mathbf{r}'_p \in V_p, \tag{3.3}$$

where V_p is the volume of the voxel-size scatterer at the p-th voxel. Given that V_p is sufficiently small and $\Delta\varepsilon^{(m)}(\mathbf{r}'_p) = \delta\varepsilon_{\mathrm{CO}}^{(m)}$, (3.3) can be approximated as

$$\Delta S_{\mathrm{CO},\,p,\,n}^{(m)} \approx k_m^2 \Omega_{\mathrm{v}} \delta\varepsilon_{\mathrm{CO}}^{(m)} R_i^{(m)} \left\{ \underline{\mathbf{G}}(\mathbf{r}_i, \mathbf{r}'_p) \cdot \mathbf{E}_{\mathrm{CO},\,p,\,j}^{(m)\mathrm{tot}}(\mathbf{r}'_p) \right\}, \tag{3.4}$$

where Ω_{v} is the voxel size and $\mathbf{E}_j^{(m)\mathrm{tot}}(\mathbf{r}'_p) \equiv \mathbf{E}_{\mathrm{CO},\,p,\,j}^{(m)\mathrm{tot}}(\mathbf{r}'_p)$ is the internal total field. The expression in (3.4) is the p-th PSF of the imaging system representing the

system response to a point scatterer at the p-th voxel. If the system is invariant upon translation or rotation, this PSF can be used to characterize the n-th system response to point scatterers at other locations by making use of coordinate translations. Also, note that no approximation of the internal total field (e.g., it has not been assumed equal to the incident field as in the linear Born approximation) used in (3.4).

Further, due to the small size of the scatterer, the internal total field $\mathbf{E}^{(m)\mathrm{tot}}_{\mathrm{CO},\,p,\,j}(\mathbf{r}'_p)$ can be approximated through a linear relationship to the internal incident field, i.e.,

$$\mathbf{E}^{(m)\mathrm{tot}}_{\mathrm{CO},\,p,\,j}(\mathbf{r}'_p) \approx \underline{\mathbf{\Gamma}}^{(m)}_{\mathrm{CO}} \cdot \mathbf{E}^{(m)}_{\mathrm{RO},\,j}(\mathbf{r}'_p)\,, \tag{3.5}$$

which is in accordance with the well-known localized nonlinear (LN) [6] and quasi-analytic (QA) [7]-[9] approximations. In (3.5), the tensor $\underline{\mathbf{\Gamma}}^{(m)}_{\mathrm{CO}}$ depends on the contrast $\delta\varepsilon^{(m)}_{\mathrm{CO}}$ and the shape of the small target. It tends to the identity tensor $\underline{\mathbf{I}}$ asymptotically as $\delta\varepsilon^{(m)}_{\mathrm{CO}}$ decreases, leading to the linearized Born model of scattering. Also, in the static limit of the LN approximation and in the QA approximation, $\underline{\mathbf{\Gamma}}^{(m)}_{\mathrm{CO}} = \Gamma^{(m)}_{\mathrm{CO}}\underline{\mathbf{I}}$ where $\Gamma^{(m)}_{\mathrm{CO}}$ is a scalar. Using (3.5), (3.4) can be rearranged as

$$R^{(m)}_i \left\{ \underline{\mathbf{G}}(\mathbf{r},\mathbf{r}'_p) \cdot \mathbf{E}^{(m)\mathrm{tot}}_{\mathrm{RO},\,j}(\mathbf{r}'_p) \right\} \approx \frac{\Delta S^{(m)}_{\mathrm{CO},\,p,\,n}}{k_m^2 \Omega_{\mathrm{v}} \Gamma^{(m)}_{\mathrm{CO}} \delta\varepsilon^{(m)}_{\mathrm{CO}}}, \;\; p = 1,\ldots,N_{\mathrm{v}}. \tag{3.6}$$

This is the resolvent kernel of the scattering problem specific to the data-acquisition system.

Analogously to (3.4), the scattering integral is written in terms of the scattered signal $\Delta S_{\mathrm{OUT},\,n}^{(m)}$ acquired with the OUT as

$$\Delta S_{\mathrm{OUT},\,n}^{(m)} \approx k_m^2 \int_V R_i^{(m)} \left\{ \underline{\mathbf{G}}(\mathbf{r},\mathbf{r}') \cdot \mathbf{E}_{\mathrm{OUT},\,j}^{(m)\mathrm{tot}}(\mathbf{r}') \right\} \Delta\varepsilon_{\mathrm{OUT}}^{(m)}(\mathbf{r}') d\mathbf{r}' . \tag{3.7}$$

This is the integral equation to be solved for the unknown contrast $\Delta\varepsilon_{\mathrm{OUT}}^{(m)}(\mathbf{r}')$, i.e.,

$$\Delta\varepsilon_{\mathrm{OUT}}^{(m)}(\mathbf{r}') = \varepsilon_{\mathrm{OUT}}^{(m)}(\mathbf{r}') - \varepsilon_{\mathrm{RO}}^{(m)}(\mathbf{r}') . \tag{3.8}$$

Neglecting the coupling among the scattering voxels and employing the linear relationship (3.5) between the total field in the OUT and that in the RO, (3.7) can be expressed in terms of the resolvent kernel (3.6) as

$$\Delta S_{\mathrm{OUT},\,n}^{(m)} \approx k_m^2 \int_V R_i^{(m)} \left\{ \underline{\mathbf{G}}(\mathbf{r},\mathbf{r}') \cdot \mathbf{E}_{\mathrm{RO},\,j}^{(m)\mathrm{tot}}(\mathbf{r}') \right\} \Gamma_{\mathrm{OUT}}^{(m)}(\mathbf{r}') \Delta\varepsilon_{\mathrm{OUT}}^{(m)}(\mathbf{r}') d\mathbf{r}' . \tag{3.9}$$

Thus, (3.6) and (3.9) allow for the expression of the OUT data $\Delta S_{\mathrm{OUT},\,n}^{(m)}$, m = 1, …, N_{f}, n = 1, …, N_{s}, in terms of the data acquired with the known CO:

$$\Delta S_{\mathrm{OUT},\,n}^{(m)} \approx k_m^2 \int_V \left[\frac{\Delta S_{\mathrm{CO},\,p,\,n}^{(m)}}{k_m^2 \Omega_{\mathrm{v}} \delta\varepsilon_{\mathrm{CO}}^{(m)} \Gamma_{\mathrm{CO}}^{(m)}} \right] \Gamma_{\mathrm{OUT}}^{(m)}(\mathbf{r}') \Delta\varepsilon_{\mathrm{OUT}}^{(m)}(\mathbf{r}') d\mathbf{r}' . \tag{3.10}$$

Here, all terms in the square brackets are known. The forward model in (3.10) inherently incorporates the Green function of the particular imaging system and the internal total field inside a small scatterer, which is more reliable than the analytical or simulation models. The direct inversion approaches [10]-[18], employing analytical or simulation forward models, rely on the linear Born approximation where the total internal field is replaced by its incident counterpart. This not only

results in the inability to perform quantitative imaging but it also leads to limitations on the size and contrast of the reconstructed objects [19][21]. In fact, as shown later, the closer $\delta\varepsilon_{\mathrm{CO}}^{(m)}$ is to $\Delta\varepsilon_{\mathrm{OUT}}^{(m)}(\mathbf{r}')$, the closer the ratio $\Gamma_{\mathrm{OUT}}^{(m)}(\mathbf{r}')/\Gamma_{\mathrm{CO}}^{(m)}$ is to unity.

3.3 THE POWER MAPS

Assuming that $\Gamma_{\mathrm{OUT}}^{(m)}(\mathbf{r}'_p)\big/\Gamma_{\mathrm{CO}}^{(m)} \approx 1$ and discretizing the integral into a sum over the contributions of all voxels, (3.10) becomes

$$\Delta S_{\mathrm{OUT},\,n}^{(m)} \approx \sum_{p=1}^{N_{\mathrm{v}}} \frac{\Delta\varepsilon_{\mathrm{OUT}}^{(m)}(\mathbf{r}'_p)}{\delta\varepsilon^{(m)}} \Delta S_{\mathrm{CO},\,p,\,n}^{(m)} . \tag{3.11}$$

Here, $\Delta S_{\mathrm{CO},\,p,\,n}^{(m)}$ is the n-th response at the m-th frequency acquired with the p-th CO, in which the known voxel-size scatterer is positioned at the p-th voxel. By introducing the ratio $\tau_p^{(m)}$ of $\Delta\varepsilon_{\mathrm{OUT}}^{(m)}(\mathbf{r}'_p)$ and $\delta\varepsilon_{\mathrm{CO}}^{(m)}$, so that

$$\Delta\varepsilon_{\mathrm{OUT}}^{(m)}(\mathbf{r}'_p) = \tau_p^{(m)} \delta\varepsilon_{\mathrm{CO}}^{(m)} . \tag{3.12}$$

(3.11) can be stated simply as

$$\Delta S_{\mathrm{OUT},\,n}^{(m)} \approx \sum_{p=1}^{N_{\mathrm{v}}} \tau_p^{(m)} \Delta S_{\mathrm{CO},\,p,\,n}^{(m)} . \tag{3.13}$$

This suggests that the n-th OUT signal can be expressed as the weighted sum of all N_{v} CO signals.

We next define the *power map* of the OUT at the m-th frequency so that the map's value at the p-th voxel is the sum of the product of $\Delta S_{\mathrm{OUT},\,n}^{(m)} \cdot \left[\Delta S_{\mathrm{CO},\,p,\,n}^{(m)}\right]^*$ over all available signals, $n = 1, 2, \ldots, N_{\mathrm{s}}$:

$$M_{\mathrm{OUT}}^{(m)}(\mathbf{r}'_p) = \sum_{n=1}^{N_{\mathrm{s}}} \Delta S_{\mathrm{OUT},\,n}^{(m)} \cdot \left[\Delta S_{\mathrm{CO},\,p,\,n}^{(m)}\right]^*, \quad p = 1, \ldots, N_{\mathrm{v}}, \tag{3.14}$$

where $\left[\Delta S_{\mathrm{CO},\,p,\,n}^{(m)}\right]^*$ is the complex conjugate of $\Delta S_{\mathrm{CO},\,p,\,n}^{(m)}$.

It is clear that the power map is generated in a similar manner as the Jacobian map or sensitivity map in the sensitivity-based imaging method; see (2.22) in Chapter 2. Here, the only difference is that the result is scaled by a factor of $-\delta\varepsilon_{\mathrm{CO}}^{(m)} \cdot N_{\mathrm{s}}$ since the response derivative $\partial S_{\mathrm{RO},\,n}^{(m)} \big/ \partial \varepsilon_{\mathrm{RO}}^{(m)}(\mathbf{r}'_p) \approx \Delta S_{\mathrm{CO},\,p,\,n}^{(m)} \big/ \delta\varepsilon_{\mathrm{CO}}^{(m)}$ in (2.22) is here replaced by $\Delta S_{\mathrm{CO},\,p,\,n}^{(m)}$, and we neglect the minus sign to have a neat expression of power maps.

The ability of the power map to represent the presence of scattering objects in the OUT can be explained as follows. The complex-valued product $\Delta S_{\mathrm{OUT},\,n}^{(m)} \cdot [\Delta S_{\mathrm{CO},\,p,\,n}^{(m)}]^*$ can be viewed as the m-th Fourier component of the cross-correlation between the n-th OUT signal and the n-th CO signal with a point scatterer at $\mathbf{r}'_p$. As such, it is a measure of the similarity of these two signals. If the p-th voxel in the OUT indeed scatters at this frequency, the above product is expected to have a significant magnitude and a near-zero phase for all N_{s} terms in (3.14), which

correspond to all available responses collected by all sensors over the entire acquisition surface. Summing up all N_s terms would lead to their coherent addition. Thus, the "power signature" associated with the *p*-th voxel would be large. Conversely, if there is no scattering associated with the *p*-th voxel in the OUT at this frequency, then the products $\Delta S_{\mathrm{OUT},n}^{(m)} \cdot [\Delta S_{\mathrm{CO},p,n}^{(m)}]^*$, $n = 1, \ldots, N_s$, are expected to have relatively small magnitudes and random phases, leading to an incoherent addition and, as a consequence, a small "power signature" associated with the *p*-th voxel. The term "power signature" is appropriate here given that the magnitude of each signal $|\Delta S_{\mathrm{OBJ},n}^{(m)}|$ (OBJ $\equiv$ CO, OUT) is proportional to the square root of the ratio of the received-to-transmitted power.

The power map also bears mathematical similarity to back-propagation or time-reversal schemes, although here the Tx and Rx arrays need not be co-located. This becomes clear if (3.13) is viewed as the system of data equations $\boldsymbol{A\tau} = \boldsymbol{b}$ where the vector $\boldsymbol{b}$ consists of the OUT data $\Delta S_{\mathrm{OUT},n}^{(m)}$ ($n = 1, \ldots, N_s$), $\boldsymbol{\tau}$ is the vector of the unknown contrast values $\tau_p^{(m)}$ ($p = 1, \ldots, N_v$), and $\boldsymbol{A}$ is the $N_s \times N_v$ system matrix built from the measured PSFs of the acquisition system. In the context of time reversal, $\boldsymbol{A}$ can be viewed as a discrete representation of the measured *background coherent point-spread function* [21]. Therefore, the quantity $\boldsymbol{A}^* \cdot \boldsymbol{b}$, equivalent to the power map definition in (3.14), can be viewed as an estimate of the projection of the data onto the space defined by the system singular vectors.

To this end, the power maps yield only *qualitative imaging* results, i.e., there is no property estimation involved. With wideband data, the OUT power maps at all frequencies are usually combined (often after proper normalization [17]-[18]) to obtain a single qualitative image of the OUT.

To gain a deeper insight into the power map, we substitute (3.13) into (3.14) and obtain

$$M_{\mathrm{OUT}}^{(m)}(\mathbf{r}'_p) = \sum_{n=1}^{N_{\mathrm{s}}} \sum_{q=1}^{N_{\mathrm{v}}} \tau_q^{(m)} \Delta S_{\mathrm{CO},q,n}^{(m)} \cdot \left[\Delta S_{\mathrm{CO},p,n}^{(m)} \right]^* \tag{3.15}$$

Writing out (3.15) for all N_{v} voxels leads to a linear system of N_{v} equations:

$$\left| \begin{array}{l} M_{\mathrm{OUT}}^{(m)}(r_1') = M_{11}^{(m)} \tau_1^{(m)} + \cdots + M_{1N_{\mathrm{v}}}^{(m)} \tau_{N_{\mathrm{v}}}^{(m)} \\ \quad \vdots \\ M_{\mathrm{OUT}}^{(m)}(r_{N_{\mathrm{v}}}') = M_{N_{\mathrm{v}}1}^{(m)} \tau_1^{(m)} + \cdots + M_{N_{\mathrm{v}}N_{\mathrm{v}}}^{(m)} \tau_{N_{\mathrm{v}}}^{(m)}, \end{array} \right. \tag{3.16}$$

where

$$M_{pq}^{(m)} = \sum_{n=1}^{N_{\mathrm{s}}} \Delta S_{\mathrm{CO},q,n}^{(m)} \cdot \left[\Delta S_{\mathrm{CO},p,n}^{(m)} \right]^* . \tag{3.17}$$

Comparing (3.17) and (3.14), we see that $M_{pq}^{(m)}$ is in fact the value at the p-th voxel of the power map of the CO which has the voxel-size scatterer at the q-th voxel, i.e., $M_{pq}^{(m)} = M_{\mathrm{CO},q}^{(m)}(\mathbf{r}'_p)$. Note that when $p \neq q$, $M_{\mathrm{CO},q}^{(m)}(\mathbf{r}'_p)$ is not necessarily zero but it is expected to be small in magnitude and increasingly so as the distance between the p-th and q-th voxels increases. On the other hand, when $q = p$, (3.17) becomes

$$M_{pp}^{(m)} \equiv M_{\mathrm{CO},p}^{(m)}(\mathbf{r}'_p) = \sum_{n=1}^{N_{\mathrm{s}}} \left| \Delta S_{\mathrm{CO},p,n}^{(m)} \right|^2 \tag{3.18}$$

which is the maximum attainable power value among all voxels and it is equal to the combined scattered power of the target at the p-th voxel (normalized to the Tx power) collected by all receivers.

3.4 ESTIMATION OF DIELECTRIC PROPERTIES

First, the linear system (3.16) is written in matrix form

$$\boldsymbol{M}^{(m)}\boldsymbol{\tau}^{(m)} = \boldsymbol{m}^{(m)}, \tag{3.19}$$

where

$$\boldsymbol{M}^{(m)} = \begin{bmatrix} M_{\mathrm{CO},1}^{(m)}(\mathbf{r}_1') & \cdots & M_{\mathrm{CO},N_\mathrm{v}}^{(m)}(\mathbf{r}_1') \\ \vdots & & \vdots \\ M_{\mathrm{CO},1}^{(m)}(\mathbf{r}_{N_\mathrm{v}}') & \cdots & M_{\mathrm{CO},N_\mathrm{v}}^{(m)}(\mathbf{r}_{N_\mathrm{v}}') \end{bmatrix}, \tag{3.20}$$

$$\boldsymbol{\tau}^{(m)} = [\tau_1^{(m)} \ \cdots \ \tau_{N_\mathrm{v}}^{(m)}]^T, \tag{3.21}$$

and

$$\boldsymbol{m}^{(m)} = [M_{\mathrm{OUT}}^{(m)}(\mathbf{r}_1') \ \cdots \ M_{\mathrm{OUT}}^{(m)}(\mathbf{r}_{N_\mathrm{v}}')]^T. \tag{3.22}$$

The system matrix $\boldsymbol{M}^{(m)}$ is an $N_\mathrm{v} \times N_\mathrm{v}$ square matrix consisting of the CO power maps (the power map of the CO with a voxel-size scatterer at the p-th voxel, i.e., the p-th CO map, is in the p-th column of $\boldsymbol{M}^{(m)}$. $\boldsymbol{m}^{(m)}$ is an $N_\mathrm{v} \times 1$ vector containing the OUT power map, and $\boldsymbol{\tau}^{(m)}$ is an $N_\mathrm{v} \times 1$ vector of the unknown property contrast ratios defined by (3.12).

To build $\boldsymbol{M}^{(m)}$, all necessary CO measurements must be performed and the respective CO power maps to be built using (3.17). To build $\boldsymbol{m}^{(m)}$, the OUT measurements are needed from which the OUT power map is built using (3.14). Since the small scatterer in the CO has known dielectric-property contrast $\delta\varepsilon_{\mathrm{CO}}^{(m)}$, once $\boldsymbol{\tau}^{(m)}$ is obtained by solving (3.19), then the property contrast $\Delta\varepsilon_{\mathrm{OUT}}^{(m)}(\mathbf{r}'_p)$ of the OUT can be computed using (3.12). Finally, the actual property values of the OUT can be calculated from $\Delta\varepsilon_{\mathrm{OUT}}^{(m)}(\mathbf{r}'_p)$ and the known background permittivity $\varepsilon_{\mathrm{RO}}^{(m)}(\mathbf{r}'_p)$ using (3.8).

The method of solving (3.19) is critical to the speed of the reconstruction. It is, therefore, important to examine the properties of the system matrix $\boldsymbol{M}^{(m)}$, the q-th column of which contains the q-th CO map. Ideally, the q-th CO map should behave as a delta function, namely,

$$M_{\mathrm{CO},\,q}^{(m)}(r'_p)\begin{cases}\neq 0, & p=q,\\ =0, & p\neq q.\end{cases} \tag{3.23}$$

Such ideal images of a point scatterer could be obtained only with infinitesimal spatial resolution (e.g., the wavelength is very short) and noise-free measurements. In this ideal case, $\boldsymbol{M}^{(m)}$ is a diagonal matrix, with all of its diagonal elements being nonzero; it is well-conditioned and is easily invertible.

Next, let us consider the extreme opposite case where the whole imaged volume is below the spatial resolution limit (e.g., the sample frequency is very low).

Then all map values in $M_{\mathrm{CO},q}^{(m)}(\mathbf{r}'_p)$ become very similar. As a result, the condition number $\kappa\left[\boldsymbol{M}^{(m)}\right]$ of the system matrix $\boldsymbol{M}^{(m)}$ approaches infinity and it cannot be inverted.

Also, due to the large matrix size, the solution of (3.19) through direct inversion or *LU* (lower upper) decomposition, is not practical. Here, (3.19) is solved as a linear LS (least square) problem, which can be cast into the form of

$$\boldsymbol{\tau}_*^{(m)} = \arg\min_{\boldsymbol{\tau}^{(m)}} \left\| \boldsymbol{M}^{(m)}\boldsymbol{\tau}^{(m)} - \boldsymbol{m}^{(m)} \right\|, \tag{3.24}$$

where $\|\cdot\|$ is the l_2 norm and $\boldsymbol{\tau}_*^{(m)}$ is the optimal solution. A good initial guess $\boldsymbol{\tau}_0^{(m)}$ in solving (3.24) iteratively is obtained from (3.23), i.e., ignoring the off-diagonal elements of $\boldsymbol{M}^{(m)}$:

$$\left[\tau_0^{(m)}\right]_p = \frac{M_{\mathrm{OUT}}^{(m)}(\mathbf{r}'_p)}{M_{\mathrm{CO},p}^{(m)}(\mathbf{r}'_p)},\ p = 1,\ldots,N_{\mathrm{v}}. \tag{3.25}$$

Once the solution $\boldsymbol{\tau}_*^{(m)}$ of (3.24) is available, the estimated property distribution of the OUT at the *m*-th frequency is calculated as

$$\varepsilon_{\mathrm{OUT}}^{(m)}(\mathbf{r}'_p) = \varepsilon_{\mathrm{RO}}^{(m)}(\mathbf{r}'_p) + \left[\tau_*^{(m)}\right]_p \delta\varepsilon_{\mathrm{CO}}^{(m)},\ p = 1,\ldots,N_{\mathrm{v}}. \tag{3.26}$$

In order to evaluate the accuracy of the property estimation in all subsequent examples, we define the RRMSE (relative root-mean-square error) as

$$\text{RRMSE}=\sqrt{\frac{1}{N_{\text{v}}}\sum_{p=1}^{N_{\text{v}}}\frac{\left|\varepsilon_{\text{OUT}}^{(m)}(\mathbf{r}'_p)-\bar{\varepsilon}_{\text{OUT}}^{(m)}(\mathbf{r}'_p)\right|^2}{\left|\bar{\varepsilon}_{\text{OUT}}^{(m)}(\mathbf{r}'_p)\right|^2}}\,, \tag{3.27}$$

where $\varepsilon_{\text{OUT}}^{(m)}(\mathbf{r}'_p)$ is the estimate from (3.26) and $\bar{\varepsilon}_{\text{OUT}}^{(m)}(\mathbf{r}'_p)$ is the true property distribution of the OUT.

We note that, in principle, the $\tau^{(m)}$ coefficients could also be found by solving (3.13) directly, i.e., without constructing the power maps first. Note that (3.13) can be cast as a rectangular system $\boldsymbol{A\tau}=\boldsymbol{b}$. However, if the data $\boldsymbol{b}$ are not entirely in the range of the forward operator (represented by $\boldsymbol{A}$), then such direct solution will not produce a valid result. On the other hand, under the same conditions, the system $\boldsymbol{A}^*\boldsymbol{A\tau}=\boldsymbol{A}^*\boldsymbol{b}$, which is in effect (3.19), may have a solution and this solution will minimize the LS error of (3.13); see, for example [21]. This also explains why it is advantageous to obtain $\boldsymbol{A}$ experimentally as this provides the physically correct functional space spanning all possible response functions acquired with the particular setup.

In addition, constructing the power maps brings the following three advantages. (i) The images provided by the absolute values of the power maps are generated practically instantaneously, which enables real-time qualitative imaging. (ii) A good initial guess of the OUT property distribution can be obtained once the power maps are generated; see (3.25). This is critical in dealing with nonuniqueness and in accelerating the iterative solution to (3.24). (iii) Multi-frequency data

combination is efficiently done using the power maps (see Section 3.6C below) thus enabling fast processing of wideband data where we may be dealing with thousands of frequency points. Such number of data points would render the direct solution of (3.13) impractical.

3.5 METHOD LIMITATIONS

The reconstruction method described above rests on the forward model in (3.11) obtained through two assumptions: (i) the mutual coupling between the scattering centers and the multiple scattering effects in the OUT are negligible, which reduces (3.7) to (3.9), and (ii) the ratio $\Gamma_{\mathrm{OUT}}^{(m)}(\mathbf{r}'_p)/\Gamma_{\mathrm{CO}}^{(m)}$ is close to unity, which reduces (3.10) to (3.11).

The first limitation is typical for all direct-inversion methods. If multiple-scattering effects are prominent in the OUT, they would lead to image artifacts. Such artifacts could be suppressed if the property reconstruction obtained with the proposed method is further refined using an iterative technique such as the iterative Born method [1], the distorted Born iterative method [2], or a model-based optimization method [3].

We next examine the limitations stemming from the assumption that the ratio $\Gamma_{\mathrm{OUT}}^{(m)}(\mathbf{r}'_p)/\Gamma_{\mathrm{CO}}^{(m)}$ is close to unity. As shown in [6], at the low-frequency (or DC) limit

of the local nonlinear approximation, the coefficient $\Gamma_{\mathrm{OBJ}}^{(m)}$, relating the internal total field to the internal incident field in a sufficiently small spherical scatterer is given by

$$\Gamma_{\mathrm{OBJ}}^{(m)} \approx \frac{3\varepsilon_{\mathrm{RO}}^{(m)}}{\varepsilon_{\mathrm{OBJ}}^{(m)} + 2\varepsilon_{\mathrm{RO}}^{(m)}}, \tag{3.28}$$

where $\varepsilon_{\mathrm{OBJ}}^{(m)}$ is the scatterer's permittivity and $\varepsilon_{\mathrm{RO}}^{(m)}$ is that of the background. As a result, the ratio $\Gamma_{\mathrm{OUT}}^{(m)}(\mathbf{r}')/\Gamma_{\mathrm{CO}}^{(m)}$ can be expressed as

$$\frac{\Gamma_{\mathrm{OUT}}^{(m)}(\mathbf{r}')}{\Gamma_{\mathrm{CO}}^{(m)}} \approx \frac{\varepsilon_{\mathrm{CO}}^{(m)} + 2\varepsilon_{\mathrm{RO}}^{(m)}(\mathbf{r}')}{\varepsilon_{\mathrm{OUT}}^{(m)}(\mathbf{r}') + 2\varepsilon_{\mathrm{RO}}^{(m)}(\mathbf{r}')}, \tag{3.29}$$

where $\varepsilon_{\mathrm{CO}}^{(m)} \equiv \delta\varepsilon_{\mathrm{CO}}^{(m)} + \varepsilon_{\mathrm{RO}}^{(m)}$ is the permittivity of the small scatterer in the CO. Thus, the accuracy of the proposed method depends on the condition,

$$\varepsilon_{\mathrm{OUT}}^{(m)}(\mathbf{r}') \approx \varepsilon_{\mathrm{CO}}^{(m)} \tag{3.30}$$

or

$$\left|\varepsilon_{\mathrm{OUT}}^{(m)}(\mathbf{r}')\right|, \left|\varepsilon_{\mathrm{CO}}^{(m)}\right| < \left|\varepsilon_{\mathrm{RO}}^{(m)}\right|. \tag{3.31}$$

According to (3.30), the method is accurate if the CO permittivity is similar to that of the OUT. If (3.30) holds, the low-contrast requirements of (3.31), typical for the linear Born or the Rytov approximations [22], are not necessary. Lastly, the expression in (3.29) suggests a method of overcoming the limitation associated with the requirement in (3.30). The ratio found in (3.29) can be used in conjunction with

the forward model in (3.10) in case large differences are expected between $\varepsilon_{\mathrm{OUT}}^{(m)}(\mathbf{r}')$ and $\varepsilon_{\mathrm{CO}}^{(m)}$. If the ratio in (3.29) is much bigger than one, it should be included in the forward model.

Assuming that the estimation inaccuracy stems only from the approximation of $\Gamma_{\mathrm{OUT}}^{(m)}(\mathbf{r}')/\Gamma_{\mathrm{CO}}^{(m)} \approx 1$ (and not from multiple scattering effects), an acceptable estimation range for the OUT complex permittivity distribution can be obtained within a specified error level α, $0 \le \alpha \le 1$. Requiring that

$$\left| \frac{\Gamma_{\mathrm{OUT}}^{(m)}(\mathbf{r}')}{\Gamma_{\mathrm{CO}}^{(m)}} - 1 \right| \le \alpha \tag{3.32}$$

and employing (3.29) leads to

$$\frac{\left|\varepsilon_{\mathrm{CO}}^{(m)} + 2\varepsilon_{\mathrm{RO}}^{(m)}(\mathbf{r}')\right|}{1+\alpha} \le \left|\varepsilon_{\mathrm{OUT}}^{(m)}(\mathbf{r}') + 2\varepsilon_{\mathrm{RO}}^{(m)}(\mathbf{r}')\right| \le \frac{\left|\varepsilon_{\mathrm{CO}}^{(m)} + 2\varepsilon_{\mathrm{RO}}^{(m)}(\mathbf{r}')\right|}{1-\alpha} \tag{3.33}$$

The inequalities in (3.33) provide the range of values for $\varepsilon_{\mathrm{OUT}}^{(m)}(\mathbf{r}')$ within which (3.32) is satisfied.

Finally, several practical issues should be emphasized. The size of the small scatterer in the CO limits the resolution of the images, i.e., resolution much better than the CO size cannot be achieved. This is why it is critical to use a CO of the smallest possible size (yet sufficiently large for acceptable SNR of the calibration data) so that the reconstruction algorithm can achieve its best performance in terms of resolution. We note that, in near-field imaging, the resolution is strongly influenced by the variability of the near-zone incident field rather than the

wavelength. From that point of view, since the proposed approach utilizes experimentally acquired resolvent kernel, it does allow for the retrieval of near-zone scattering information as long as the CO size is sufficiently small. Also, limitations may arise from the implementation of coordinate translation, in which translational invariance is assumed; see Section 2.3.2 in Chapter 2. In practice, this forces our imaging approach to rely on: (i) homogeneous background medium, (ii) an imaged region well removed from the RO's edges, and (iii) a scanned region that is twice larger than the imaged region (in the planar raster-scanning).

3.6 SUMMARY OF IMAGE-FORMATION PROCEDURE

The image-formation procedure is summarized here for the case of a planar raster-scanning acquisition system (see Section 2.2.2 in Chapter 2). If the total number of acquired signals at each sampling location is N_s' at each sample frequency, the scanning system provides a total of $N_s = N_s' \times N_x \times N_y$ signals, where N_x and N_y are the sample numbers along x and y, respectively. This can be easily adjusted for other scanning schemes. There are two main procedural stages: the *system calibration* and the *OUT imaging*.

The system calibration consists of: (i) acquisition of the RO responses, (ii) acquisition of the CO responses, and (iii) the generation and storing of the CO power

maps. The CO measurements are carried out using coordinate translation as described in Section 2.3.2 of Chapter 2, with only one scan per range location.

The OUT imaging consists of: (i) acquiring the responses of the OUT, (ii) generation of the OUT power map, (iii) generation of the OUT permittivity map. The detailed steps of the procedure are summarized below.

A. System calibration

<u>Step 1</u> Acquire the baseline signals $S^{(m)}_{\mathrm{RO},\,n}$ (RO measurement).

<u>Step 2</u> Place the small scatter at the center $\mathbf{r}'_0$ of the desired $z' = const$ plane and acquire the signals $S^{(m)}_{\mathrm{CO},\,0,\,n}$ (CO measurement).

<u>Step 3</u> Obtain all CO signals $S^{(m)}_{\mathrm{CO},\,p,\,n}\left(\mathbf{r}_{uv}\right)$ for the $z' = const$ plane using the coordinate translation in (2.27).

<u>Step 4</u> Calculate the scattering CO responses $\Delta S^{(m)}_{\mathrm{CO},\,p,n}\left(\mathbf{r}_{uv}\right)$ using (2.20).

<u>Step 5</u> Obtain the CO power maps $M^{(m)}_{\mathrm{CO},\,q}(\mathbf{r}'_p)$, $q = 1, 2, \ldots, N_{\mathrm{v}}$, using (3.17) implemented as

$$M^{(m)}_{\mathrm{CO},q}(\mathbf{r}'_p) = \sum_{u=1}^{N_x}\sum_{v=1}^{N_y}\sum_{n=1}^{N'_{\mathrm{S}}} \Delta S^{(m)}_{\mathrm{CO},q,n}(\mathbf{r}_{uv}) \cdot \left[\Delta S^{(m)}_{\mathrm{CO},\,p,n}(\mathbf{r}_{uv})\right]^{*}. \tag{3.34}$$

B. OUT image *generation*

<u>Step 6</u> Acquire the signals $S^{(m)}_{\mathrm{OUT},\,n}\left(\mathbf{r}_{uv}\right)$ (OUT measurement).

<u>Step 7</u> Calculate the scattering OUT responses $\Delta S^{(m)}_{\mathrm{OUT},\,n}\left(\mathbf{r}_{uv}\right)$ using

$$\Delta S_{\mathrm{OUT},n}^{(m)}\left(\mathbf{r}_{uv}\right)=S_{\mathrm{OUT},n}^{(m)}\left(\mathbf{r}_{uv}\right)-S_{\mathrm{RO},n}^{(m)}\left(\mathbf{r}_{uv}\right). \tag{3.35}$$

<u>Step 8</u> Obtain the OUT power map $M_{\mathrm{OUT}}^{(m)}(r_p')$ using (3.14) implemented as

$$M_{\mathrm{OUT}}^{(m)}(\mathbf{r}_p')=\sum_{u=1}^{N_x}\sum_{v=1}^{N_y}\sum_{n=1}^{N_s'}\Delta S_{\mathrm{OUT},n}^{(m)}(\mathbf{r}_{uv})\cdot\left[\Delta S_{\mathrm{CO},p,n}^{(m)}(\mathbf{r}_{uv})\right]^{*}. \tag{3.36}$$

<u>Step 9</u> Calculate the initial vectors $\boldsymbol{\tau}_0^{(m)}$ using (3.25).

<u>Step 10</u> Solve (3.19) with $\boldsymbol{\tau}_0^{(m)}$ to obtain $\boldsymbol{\tau}_*^{(m)}$.

<u>Step 11</u> Obtain $\varepsilon_{\mathrm{OUT}}^{(m)}(\mathbf{r}_p')$ using (3.26) with $\boldsymbol{\tau}_*^{(m)}$, $\varepsilon_{\mathrm{RO}}^{(m)}(\mathbf{r}_p')$ and $\delta\varepsilon_{\mathrm{CO}}^{(m)}$.

C. Multi-frequency combination (used with wideband data)

The multi-frequency strategy is recommended when thousands of frequency samples may need to be processed. First, the power maps of the OUT and the CO at all N_{f} frequencies are combined via

$$\bar{M}_{\mathrm{OBJ}}(r_p')=\frac{1}{N_{\mathrm{f}}}\sum_{m=1}^{N_{\mathrm{f}}}\frac{M_{\mathrm{OBJ}}^{(m)}(\mathbf{r}_p')}{\eta^{(m)}},\ \mathrm{OBJ}\equiv\mathrm{OUT,\ CO}. \tag{3.37}$$

Here, $\eta^{(m)}$ is the maximum magnitude value of the CO power maps at the m-th frequency:

$$\eta^{(m)}=\max\left(\left\{\left|M_{\mathrm{CO},q}^{(m)}(\mathbf{r}_p')\right|:p=1,2,\ldots,N_{\mathrm{v}};q=1,2,\ldots,N_{\mathrm{v}}\right\}\right). \tag{3.38}$$

The combined CO and OUT maps obtained through (3.37) are next used to fill the matrix $\boldsymbol{M}$ and the vector $\boldsymbol{m}$ in (3.19), respectively. Following Step 9 to Step 11 from the procedure at a single frequency, (3.19) is solved to obtain $\varepsilon_{\mathrm{OUT}}(\mathbf{r}_p')$.

We note that the multi-frequency combination can be done via simple averaging of the permittivity distributions obtained at all single-frequency solutions. However, the method described above produces better results. This is because the imaging resolution of the direct-averaging approach is badly influenced by the low-frequency solutions. This is not the case in the proposed multi-frequency scheme, which reduces the impact of the low-resolution images at an earlier stage by combining the power maps. Also, notice that the LS solver is only called once with the multi-frequency combination scheme.

3.7 RECONSTRUCTION OF AN F-SHAPED DIELECTRIC BAR USING SIMULATION DATA

A planar raster-scanning acquisition system is emulated with a full-wave electromagnetic numerical solver based on the method of moments [23]. We attempt to image an F-shaped dielectric bar in air. In the simulations of all the measurements, a pair of half-wavelength dipole antennas is used as the Rx/Tx antennas. The sampled frequencies are from 3 GHz to 16 GHz with an interval of 1 GHz, i.e., N_f = 14. At each frequency, the length of the dipole is automatically adjusted to half of the wavelength for a good impedance match. The simulated responses include both the transmission and the reflection coefficients for a total of 4 *S*-parameters.

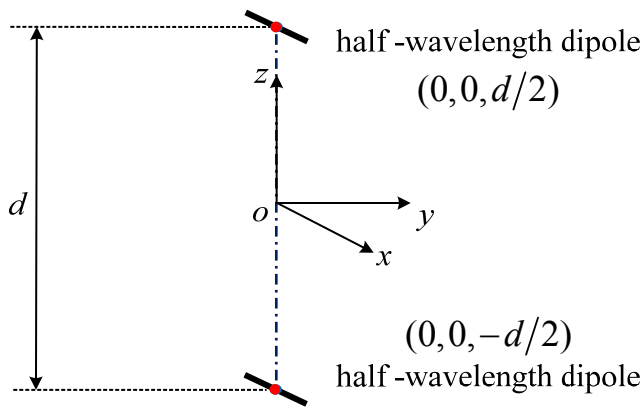

Fig. 3.1 Configuration of the simulation setup for the RO measurement. The RO is air.

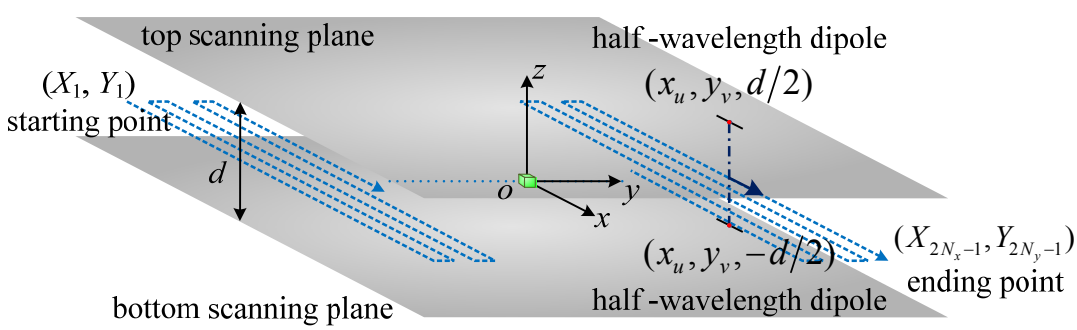

Fig. 3.2 Configuration of the simulation setup for the CO measurement. The small scatterer embedded in the CO is a dielectric cube with known property contrast $\delta\varepsilon_{\mathrm{CO}}^{(m)}$.

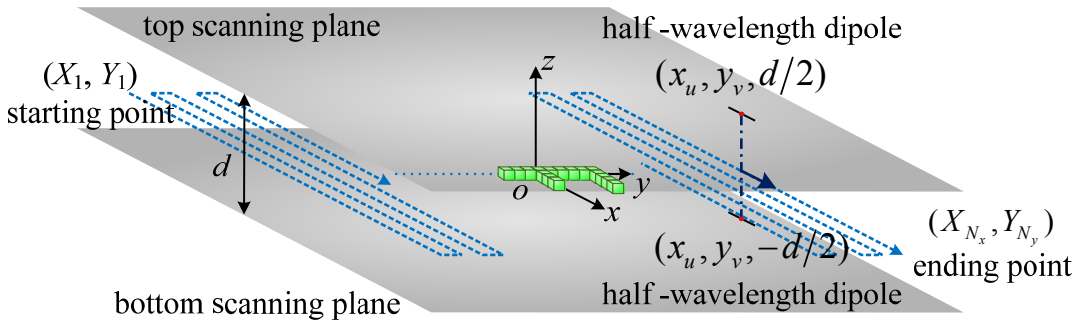

Fig. 3.3 Configuration of the simulation setup for the OUT measurement. The OUT is an F-shaped dielectric bar placed at the middle layer.

Fig. 3.1 shows the RO measurement emulated in simulations, where the RO is set to be air, i.e., $\varepsilon_{\mathrm{RO}}^{(m)} = \varepsilon_{\mathrm{RO}}^{\prime(m)} - \mathrm{i}\varepsilon_{\mathrm{RO}}^{\prime\prime(m)} = 1.0 - \mathrm{i}0.0$. The half-wavelength dipoles are oriented along x, which are placed at (0, 0, d/2) and (0, 0, −d/2), respectively. Here, d = 5 cm is the distance between the top and bottom scanning planes. Since the background medium is homogeneous, in the absence of numerical errors, the S-parameters should be the same at all the sampled positions. Thus, at each frequency, only one simulation of the RO measurement is performed.

In the simulation of the CO measurement, as shown in Fig. 3.2, a small dielectric cube of 1 cm^3 is placed at the origin (the center of the z = 0 plane). The small scatterer has a property contrast of 0.1 in the real permittivity only, i.e., $\delta\varepsilon_{\mathrm{CO}}^{(m)} = 0.1 - \mathrm{i}0.0$, which is set to be frequency independent. For another z' = *const.* plane, the dielectric cube is placed in the center of this plane and the CO data acquisition is repeated.

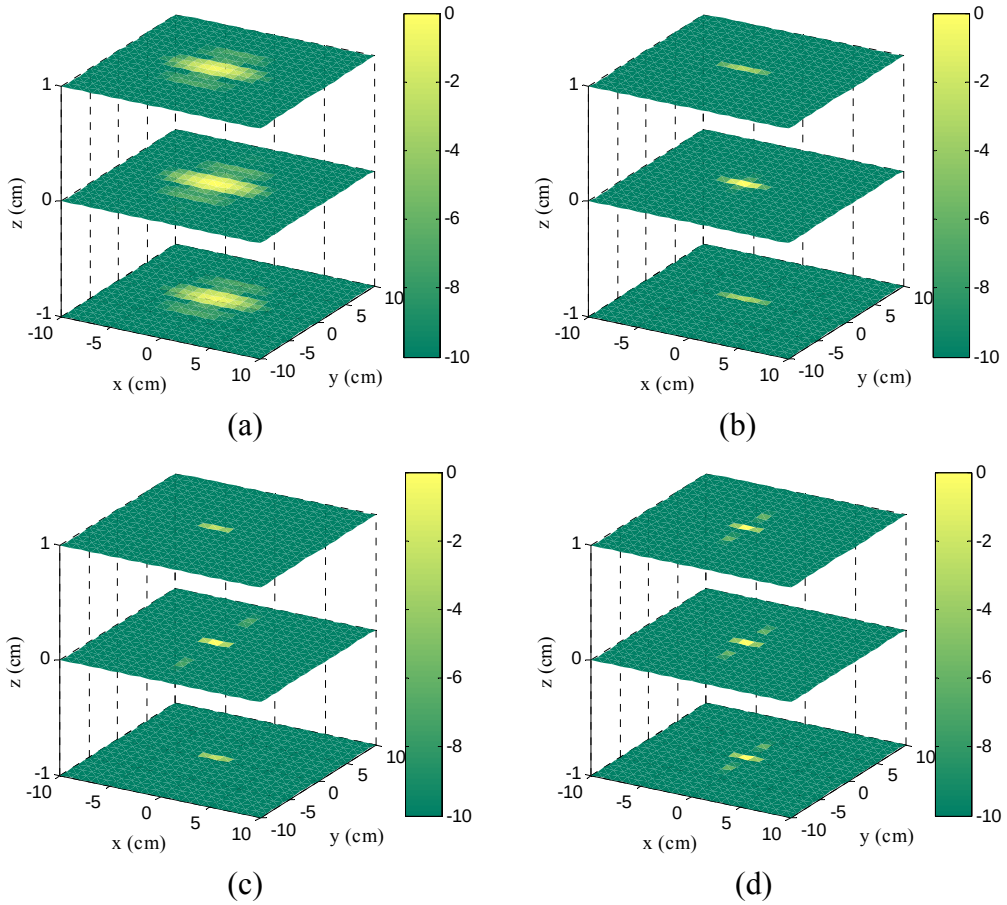

Fig. 3.4 Normalized magnitude plots (in dB) of the power maps of the CO in the simulation example at: (a) 3 GHz, (b) 7 GHz, (c) 11 GHz, and (d) 15 GHz. The small scatterer is assumed at (0, 0, 0), i.e., at the center of the middle layer.

To simulate the OUT measurement, as shown in Fig. 3.3, an F-shaped dielectric bar is placed in the $z = 0$ plane. It consists of 16 dielectric cubes. Each cube has the same size of 1 cm^3 and has a property contrast of 0.2 in the real permittivity

only, i.e., $\varepsilon_{\mathrm{OUT}}^{(m)} = \varepsilon_{\mathrm{OUT}}^{\prime(m)} - \mathrm{i}\varepsilon_{\mathrm{OUT}}^{\prime\prime(m)} = 1.2 - \mathrm{i}0.0$. The OUT contrast is set to be frequency independent as well.

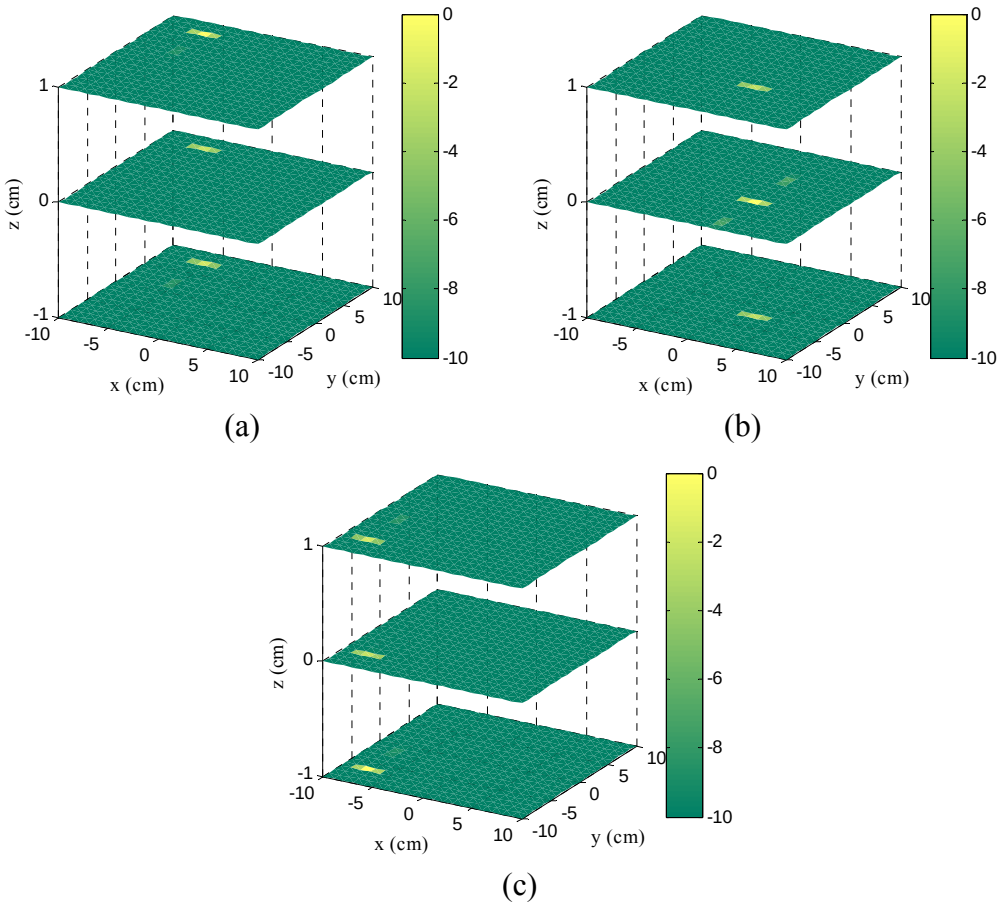

Fig. 3.5 Normalized magnitude plots (in dB) of the power maps of the CO in the simulation example at 11 GHz. The small scatterer is assumed at: (a) (−6, 8, 1) cm, (b) (4, −4, 0) cm, and (c) (−8, −8, −1) cm.

The scanning aperture in the OUT acquisition is 20 × 20 cm^2 with N_x = 21 and N_y = 21, respectively. In order to perform the coordinate translation, the scanning

aperture is enlarged to 40 × 40 cm^2 in the CO acquisition providing $(2N_x - 1)$ and $(2N_y - 1)$ sample points along x and y, respectively. The sampling step size along x and y is 1 cm. The imaged volume is divided evenly into 5 layers along the z axis. Each layer is 1 cm thick. The F-shaped dielectric bar resides in the middle layer.

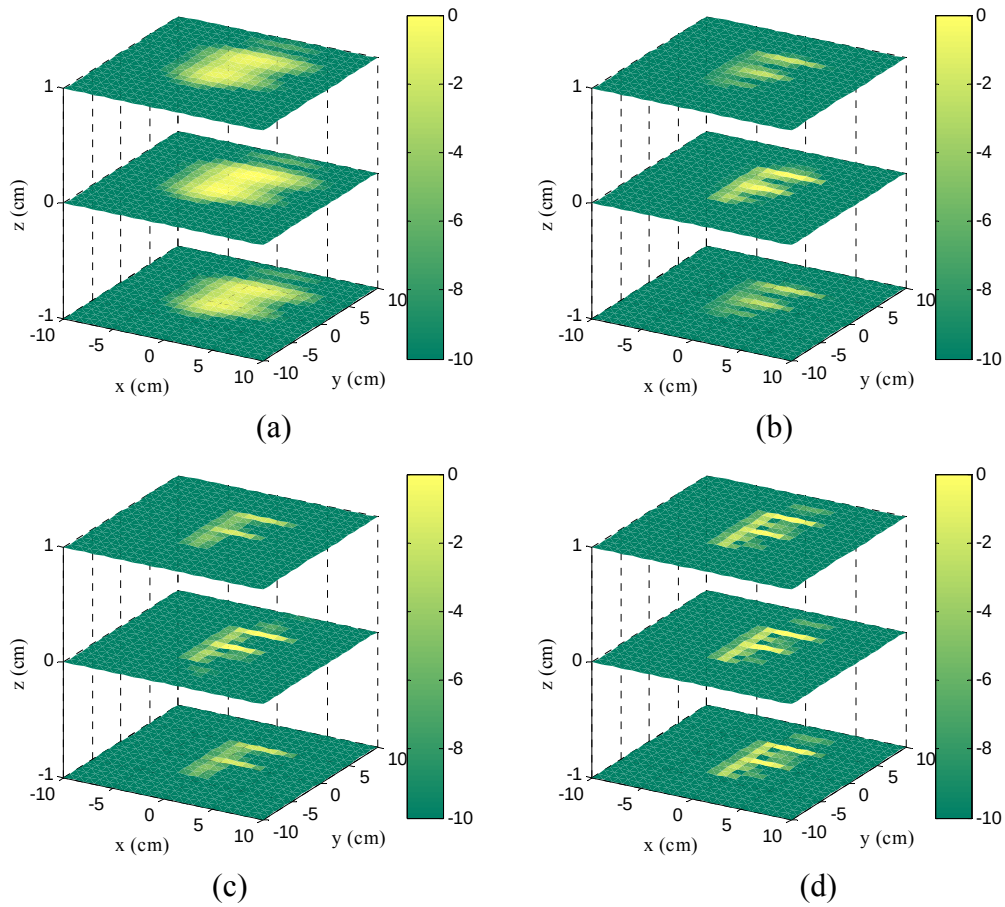

Fig. 3.6 Normalized magnitude plots (in dB) of the power maps of the OUT in the simulation example at: (a) 3 GHz, (b) 7 GHz, (c) 11 GHz, and (d) 15 GHz. The F-shaped dielectric bar is placed in the middle layer

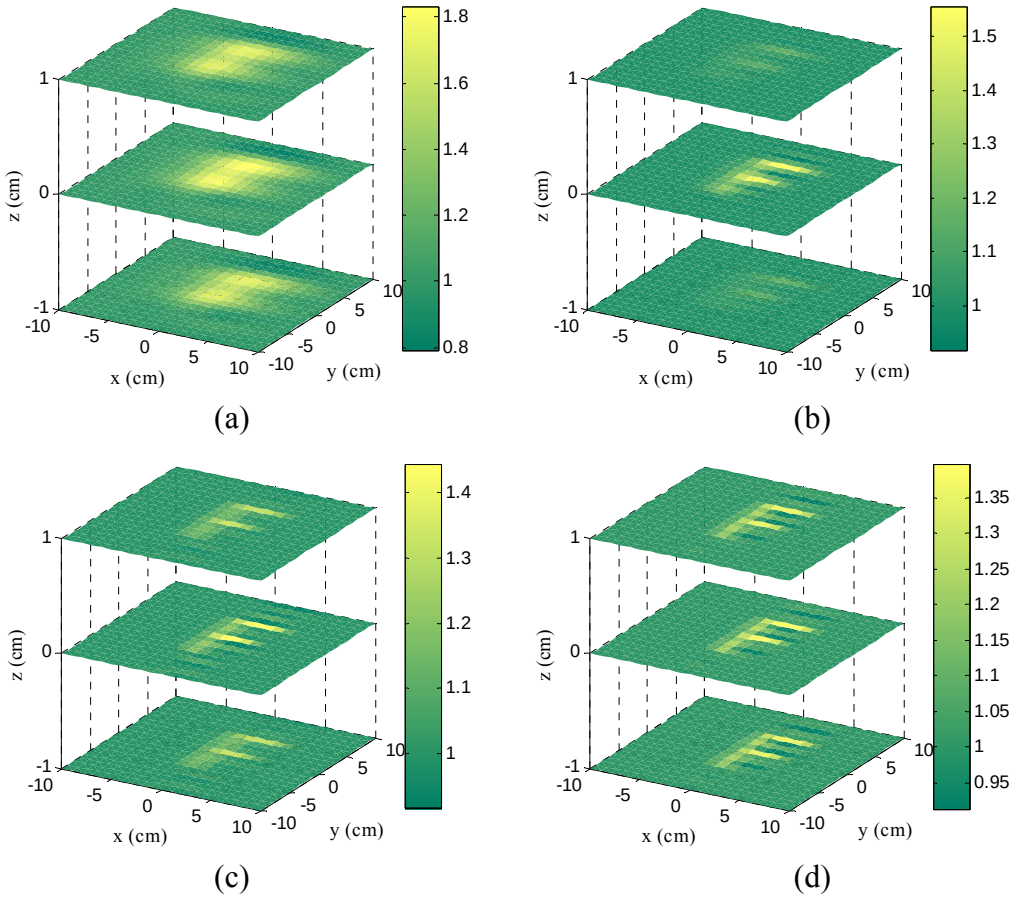

Fig. 3.7 Initial guess for the real permittivity distribution (ε') of the OUT in the simulation example at: (a) 3 GHz, (b) 7 GHz, (c) 11 GHz, and (d) 15 GHz. The F-shaped dielectric bar is placed in the middle layer. The actual values of the background and the F-shaped object are 1.0 and 1.2, respectively.

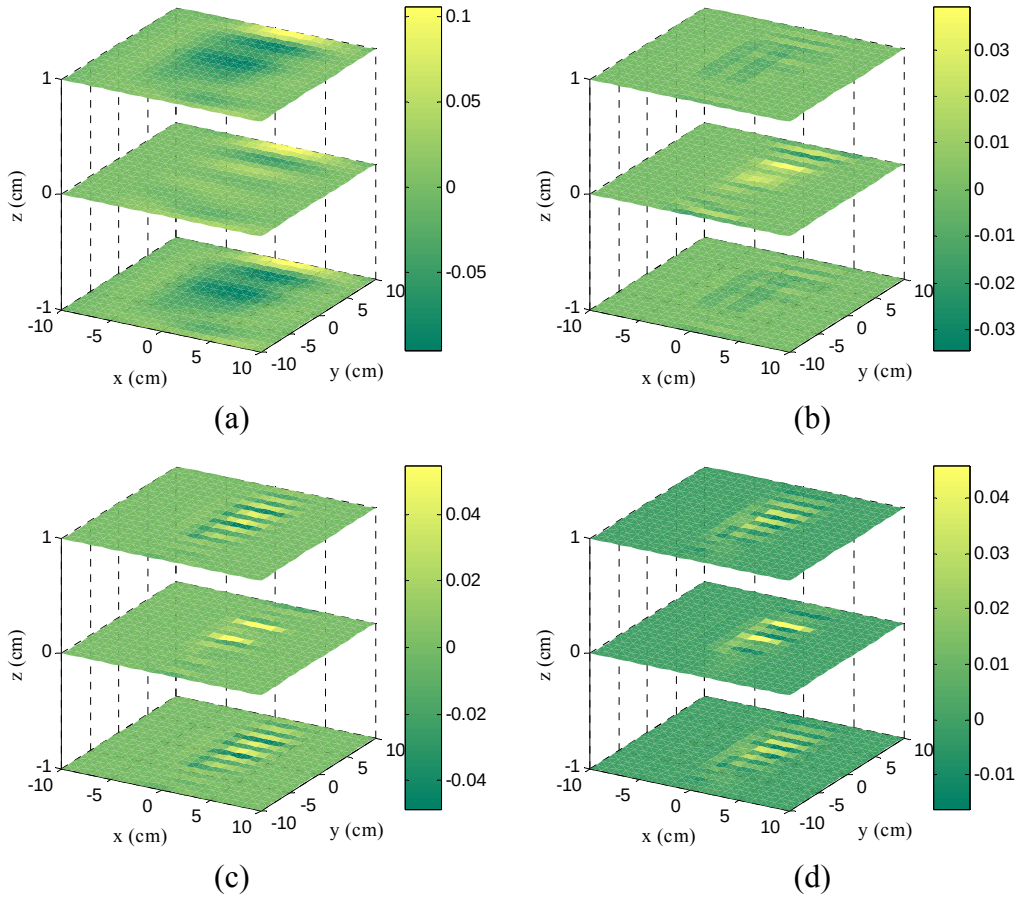

Fig. 3.8 Initial guess for the imaginary permittivity distribution (ε'') of the OUT in the simulation example at: (a) 3 GHz, (b) 7 GHz, (c) 11 GHz, and (d) 15 GHz. The actual value is 0.0 in both the background and the F-shaped object.

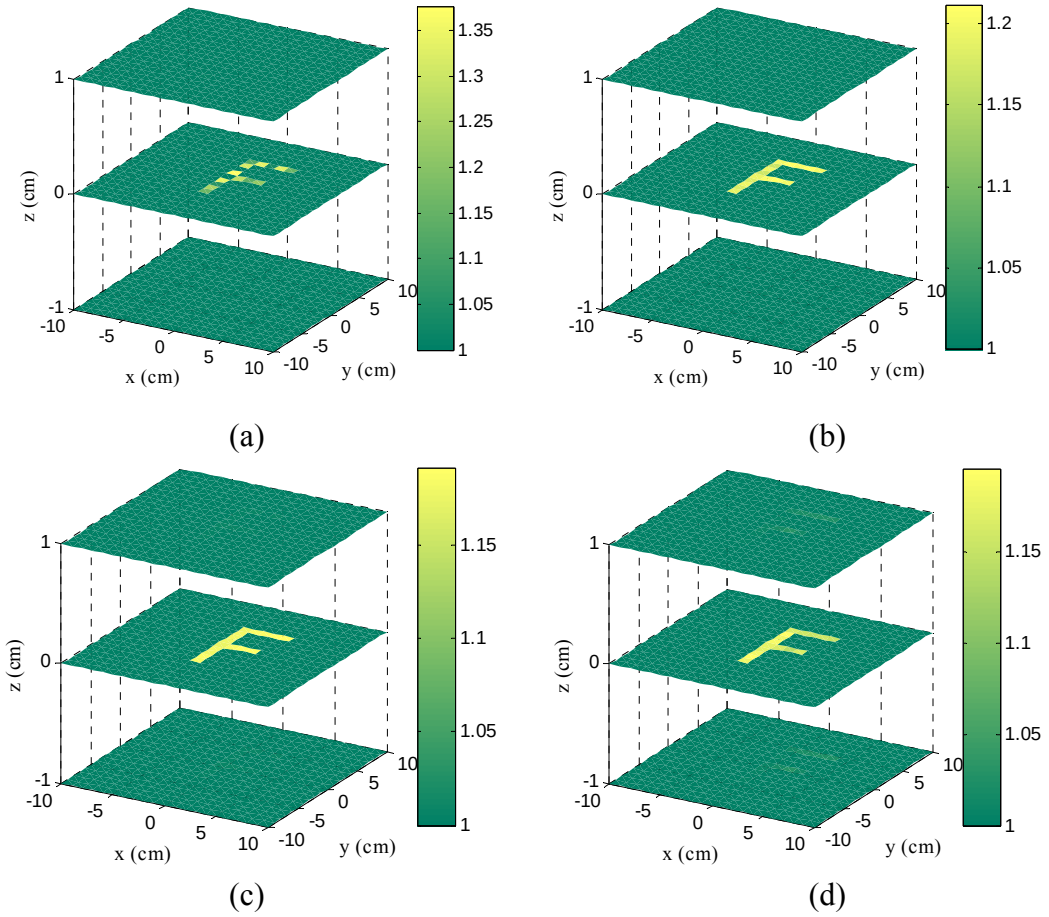

Fig. 3.9 LS solutions for the real permittivity distribution (ε') of the OUT in the simulation example at: (a) 3 GHz, (b) 7 GHz, (c) 11 GHz, and (d) 15 GHz. The actual values of the background and the F-shaped object are 1.0 – i0 and 1.2 – i0, respectively.

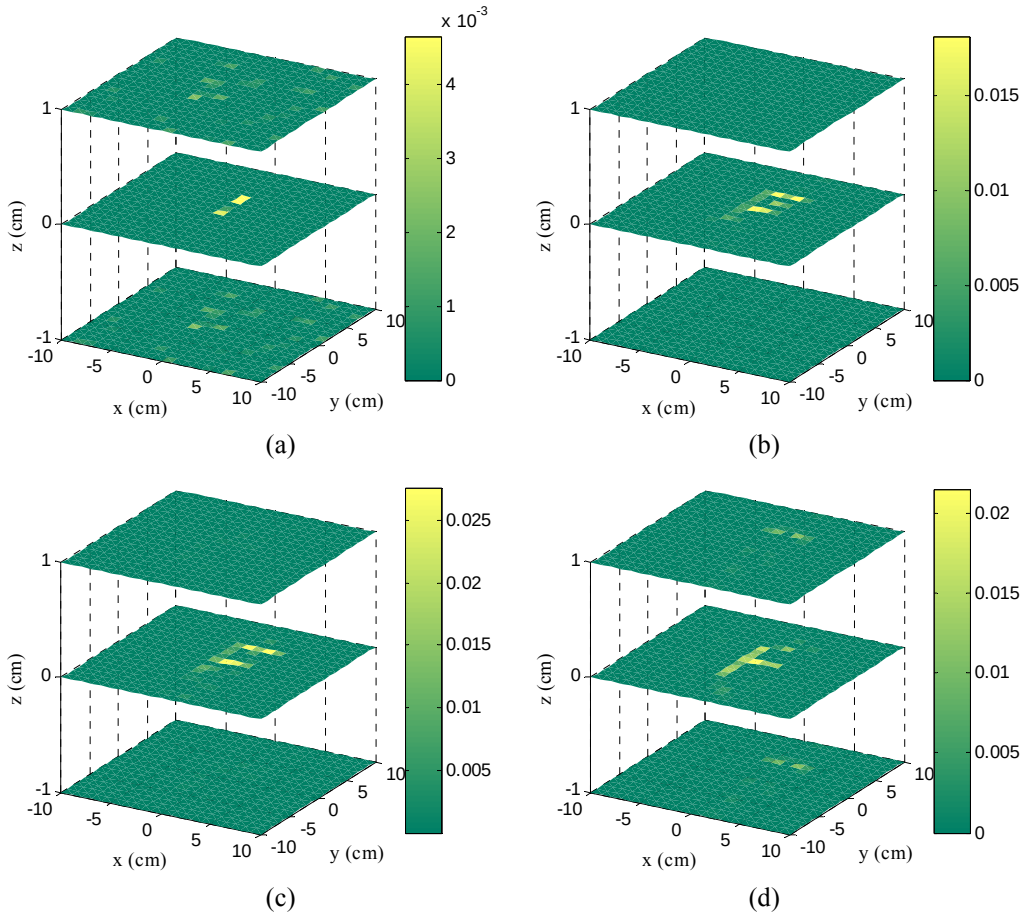

Fig. 3.10 LS solutions for the imaginary permittivity distribution (ε'') of the OUT in the simulation example at: (a) 3 GHz, (b) 7 GHz, (c) 11 GHz, and (d) 15 GHz. The actual value is 0.0 in both the background and the F-shaped object.

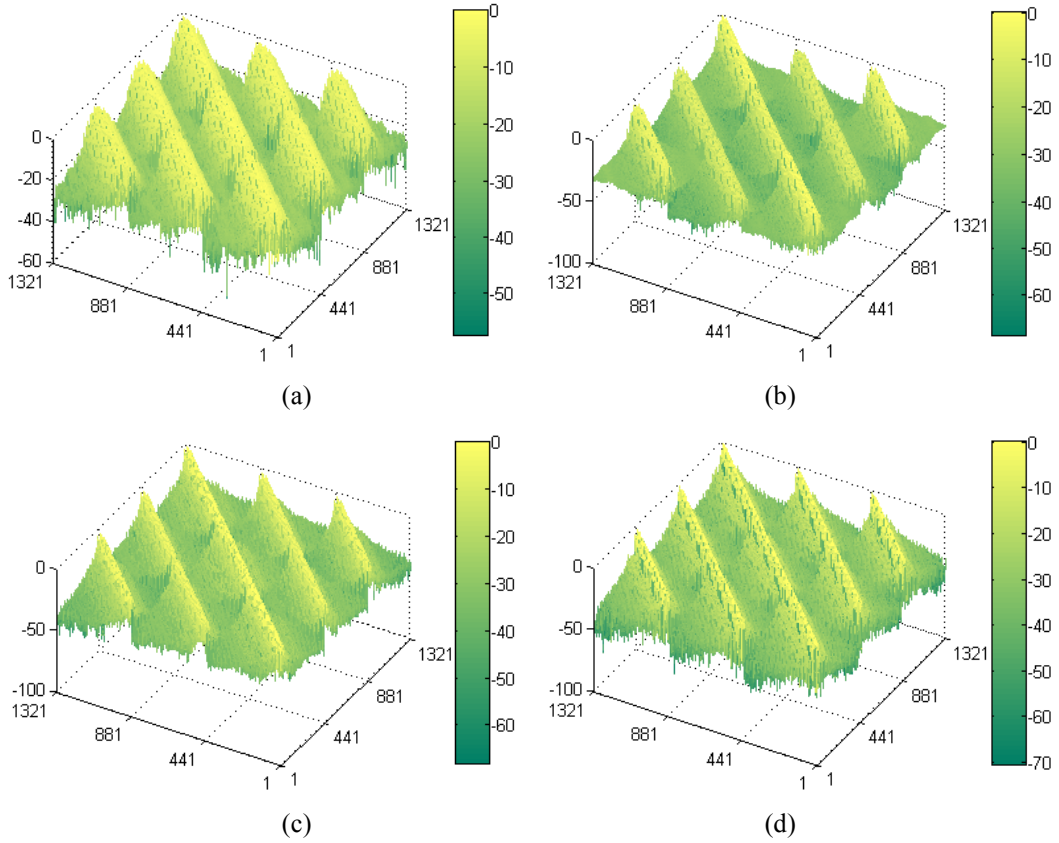

Fig. 3.11 Normalized magnitude plots (in dB) of the system matrix $\boldsymbol{M}^{(m)}$ (3.20) of the LS problem (3.19) for the simulation example at: (a) 3 GHz, (b) 7 GHz, (c) 11 GHz, and (d) 15 GHz.

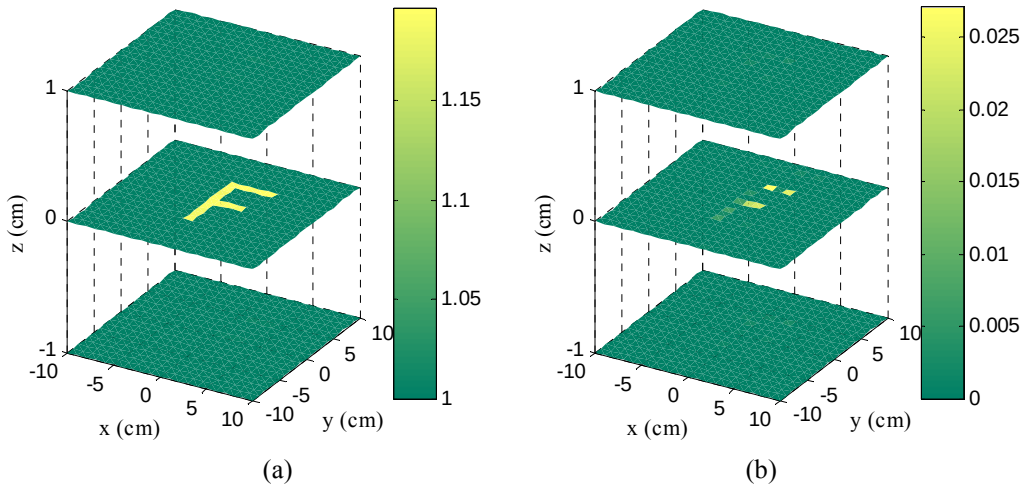

Fig. 3.12 LS solutions for complex permittivity distribution of the OUT in the simulation example using multi-frequency combination: (a) real permittivity (ε'), and (b) imaginary permittivity (ε'').

Using the *S*-parameters acquired with the CO simulations, the database of CO power maps is built using (3.17); see also Step 5 in the system calibration stage described in Section 3.6. These complex-valued maps represent the system PSF and they are crucial for the subsequent property estimation obtained by solving (3.19).

Fig. 3.4 shows the normalized magnitude plots (in dB) of the power maps of the CO at 3 GHz, 7 GHz, 11 GHz and 15 GHz. The small scatterer is placed at the center (0, 0, 0) cm, where the peak values are clearly observed. It can be also observed that the map approaches the ideal delta function distribution as the frequency increases. This indicates that the spatial resolution is better at higher

frequencies, which is expected. Meanwhile, due to the source polarization (the dipoles are x-polarized), steeper slopes can be observed along the y direction. The improved spatial resolution in the y direction is consistent with the fact that the dipoles' patterns in this direction are broader, which is another prerequisite for better spatial resolution. On the other hand, there are more artifacts along the y direction. This is due to the finite size of the scanned surface which supports an angle (with respect to the center of the imaged volume) that is narrower than the antenna beam in the $x = 0$ plane.

Fig. 3.5 shows the normalized magnitude plots (in dB) of the power maps of the CO at 11 GHz only, when the small scatterer is assumed placed at (−6, 8, 1) cm, (4, −4, 0) cm, and (−8, −8, −1) cm. It is observed that the map peak moves in correspondence with the scatterer location, which is expected since the CO responses in all these off-center scatterer locations are obtained via coordinate translation from the CO responses with the scatterer being at the center.

Fig. 3.6 shows the normalized magnitude plots (in dB) of the power maps of the OUT at 3 GHz, 7 GHz, 11 GHz, and 15 GHz. These images are only qualitative. It is observed that the cross-range resolution (along x and y) improves as the frequency increases, which is expected. Due to the different beamwidths in the x-z and y-z antenna radiation patterns, the resolution performance along x and y is somewhat different; i.e., the branches of the F-shape along x have somewhat sharper contrast compared with that along y. It is also observed that the dependence of the

range resolution on frequency is not significant. This is expected as in planar scanning it is the bandwidth which impacts the range resolution.

The property distribution of the OUT is first estimated through the initial guess $\boldsymbol{\tau}_0^{(m)}$ under the assumption that the CO maps are ideal delta functions (see Step 9 in Section 3.6B). Fig. 3.7 shows the initial guess for the real permittivity distribution (ε') of the OUT at 3 GHz, 7 GHz, 11 GHz and 15 GHz. Fig. 3.8 shows the initial guess for the imaginary permittivity distribution (ε'') at the same sample frequencies. We recall that the F-shaped bar in the OUT has a complex relative permittivity of $1.2 + \mathrm{i}0.0$ with a property contrast in real permittivity only with respect to the RO (air). This difference between the real and the imaginary permittivity distributions in the OUT is already well captured in the initial guess shown in Fig. 3.7 and Fig. 3.8. However, the initial permittivity estimate has substantial errors and is only as good as to serve as an adequate starting point toward the solution of the LS problem (3.19).

Fig. 3.9 shows the LS solutions for the real permittivity distribution (ε') of the OUT at 3 GHz, 7 GHz, 11 GHz and 15 GHz, while Fig. 3.10 shows the respective imaginary permittivity distribution (ε''). The LS solutions use the LS solver *lsqlin* of MATLAB [24] with physical constraints on the real and imaginary permittivities: $\varepsilon' \geq 1$ and $\varepsilon'' \geq 0$. Compared with the initial guess (see Fig. 3.7 and Fig. 3.8), the estimation accuracy has been improved dramatically.

Fig. 3.11 shows the normalized magnitude plots (in dB) of the system matrix $\boldsymbol{M}^{(m)}$ (3.20) of the LS problem (3.19) for the simulation example at 3 GHz, 7 GHz, 11 GHz and 15 GHz. As discussed in Section 3.4 of Chapter 3, it is observed that the system matrix $\boldsymbol{M}^{(m)}$ is a predominantly block-diagonal matrix, the diagonal elements of which become more and more dominant as the frequency increases.

Fig. 3.12 shows the results obtained with the multi-frequency combination in Section 3.6C. It is worth noting that these results are much better than the simple averaging of the complex-permittivity images obtained at all frequencies.

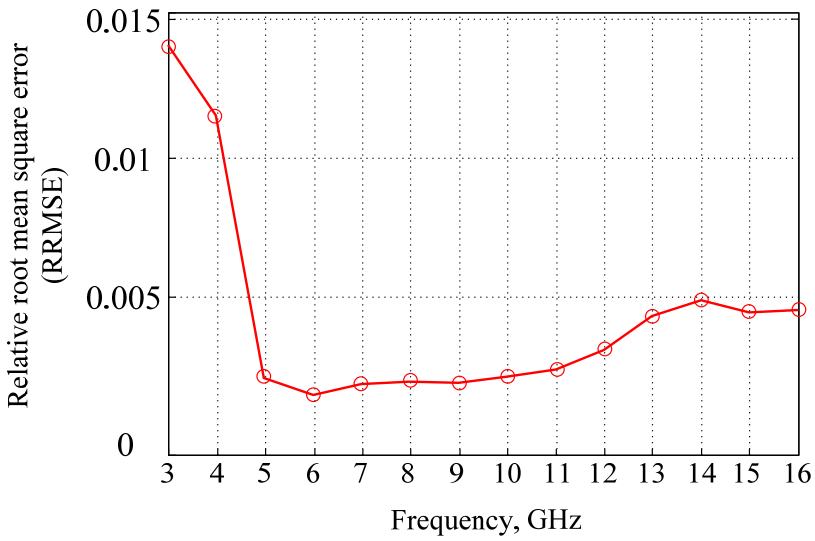

Fig. 3.13 The relative root mean square error (RRMSE) of the LS solution for the complex permittivity distribution of the OUT using simulation data.

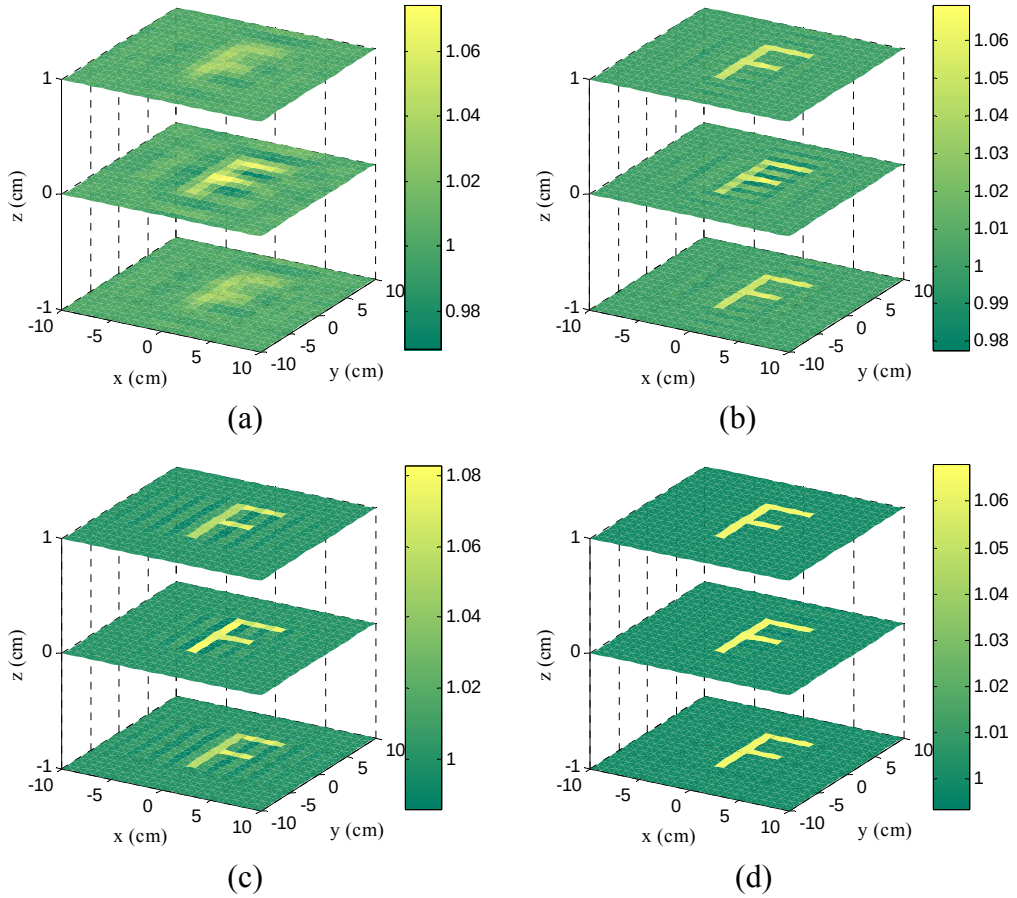

Fig. 3.14 Solutions of linear Born inversion using the Moore-Penrose pseudoinverse for the real-permittivity distribution (ε') of the OUT in the simulation example at: (a) 3 GHz, (b) 7 GHz, (c) 11 GHz, and (d) 15 GHz. The actual values of the background and the F-shaped object are 1.0 and 1.2, respectively.

The RRMSE defined in (3.27) for the LS solution is given in Fig. 3.13. It is worth mentioning that the raw simulation data is not purely noiseless; it contains numerical errors at a very low level. The average mesh convergence error for the *S*-parameters in the simulations is around 0.02 (added uncertainty of ±0.01 for all reflection and transmission coefficients) over the entire frequency band. It is evident that the RRMSE of the LS solutions over the whole frequency band is well below 0.015 and orders of magnitude better than the initial guess. Generally, the accuracy improves as the frequency increases

The choice of the solver and the initial point are critical in dealing with the nonuniqueness of the solution. As an example, Fig. 3.14 shows the real permittivity solutions of the direct (or linear) Born inversion using the Moore-Penrose pseudoinverse of the equations defined by (3.13). Note that the pseudoinverse solver (the MATLAB function *pinv*) allows neither for an initial point setting nor for constraints. The F-shaped target is detected well along the cross-range but not along the range.

The pseudoinverse solution can be applied to the equations defined by (3.19) as well. The result is comparable to the one shown in Fig. 3.14 (not shown here for brevity) and much worse than the iterative LS solution where we employed the initial guess (3.25) along with physically based constraints on the complex permittivity values.

Finally, we note that the direct solution of either (3.13) or (3.19) with multi-frequency wideband data is impractical when the number of frequency samples is on the order of hundreds or thousands. In this case, the intermediate step of constructing multi-frequency power maps is critical as it provides computational speed and an adequate initial point for the linear LS solution.

3.8 CONCLUSIONS

A fast imaging method is proposed, which achieves quantitative reconstruction through the direct inversion of the scattering problem in real space (as opposed to Fourier or k space). The method does not require analytical or numerical approximations of the forward model since the acquisition system is fully characterized through the calibration measurements of known objects: the RO and the CO.

First, the baseline measurement is that of the RO, i.e., the assumed known background medium together with the acquisition apparatus. It is essential in estimating the incident field and, therefore, in extracting the scattered signal component from the total signal. The main goal of the RO measurement is to describe properly all the features of the particular acquisition system (e.g., transmitting and receiving antennas, the fixtures and shielding) rather than possible complexities of the OUT. The OUT features are the subject of the reconstruction, not

the system calibration. The construction of a proper physical RO depends on the expected averaged OUT permittivity distribution. The closer the RO properties are to those of the OUT, the more successful the reconstruction would be as discussed in Section 3.5. If no additional prior knowledge is available about the expected OUTs, the RO is fabricated as a homogeneous object, which is also done here.

Second, the CO measurement takes the above standard calibration procedure only one step further by employing a small known object in the already available RO. As in the RO measurement, the CO measurement aims at describing properly the PSFs of the particular sensors rather than attempting to mimic the OUT. The acquired CO signals are critically important for the proposed quantitative inversion as they comprise the functional basis for quantifying the OUT responses.

The direct inversion without the need for Fourier transforms enables real-time reconstruction. Acquiring the system's resolvent kernel experimentally, instead of using analytical or simulation models, improves drastically the image quality, especially in the case of near-field imaging where these models become inadequate.

The proposed method is not subject to the typical limitation associated with the linear Born or the Rytov approximations. However, its accuracy is shown to improve if the dielectric properties of the small known target in the calibration object are similar to those in the OUT. In addition, the method does not account for multiple scattering. These limitations cannot be ignored in the imaging of heterogeneous objects with wide contrast variations. In such cases, the method can

provide a good initial estimate of the object's permittivity distribution toward subsequent refinement through a nonlinear iterative solution.

REFERENCES

[1] Y. M. Wang and W. C. Chew, "An iterative solution of the two-dimensional electromagnetic inverse scattering problem," *Int. J. Imag. Syst. Technol.*, vol. 1, no. 1, pp. 100−108, Feb. 1989.

[2] W. C. Chew and Y. M. Wang, "Reconstruction of two-dimensional permittivity distribution using the distorted Born iterative method," *IEEE Trans. Med. Imag.*, vol. 9, no. 2, pp. 218−225, June 1990.

[3] K. D. Paulsen, P. M. Meaney, and L. C. Gilman (Eds.), *Alternative Breast Imaging: Four Model Based Approaches*, Springer, 2005.

[4] T. G. Savelyev and A. G. Yarovoy, "Fast image by 3-D deconvolution in short-range UWB radar for concealed weapon detection," *The 9th European Radar Conf. (EuRAD 2012)*, pp. 26−29, Oct. 2012.

[5] T. Sakamoto, T. G. Savelyev, P. Aubry, and A. G. Yarovoy, "Fast range point migration method for weapon detection using ultra-wideband radar," *The 9th European Radar Conf. (EuRAD 2012)*, pp. 230−233, Oct. 2012.

[6] T. M. Habashy, R. W. Groom, and B. R. Spies, "Beyond the Born and Rytov

approximations: a nonlinear approach to electromagnetic scattering," *J. Geophys. Res.*, vol. 98, no. B2, pp. 1759−1775, Feb. 1993.

[7] M. S. Zhdanov and S. Fang, "Quasi-linear approximation in 3-D electromagnetic modeling," *Geophysics*, vol. 61, no. 3, pp. 646−645, May 1996.

[8] M. S. Zhdanov and Sheng Fang, "Three-dimensional quasi-linear electromagnetic inversion," *Radio Sci.*, vol. 31, no. 4, pp. 741−754, July 1996.

[9] M. Zhdanov and G. Hursan, "3D electromagnetic inversion based on quasi-analytical approximation," *Inverse Problems*, vol. 16, pp. 1297−1322, 2000.

[10] D. M. Sheen, D. L. McMakin, and T. E. Hall, "Three-dimensional millimeter-wave imaging for concealed weapon detection," *IEEE Trans. Microw. Theory Tech.*, vol. 49, no. 9, pp. 1581−1592, Sept. 2001.

[11] M. Elsdon, D. Smith, M. Leach, and S. J. Foti, "Experimental investigation of breast tumor imaging using indirect microwave holography," *Microw. Opt. Technol. Letters,* vol. 48, no. 3, pp. 480−482, Mar. 2006.

[12] M. Ravan, R. K. Amineh, and N. K. Nikolova, "Two-dimensional near-field microwave holography," *Inverse Problems*, vol. 26, 055011, 2010.

[13] R. K. Amineh, M. Ravan, N. K. Nikolova, and A. Khalatpour, "Three-dimensional near-field microwave holography using reflected and transmitted signals," *IEEE Trans. Antennas Propag.*, vol. 59, no. 12, pp. 4777−4789,

Dec. 2011.

[14] E. C. Fear, X. Li, S. C. Hagness, and M. A., "Confocal microwave imaging for breast cancer detection: localization of tumors in three dimensions," *IEEE Trans. Biomed. Eng.*, vol. 49, no. 8, pp. 812−822, Aug. 2002.

[15] H. B. Lim, N. T. T. Nhung, P. E. Li, and N. D. Thang, "Confocal microwave imaging for breast cancer: delay-multiply-and-sum image reconstruction algorithm," *IEEE Trans. Biomed. Eng.*, vol. 55, no. 6, pp. 1697−1704, June 2008.

[16] M. Klemm, I. J. Craddock, J. A. Leendertz, A. Preece, and R. Benjamin, "Radar-based breast cancer detection using a hemispherical antenna aray—experimental results," *IEEE Trans. Antennas Propag.*, vol. 57, no.6, pp. 1692−1704, June 2009.

[17] L. Liu, A. Trehan, and N. K. Nikolova, "Near-field detection at microwave frequencies based on self-adjoint response sensitivity analysis," *Inverse Problems*, vol. 26, 105001, 2010.

[18] Y. Zhang, S. Tu, R. K. Amineh and N. K. Nikolova, "Resolution and robustness to noise of the sensitivity-based method for microwave imaging with data acquired on cylindrical surfaces," *Inverse Problems*, vol. 28, 115006, 2012.

[19] P. Kosmas and C. M. Rappaport, "Time reversal with the FDTD method for microwave breast cancer detection," *IEEE Trans. Microw. Theory Tech.*, vol.

53, no. 7, pp. 2317−2323, July 2005.

[20] P. Kosmas and C. M. Rappaport, "FDTD-based time reversal for microwave breast cancer detection-localization in three dimensions," *IEEE Trans. Microw. Theory Tech.*, vol. 54, no. 4, pp. 1921−1927, Apr. 2006.

[21] A. J. Devaney, *Mathematical Foundations of Imaging, Tomography and Wavefield Inversion*, Cambridge UK: Cambridge University Press, 2012.

[22] W. C. Chew, *Waves and Fields in Inhomogeneous Media*, New York: IEEE Press, 1995.

[23] FEKO suite 6.0 EM Software & System, Inc. USA, www.feko.info

[24] The MathWorks, MATLAB. Natick, MA, USA, Feb. 2010, [Online] http://www.mathworks.com/products/matlab

Chapter 4

NOISE ANALYSIS OF FAST QUANTITATIVE MICROWAVE IMAGING

4.1 INTRODUCTION

The data acquired using a practical imaging system carry noise which has a detrimental effect on the image quality [1]-[8]. This is especially true in the microwave imaging of tissue where the significant attenuation leads to vary weak signals. For an imaging technique, noise analysis is always necessary in order to determine its limitations associated with the noise levels.

The noise and uncertainty in an imaging system are due to both the systematic and random (stochastic) errors. Some systematic errors are easy to model and correct. For instance, the calibration of a VNA can be done via measurements with standard loads, which allows to effectively de-embed the systematic instrument errors from the measured result. On the other hand, some errors due to the sensor antennas and the mechanical scanning remain difficult to characterize [4]. Random errors are unavoidable for any system and they are caused by various factors. For instance, a system would have intrinsic random errors caused by the internal

electronic noise, the positioning mechanism, the wire and cable connections, etc. Also, external factors such as temperature variations and electromagnetic interference can introduce random noise.

The signal-to-noise ratio (SNR) used to characterize magnetic resonance imaging (MRI) system [1]-[3] is adopted here. In microwave imaging, although so far there are no agreed upon metrics and methods for system SNR evaluation, some approaches have been suggested [4]-[5].

Usually, the noise analysis of a reconstruction method is performed using synthetic data, where noise is added to noise-free data [6]-[8]. The noise-free data can be obtained by analytical or numerical models, in which the computational errors are negligible.

In this chapter, noise analysis is performed on the fast quantitative reconstruction method introduced in Chapter 3. The study focuses on the impact of random noise on the reconstruction accuracy of the dielectric-property distribution in an OUT. Here, the simulation example of the F-shaped dielectric bar is used. The raw simulation data of the example is considered to be noise-free. Gaussian White Noise (GWN) with a specified SNR is added to it to obtain synthetic noisy data. Different sets of noisy data are obtained with different SNR levels and images are generated from them. The details of the noise-adding procedure are given later.

Also, experiments are carried out to acquire noisy measurement data using the planar raster-scanning system described in Chapter 2. Two dielectric cylinders in

lossy dielectric material are imaged and reconstructed using our fast quantitative reconstruction algorithm. The SNR of the practical imaging system is assessed over the sample frequency band as well. Acceptable quantitative results are obtained at relatively low SNR levels, indicating that the proposed imaging method is robust to noise.

4.2 NOISE STUDY WITH SIMULATED SYNTHETIC DATA

4.2.1 Adding Gaussian white noise to raw data

GWN is added to the raw data $S_n^{(m)}$ (n = 1, 2, …, N_s; m = 1, 2, …, N_f) with a specified SNR via the MATLAB function *awgn* [9]. According to the script [10], the function *awgn* firstly calculates the signal power as

$$P_\mathrm{s}^{(m)} = \frac{1}{N_\mathrm{s}} \sum_{n=1}^{N_\mathrm{s}} \left| S_n^{(m)} \right|^2 , \tag{4.1}$$

where $|\cdot|$ denotes the absolute value of a complex-valued signal $S_n^{(m)}$. $P_\mathrm{s}^{(m)}$ is used to determine the noise power $P_\mathrm{N}^{(m)}$ together with a specific SNR (linear value) by

$$P_\mathrm{N}^{(m)} = \frac{P_\mathrm{s}^{(m)}}{\mathrm{SNR}} . \tag{4.2}$$

Then, for each $S_n^{(m)}$, the respective noise $N_n^{(m)}$ is calculated by

$$N_n^{(m)} = \gamma \sqrt{P_\mathrm{N}^{(m)}} , \tag{4.3}$$

where γ is a random number that can be generated by the MATLAB function *randn*

[10]. Since the signals $S_n^{(m)}$ are complex, the $N_n^{(m)}$ is a complex number:

$$N_n^{(m)} = \left(\gamma_1 + \mathrm{i}\gamma_2\right)\sqrt{\frac{P_{\mathrm{s}}^{(m)}}{2}}, \tag{4.4}$$

where $\mathrm{i}^2 = -1$, while γ_1 and γ_2 are two random numbers.

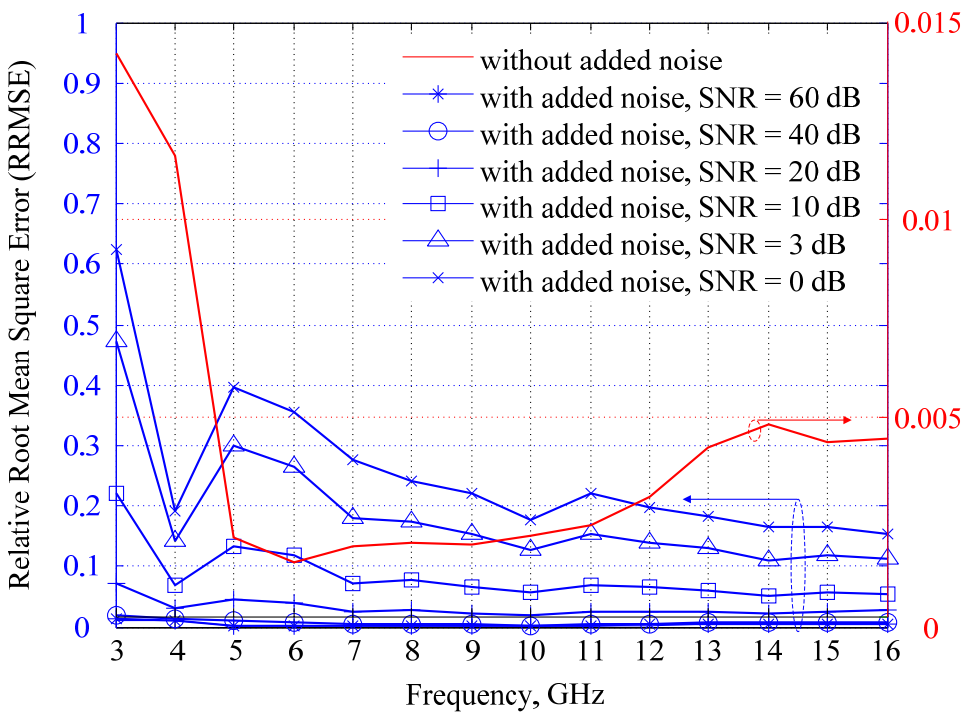

Fig. 4.1 The RRMSE of the LS solution for the complex permittivity distribution in the middle layer of the OUT using simulation data without and with GWN with SNR of 60 dB, 40 dB, 20 dB, 10 dB, 3 dB and 0 dB.

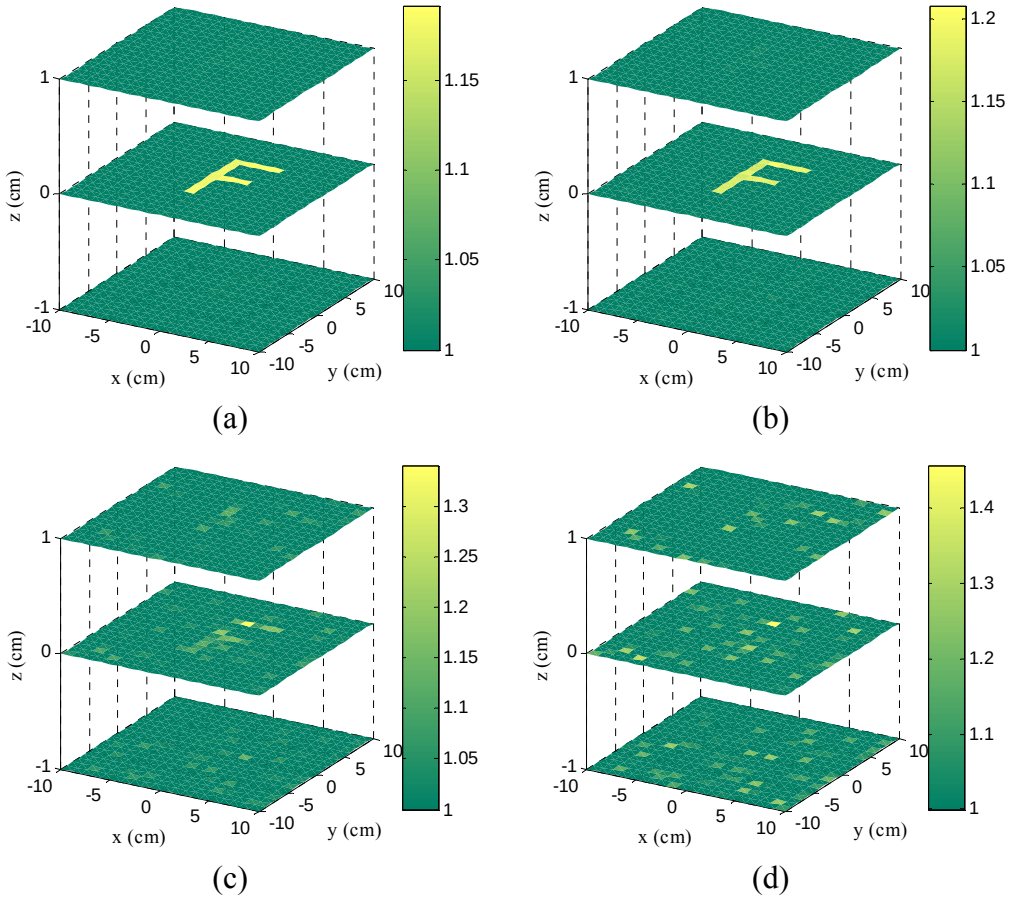

Fig. 4.2 LS solution for the real permittivity distribution (ε') of the OUT at 11 GHz using simulation data with GWN when the SNR is: (a) 60 dB, (b) 40 dB, (c) 20 dB, and (d) 10 dB.

4.2.2 Influence of random noise

Here, we continue with the example of the F-shaped dielectric bar in Section 3.7 of Chapter 3. Both the calibration and the test data (i.e., $\Delta S_{\mathrm{CO},p,n}^{(m)}$ and $\Delta S_{\mathrm{OUT},n}^{(m)}$) from simulations are used as the raw signals $S_n^{(m)}$, to which GWN is added. The SNR

level is set to 60 dB, 40 dB, 20 dB, 10 dB, 3 dB and 0 dB, respectively.

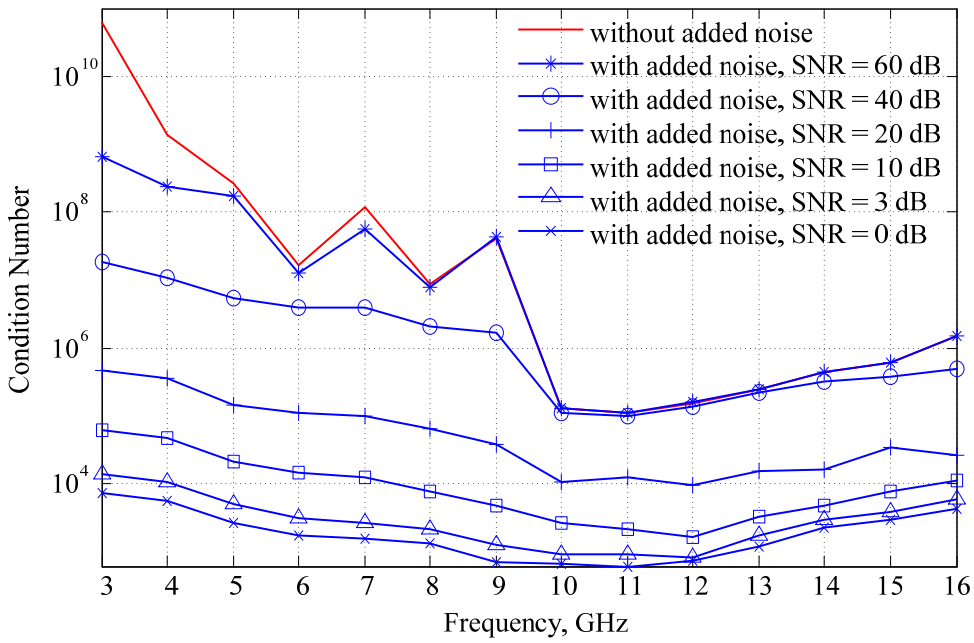

Fig. 4.3 The condition number of the system matrix of the LS problem in the simulation example without and with GWN of SNR equal to 60 dB, 40 dB, 20 dB, 10 dB, 3 dB and 0 dB.

Fig. 4.1 shows the RRMSE (relative root mean square error defined in Chapter 3) of the LS solutions obtained using the data with and without noise, respectively. It is obvious that the RRMSE becomes worse in the presence of noise. As expected, as the SNR decreases, the RRMSE increases significantly. Fig. 4.2 gives an example of the real permittivity estimate at 11 GHz as affected by the GWN at SNR levels of 60 dB, 40 dB, 20 dB and 10 dB, respectively. It is observed that

accurate results can still be obtained with SNR = 40 dB; however, at and below SNR = 20 dB, the image quality deteriorates dramatically.

Further, the condition number $\kappa\left[\boldsymbol{M}^{(m)}\right]$ of the system matrix $\boldsymbol{M}^{(m)}$ of the LS problem, see (3.19) in Chapter 3, is investigated when the noise-free and noisy data are used. The condition number $\kappa\left[\boldsymbol{M}^{(m)}\right]$ indicates the ill-posedness of the system matrix $\boldsymbol{M}^{(m)}$ as well as the uniqueness of the problem. When the system matrix $\boldsymbol{M}^{(m)}$ is well-posed, the condition number $\kappa\left[\boldsymbol{M}^{(m)}\right]$ is close to 1 and the problem has a unique solution. Otherwise, $\kappa\left[\boldsymbol{M}^{(m)}\right]$ is greater than 1 and the freedom of the problem increases as $\kappa\left[\boldsymbol{M}^{(m)}\right]$ is growing. Fig. 4.3 shows $\kappa\left[\boldsymbol{M}^{(m)}\right]$ versus frequency for different SNR levels. The conditioning of the system matrix improves as the SNR decreases; however, this does not lead to better image quality. See Fig. 4.1 where the RRMSE increases as the SNR decreases.

In order to understand this system matrix behavior, we rewrite the LS problem of (3.19) by taking the noise into account, i.e.,

$$\left[\boldsymbol{M}^{(m)} + \tilde{\boldsymbol{N}}^{(m)}\right]\boldsymbol{\tau}^{(m)} = \left[\boldsymbol{m}^{(m)} + \tilde{\boldsymbol{n}}^{(m)}\right] \tag{5}$$

where $\tilde{\boldsymbol{N}}^{(m)}$ is a matrix which is due to the noise in the CO measurements and $\tilde{\boldsymbol{n}}^{(m)}$ is a vector due to the noise in the OUT measurements. Here, $\boldsymbol{M}^{(m)}$ and $\boldsymbol{m}^{(m)}$ represent noise-free data.

As discussed in Section 3.4 in Chapter 3, $\boldsymbol{M}^{(m)}$ is better conditioned when the frequency increases since the diagonal elements become increasingly dominant. This can also be observed in Fig. 4.3 where $\kappa\left[\boldsymbol{M}^{(m)}\right]$ decreases with increasing frequency up until 11 GHz. In contrast, at low frequencies (large wavelengths), all elements in $\boldsymbol{M}^{(m)}$ become similar due to the loss of resolution. As a result, $\kappa\left[\boldsymbol{M}^{(m)}\right]$ approaches infinity. In this situation, the addition of noise through $\tilde{\boldsymbol{N}}^{(m)}$ improves the conditioning of (5) by introducing differences in the matrix element; however, this does not improve the image quality since the original data has been corrupted by the noise.

When the SNR is poor, the image quality might be improved by using regularization techniques, e.g., Tikhonov regularization [11]. This will be observed in the following experimental example.

4.3 RECONSTRUCTION OF TWO DIELECTRIC CYLINDERS IN LOSSY DIELECTRIC MATERIAL USING EXPERIMENTAL DATA

4.3.1 Experiment setup and imaging results

The experiment is performed with the planar raster-scanning system as shown in Fig. 2.2 of Chapter 2. The receiver is equipped with an electronically switched antenna array of 9 bow-tie elements. The array has 5 bow-tie elements polarized along x and

4 polarized along y. The Tx antenna is a TEM horn [12] polarized long x. The distance between the top and the bottom scanning planes is about 6 cm. Both the Rx and Tx antennas are at a distance of less than 2 mm from the object's surface. Together with the imaged object, the Tx and Rx antennas form a 10-port microwave network allowing for the measurement of 9 transmission S-parameters at each sampling location. Measurements are also performed with the imaged object flipped over, which is equivalent to switching the Tx and Rx locations. Thus, the total number of acquired signals at each sample point is N_s = 18. The frequency sweep employs N_f = 86 equally spaced sampling points from 3 GHz to 8.95 GHz.

The RO, the CO and the OUT are the same as that of the example in Section 2.3.5.1; see Fig. 2.10. The RO in the example is made of 5 absorber sheets [13], each of which has the dimensions of 20 cm × 20 cm × 1 cm. The CO is the same as the RO except that a dielectric cylinder [13] is inserted in the center of the middle layer of the RO. The dielectric cylinder has a diameter of 1 cm and a height of 1 cm. The complex relative permittivities of the absorber sheets and the dielectric cylinders are $10-\mathrm{i}5$ and $15-\mathrm{i}0.003$, respectively. Both of these values are averaged over the band of interest. The dispersion of these materials is negligible. In the OUT, two dielectric cylinders are inserted in the middle layer. The cylindrical inclusions have the same size and properties as those of the scatterer in the CO. They are placed next to each other at an edge-to-edge distance of 1 cm, which is roughly equal to the anticipated spatial resolution. The imaged area is a square of 5.5 cm × 5.5 cm.

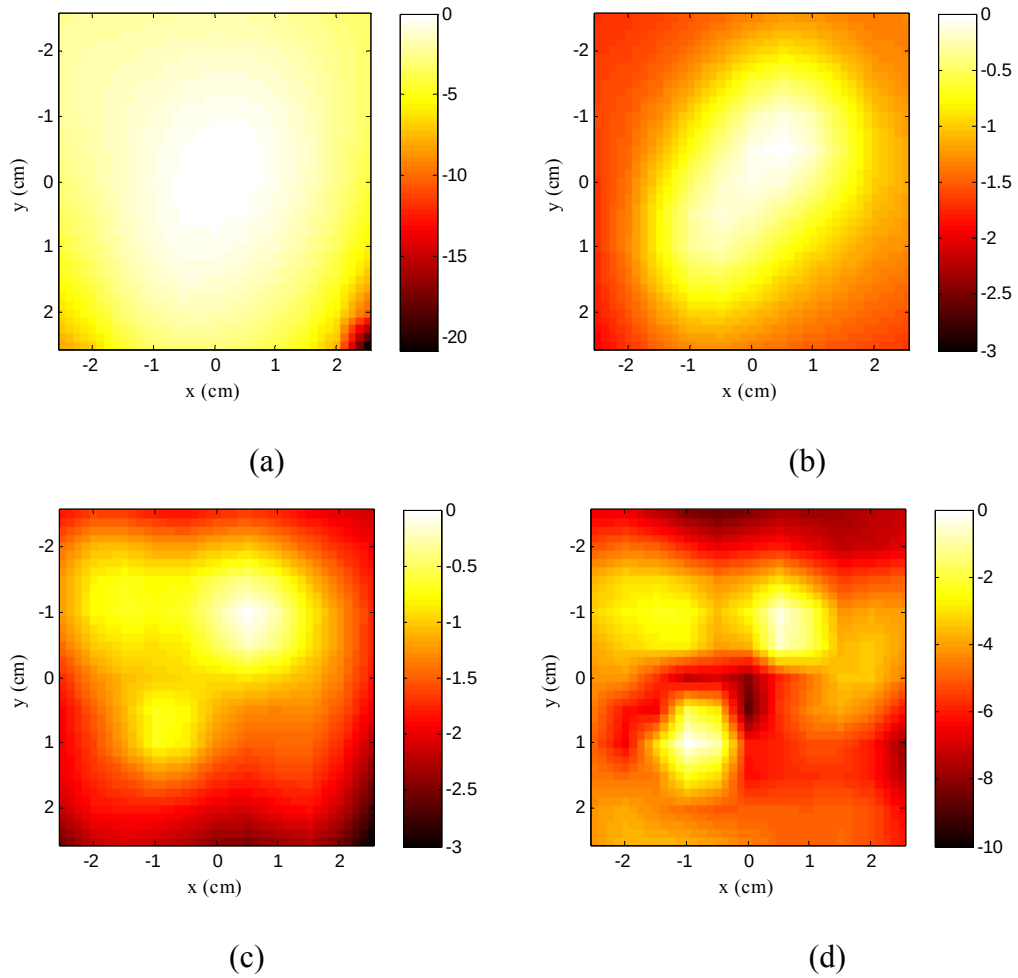

Fig. 4.4 Normalized magnitude plots (in dB) of the power maps for the middle layer of the OUT in the experiment at: (a) 3.56 GHz, (b) 5.03 GHz, (c) 6.43 GHz, (d) 8.25 GHz.

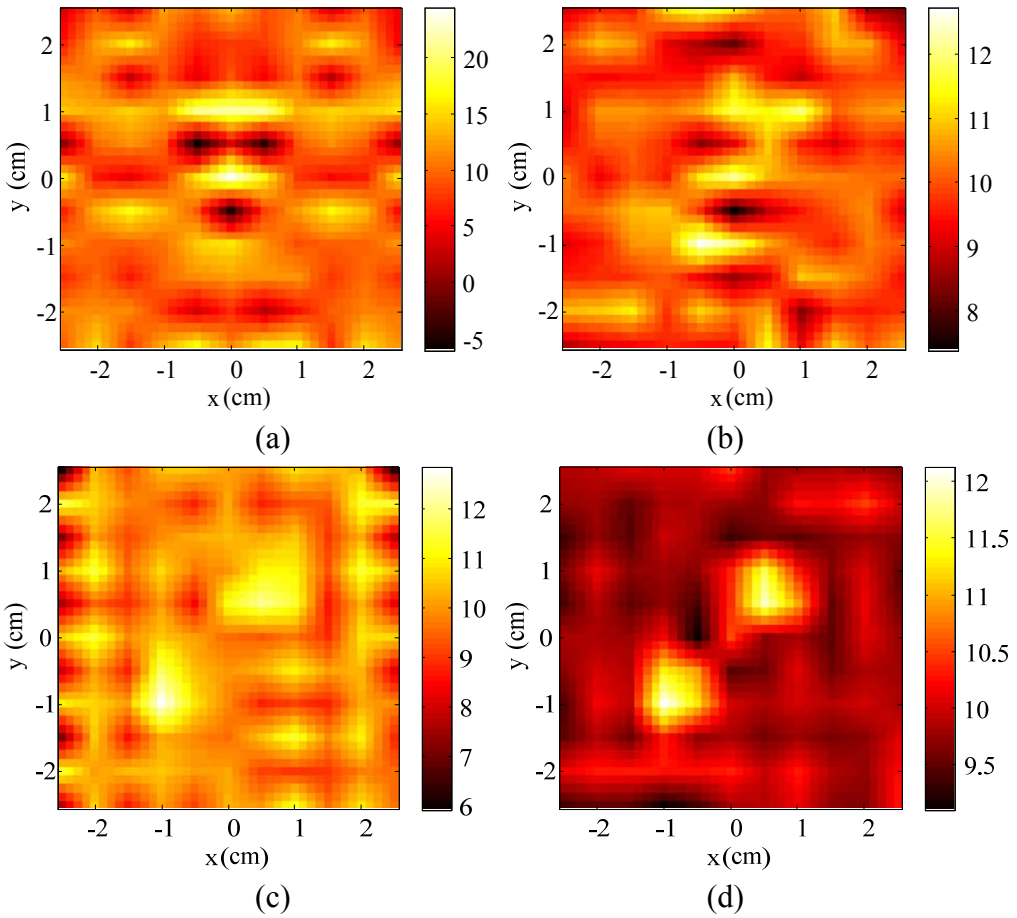

Fig. 4.5 LS solution of the real permittivity distribution (ε') for the middle layer of the object under test (OUT) at: (a) 3.56 GHz, (b) 5.03 GHz, (c) 6.43 GHz, (d) 8.25 GHz.

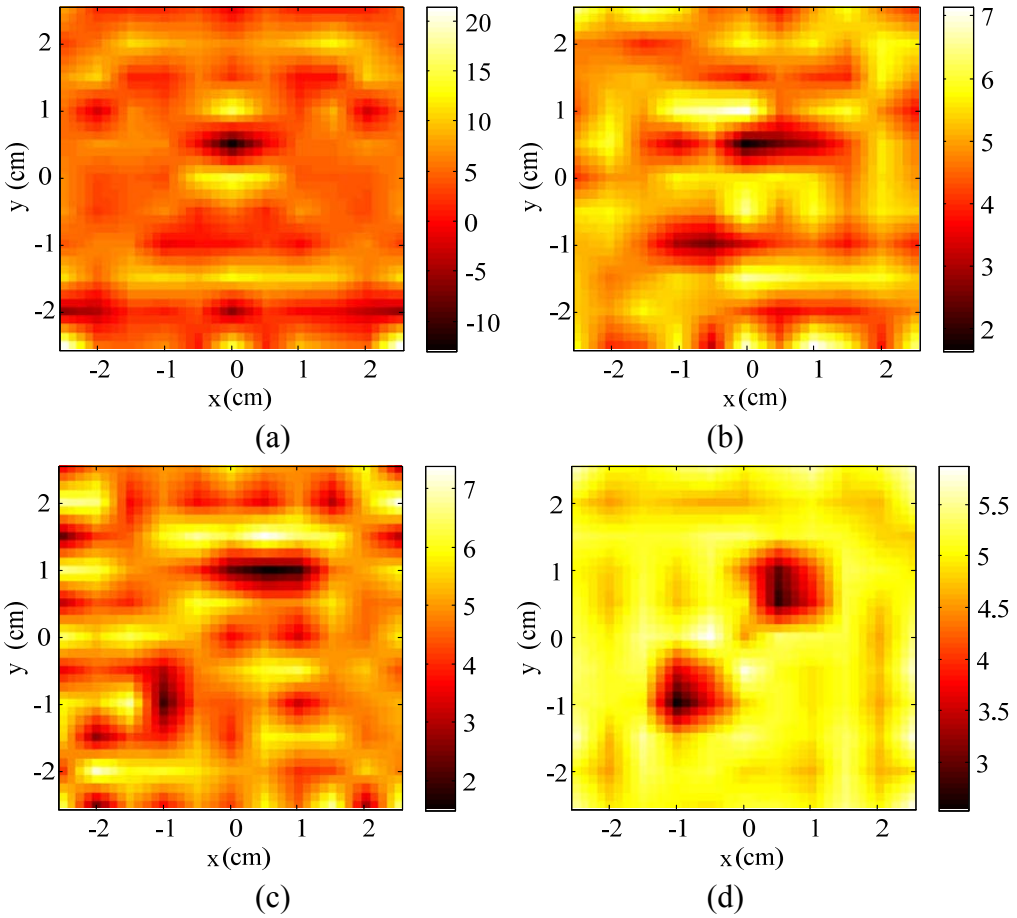

Fig. 4.6 LS solution of the imaginary permittivity distribution (ε'') for the middle layer of the object under test (OUT) at sample frequencies: (a) 3.56 GHz, (b) 5.03 GHz, (c) 6.43 GHz, (d) 8.25 GHz.

In this example, 3D images cannot be generated due to limitations of the hardware, which is incapable of acquiring the reflected signals. As discussed in Section 2.4 of Chapter 2, with planar raster scanning, the lack of reflected signals leads to loss of range resolution. Here, only the 2D results for the middle layer of the OUT are presented.

Fig. 4.4 shows the normalized magnitude plots (in dB) of the power maps for the middle layer of the OUT at different frequencies. The two dielectric cylinders embedded in the middle layer are clearly detected. As the frequency increases, the cross-range resolution improves significantly. It has been attempted to reconstruct the OUT by using a simulated resolvent kernel, computed from the incident field distributions [6][8] associated with each of the antennas in the simulation model of the experiment. This attempt failed, i.e., the obtained power maps did not show the targets. This failure is due to the inability of the model to represent adequately the complexities of the experiment despite the fact that the computations are extremely demanding.

Fig. 4.5 shows the LS solutions for the real permittivity distribution (ε') in the middle layer of the OUT at some sample frequencies. Fig. 4.6 shows the respective plots of the imaginary permittivity distributions (ε''). At low frequencies, e.g., 3.56 GHz and 5.03 GHz, the LS solution fails to localize and quantify the dielectric cylinders although the estimate of the background medium is on average close to the real background complex permittivity. As the frequency increases, see Fig. 4.5(c)

and (d) as well as Fig. 4.6(c) and (d), the accuracy of the LS solutions improves. The two cylinders are well localized and their permittivity estimated is to be around $12-i2$ (the true value is $15-i0.003$). At this stage, no regularization has been employed.

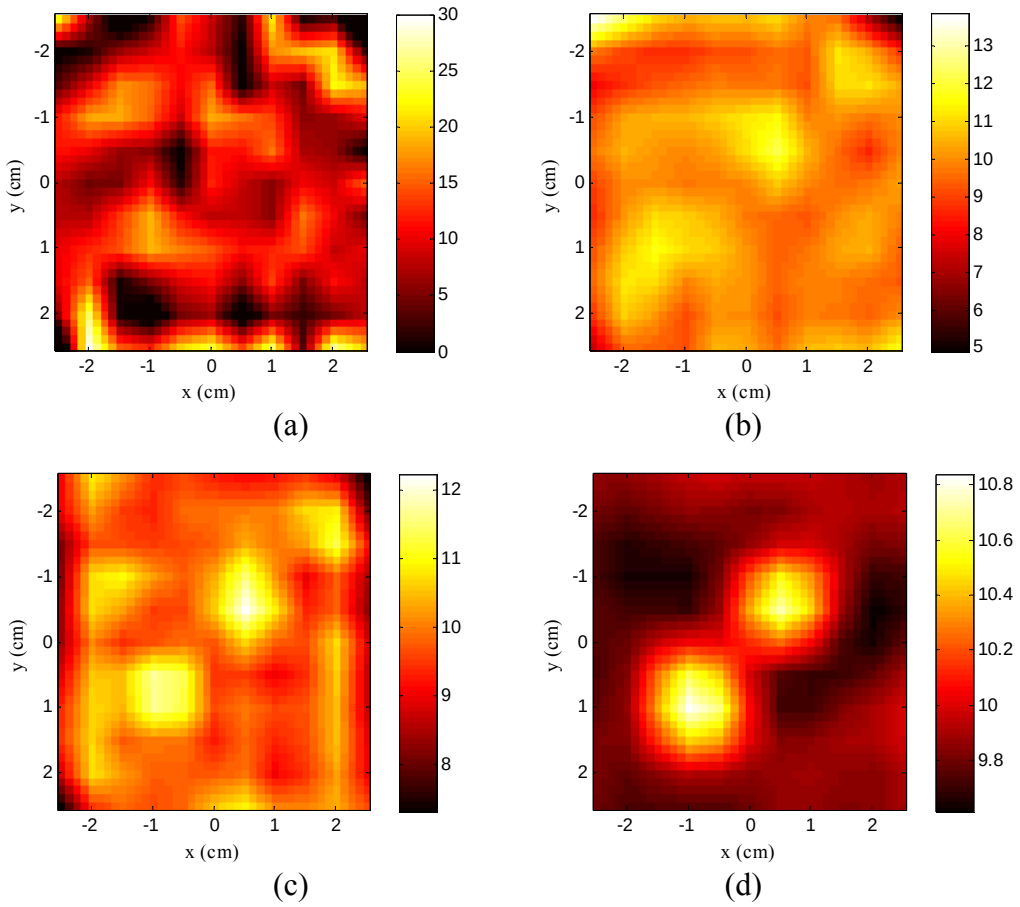

Fig. 4.7 LS solution of the real permittivity distribution (ε') for the middle layer of the object under test (OUT) at: (a) 3.56 GHz, (b) 5.03 GHz, (c) 6.43 GHz, (d) 8.25 GHz. Tikhonov regularization is applied.

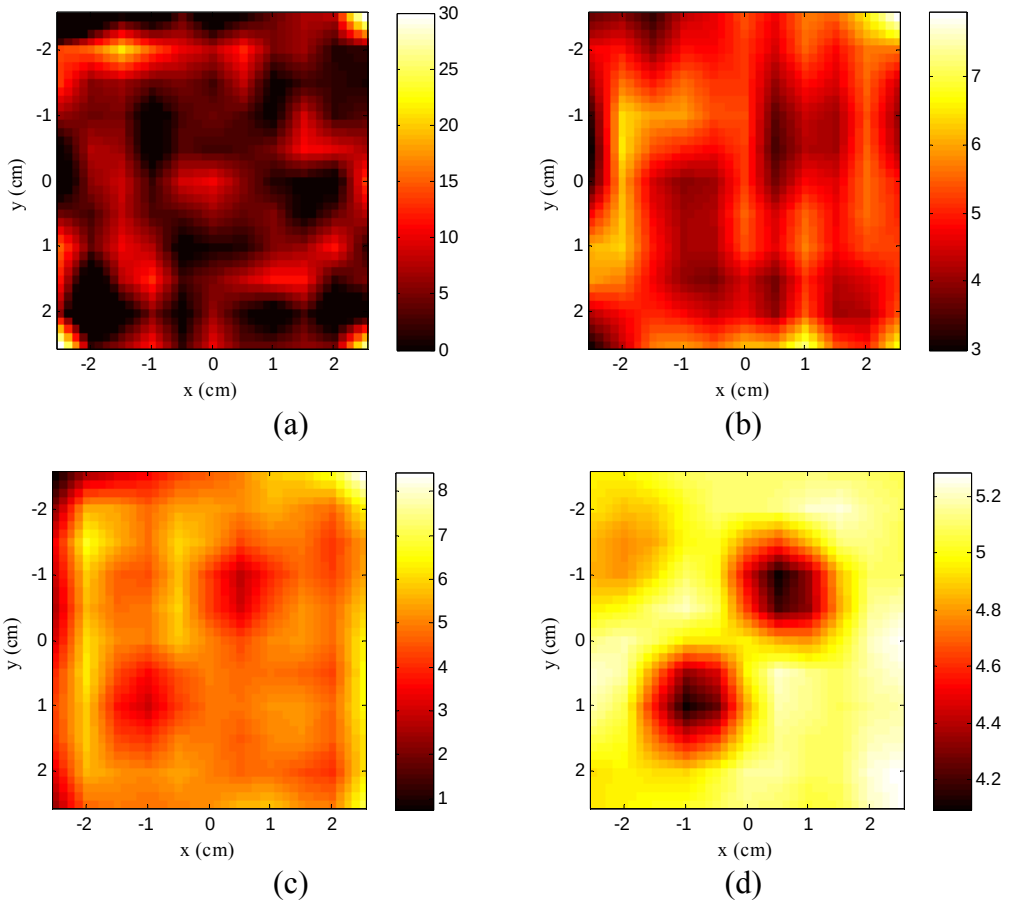

Fig. 4.8 LS solution of the imaginary permittivity distribution (ε'') for the middle layer of the object under test (OUT) at: (a) 3.56 GHz, (b) 5.03 GHz, (c) 6.43 GHz, (d) 8.25 GHz. Tikhonov regularization is applied.

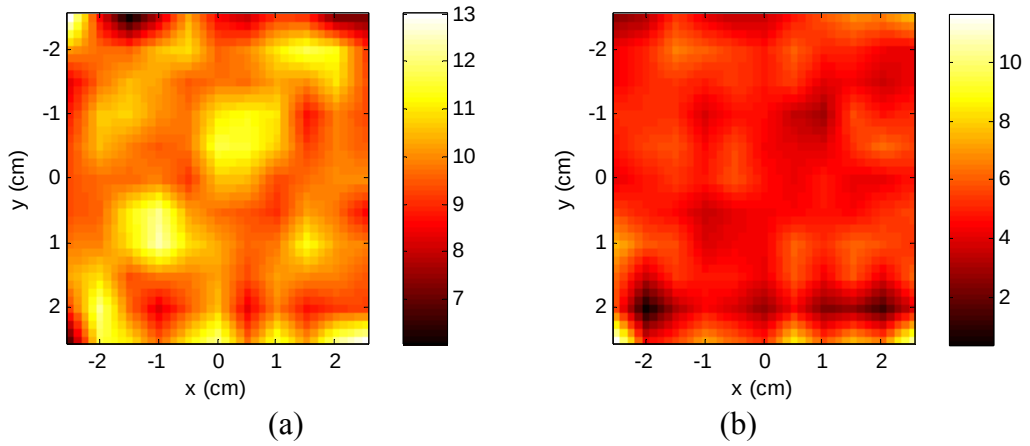

Fig. 4.9 LS solution of the complex permittivity distribution for the middle layer of the OUT using multi-frequency combination: (a) the real permittivity distribution (ε') and (b) the imaginary permittivity distribution (ε''). Tikhonov regularization is applied.

Fig. 4.7 and Fig. 4.8 show the LS solutions for the real permittivity distribution and the imaginary permittivity distribution in the middle layer of the OUT, respectively, when Tikhonov regularization is applied with the regularization parameter of 0.001. It is worth mentioning that, without regularization, the LS solution fails to localize and quantify the dielectric cylinders at low frequencies, e.g., 3.56 GHz and 5.03 GHz; see Fig. 4.5(a) and (b) as well as Fig. 4.6(a) and (b). With regularization, acceptable estimates are obtained at more sample frequencies; see Fig. 4.7(b) and Fig. 4.8(b). At some frequencies, the two cylinders are not only well localized but also their estimated permittivity is closer to the true value of

$15-\mathrm{i}0.003$; e.g., see Fig. 4.7(c) as well as Fig. 4.8(c). In both cases, the estimated permittivities of the dielectric cylinders and the background medium are about $12.5-\mathrm{i}2$ and $10-\mathrm{i}5$.

Fig. 4.9 shows the images generated by further applying the proposed multi-frequency combination; see Section 3.6C in Chapter 3. Given the true properties of the dielectric targets and the background medium, the overall-frequency results are obviously better than those at most single frequencies, e.g., see Fig. 4.7(a) and Fig. 4.8(b).

4.3.2 SNR evaluation of experimental data

The experimental signals contain noise caused by many factors, e.g., mechanical vibrations and uncertainties in the positioning, electronic noise of the instruments (the VNA), electromagnetic interference, other wireless signals, etc. The SNR of the measured data are calculated from the data acquired with the RO, which is the SNR of the planar raster-scanning system. Assume that at the m-th sample frequency there is a total of N_s acquired signals $S_{\mathrm{RO},n}^{(m)}$, where n = 1, 2, …, N_s. The mean signal $\overline{S}_\mathrm{RO}^{(m)}$ is calculated as

$$\overline{S}_\mathrm{RO}^{(m)} = \frac{1}{N}\sum_{n=1}^{N_\mathrm{s}} S_{\mathrm{RO},n}^{(m)} \tag{4.6}$$

and the mean signal power $P_\mathrm{s}^{(m)}$ is evaluated by

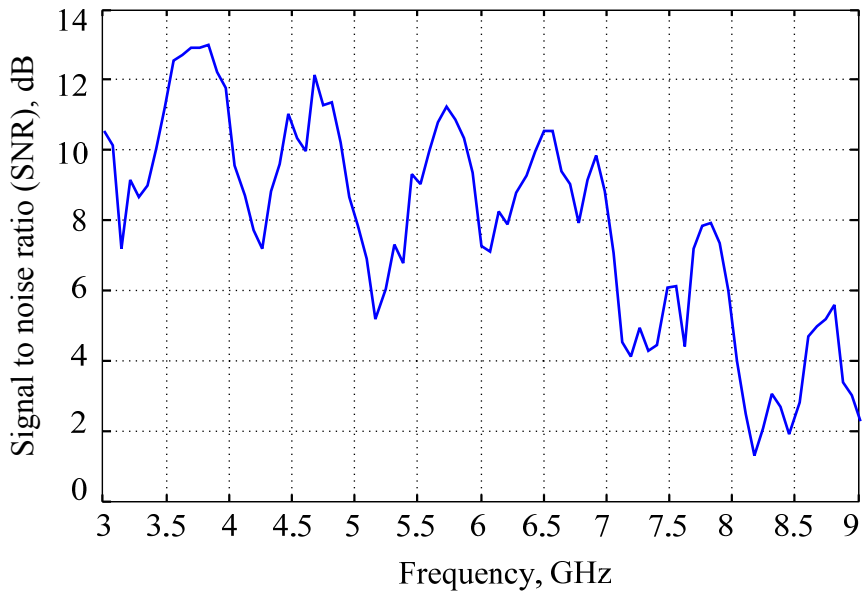

Fig. 4.10 The averaged SNR for the 9 channels of the planar raster-scanning system used in the experiment.

$$P_{\mathrm{s}}^{(m)} = \frac{1}{N}\sum_{n=1}^{N_{\mathrm{s}}}\left|S_{\mathrm{RO},n}^{(m)}\right|^2 \tag{4.7}$$

where $|\cdot|$ is the absolute value. On the other hand, the mean noise power $P_{\mathrm{N}}^{(m)}$ is obtained by

$$P_{\mathrm{N}}^{(m)} = \frac{1}{N_{\mathrm{s}}}\sum_{n=1}^{N_{\mathrm{s}}}\left|S_{\mathrm{RO},n}^{(m)} - \overline{S}_{\mathrm{RO}}^{(m)}\right|^2 . \tag{4.8}$$

Finally, the desired system SNR is calculated as

$$\mathrm{SNR}^{(m)} = \frac{P_{\mathrm{s}}^{(m)}}{P_{\mathrm{N}}^{(m)}} \tag{4.9}$$

and its dB value is given by

$$\mathrm{SNR}^{(m)} \text{ in dB} = 10\log_{10}\left(P_{\mathrm{s}}^{(m)} / P_{\mathrm{N}}^{(m)}\right). \tag{4.10}$$

Notice that the measurement data are complex numbers.

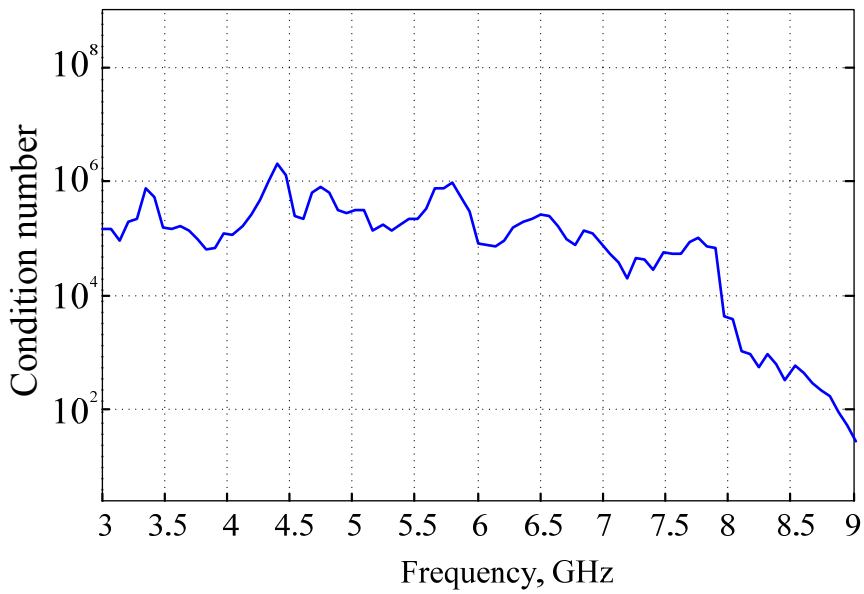

Fig. 4.11 The condition number of the system matrix of the LS problem using experimental data.

Fig. 4.10 shows the calculated averaged SNR for the 9 channels of the scanning system, which varies roughly from 2 dB to 13 dB over the frequency band and implies very low signal quality. This SNR is typical for the imaging in a lossy environment – a scenario which arises in applications such as tissue imaging, non-destructive testing and underground surveillance.

It is instructive to compare the imaging results of this experiment (with SNR levels roughly between 2 dB and 13 dB) with those in the simulation example in Section 3.7, where the simulated data have been corrupted by similar levels of noise (see Fig. 4.1 and Fig. 4.2). As is evident from Fig. 4.2(d), at SNR = 10 dB, the reconstruction in the simulation example fails completely—neither the location nor the permittivity of the object are recovered. Yet, in the experiment, which has similar or lower SNR, the targets are not only localized but also a fairly good estimate of the complex permittivity is obtained without regularization or constraints employed in the LS solution. This is mainly due to the fact that in the experiment we use nine Rx sensors with one Tx antenna allowing for the acquisition of 18 transmission coefficients at each frequency and sampling point (on both sides of the phantom). In contrast, the simulation setup employs two dipoles, each acting as both a Tx and an Rx antenna. This implies only 3 independent responses (taking into account reciprocity) at each sampling position and frequency. Increasing the number of independent responses is a well-known method to counteract the detrimental effects of noise; see e.g., [6][8].

Finally, Fig. 4.11 shows the condition number of the LS problem with the experimental data. Compared with the simulation example, see Fig. 4.3, similar trend with frequency can be observed. Namely, the conditioning of the system matrix improves as frequency increases. Also, compared with the averaged SNR curve in Fig. 4.10, the condition number appears to vary with frequency in accordance with

the averaged SNR. This illustrates one more time the impact of noise on the uniqueness and the ill-posedness of the LS problem.

4.4 CONCLUSIONS

The noise analysis is performed on the fast quantitative imaging method using both synthetic noisy data and experimental data. The synthetic noisy data are obtained by adding GWN to the simulation data with prescribed SNRs. The addition of GWN is summarized in details. The experimental data acquired from the practical scanning system inherently carries noise, which is due to the systematic and random errors. The SNR of the experimental data is calculated based on the evaluations of the signal and noise power levels. In both cases, it is observed that random noise dramatically affects the imaging quality as well as the uniqueness of the inverse problem. However, it also shows that the detrimental impact of noise can be efficiently counteracted by increasing the number of independent responses, e.g., increasing the numbers of sampling points and sensors, using multiple polarizations, etc.

REFERENCES

[1] L. Kaufman, D. M. Kramer, L. E. Crooks, and D. A. Ortendahl, “Measuring

signal-to-noise ratios in MR imaging," *Radiology*, vol. 173, no. 1, pp. 265−267, Oct. 1989.

[2] M. J. Firbank, A. Coulthard, R. M. Harrison, and E. D. Williams, "A comparison of two methods for measuring the signal to noise ratio on MR images," *Phys. Med. Biol.*, vol. 44, no. 12, pp. N261−N264, 1999.

[3] O. Dietrich, J. G. Raya, S. B. Reeder, M. F. Reiser, and S. O. Schoenberg, "Measurement of signal-to-noise ratios in MR images: influence of multichannel coils. Parallel imaging, and reconstruction filters," *J. Magn. Reson. Imaging*, vol. 26, no. 2, pp. 375−385, Aug. 2007.

[4] J. J. McCombe, "Noise reduction in microwave imaging and detection," M.A.Sc., Dept. Elect. Comput. Eng., McMaster Univ., Hamilton, ON, Canada, 2014.

[5] J. J. McCombe and N. K. Nikolova, "SNR assessment of microwave imaging systems," *IEEE AP-S/URSI Int. Symp. on Antennas and Propagation*, Memphis, TN, US, July 2014.

[6] L. Liu, A. Trehan, and N. K. Nikolova, "Near-field detection at microwave frequencies based on self-adjoint response sensitivity analysis," *Inverse Problems*, vol. 26, 105001, 2010.

[7] M. Ravan, R. K. Amineh, and N. K. Nikolova, "Two-dimensional near-field microwave holography," *Inverse Problems*, vol. 26, 055011, 2010.

[8] Y. Zhang, S. Tu, R. K. Amineh, and N. K. Nikolova, "Resolution and

robustness to noise of the sensitivity-based method for microwave imaging with data acquired on cylindrical surfaces," *Inverse Problems*, vol. 28, 115006, 2012.

[9] The MathWorks, MATLAB. Natick, MA, USA, Feb. 2010, [Online] http://www.mathworks.com/products/matlab

[10] "*MATLAB Help*" ver. 2010a. The MathWorks Inc., Natick, MA, USA, Feb. 2010.

[11] A. N. Tikhonov and V. Y. Arsenin, *Solutions of Ill-Posed Problems*, New York, NY: Wiley, 1977.

[12] R. K. Amineh, M. Ravan, A. Trehan, and N. K. Nikolova, "Near-field microwave imaging based on aperture raster scanning with TEM horn antennas," *IEEE Trans. Antennas Propag.*, vol. 59, no. 3, pp. 928−940, Mar. 2011.

[13] Emerson&Cuming Microwave Products, Inc., Randolph, MA, US.

Chapter 5

CONCLUSIONS

This thesis has presented an experimental calibration technique and a fast quantitative imaging method.

The merits of the proposed calibration technique include: (i) the automatic characterization of the imaging data-acquisition system via measurements, and (ii) the measurement-based forward model with high fidelity.

The proposed imaging method, which employs the aforementioned calibration technique, features the following advantages: (i) it is entirely measurement based, i.e., it does not need analytical or simulation-based forward models, (ii) it performs in real time, and (iii) it is quantitative.

In Chapter 2, the calibration technique is presented and explained with the employment of planar raster-scanning acquisition. The calibration measurements are performed on two known objects of the RO and the CO. With the implementation of coordinate translation, the total number of the calibration measurements can be kept at an acceptable level. The calibration procedure is first applied in sensitivity-based microwave imaging. Originally, the forward model in this method used to be

obtained by analytical approximations or simulations. With the proposed procedure, such approximate models are no longer needed as they are replaces by the measurement-based resolvent kernel of the scattering model. It is demonstrated that the sensitivity-based imaging method is enhanced by the proposed calibration technique. Also, in the last section of this chapter, the significance of the reflection signals for the imaging resolution has been emphasized and discussed.

In Chapter 3, the derivation of the fast quantitative imaging method is presented step by step. First, the concept of resolvent kernel extracted from calibration measurements is presented. Then the power maps as qualitative images are introduced followed by the generation of quantitative images. As the theoretical study suggests, the major limitation of the proposed method in its current form stems from neglecting the multiple scattering. The proposed imaging method performs the reconstruction in real space, i.e., without the need of Fourier transforms. When the examined object is highly heterogeneous, the method is able to provide a good initial estimate of the object's property distribution for iterative approach toward refinement.

In Chapter 4, synthetic noisy data and experimental data are used to perform the noise analysis of the proposed imaging method. A practical way to evaluate the SNR level of the measurement data is also presented. In the imaging results generated by noisy data, it is evident that the random noise increases the uniqueness of the inverse problem by decreasing the condition number of the system matrix.

However, the noise reduces the image quality dramatically. In the experimental example, the fast quantitative imaging method has exhibited good robustness to noise, which is mainly due to the use of multiple receiving antennas as opposed to single antenna in the measurement.

From the experience gained during the course of this work, the author suggests the following research topics to be addressed in future developments.

(1) Comparing the fast quantitative imaging method with other existing imaging methods (e.g., holography, diffraction tomography, synthetic aperture radar, etc.) in terms of inversion accuracy, spatial resolution, robustness to noise, and time requirements.

(2) Using spatial Fourier transform to avoid the coordinate translation in the calibration procedure. Instead, virtual translation in Fourier *k*-space can be implemented. Subsequently, the translated data in *k*-space can be transformed back to real (*x*-*y*) space using 2D inverse Fourier transform.

(3) Enhancing the fast quantitative imaging method employing iterative approaches to overcome the method limitations.

(4) Exploring imaging methods where there will be no need to measure the background medium, i.e., the RO.

(5) Developing an experimental model that is able to extract information about multiple scattering via measurements.

(6) Building rotating hemi-spherical or cylindrical switched-array acquisition systems to increase the number of signals and the viewing angles.

(7) Designing a miniature switched-array element with dual-polarization and a transmitting antenna with a wide illuminating aperture.

(8) Developing methods for noise evaluation of a microwave imaging system.

(9) Developing methods for noise suppression in the measurement data.

BIBLIOGRAPHY

M. G. Amin (Editor), *Through-the-Wall Radar Imaging*, Boca Raton, FL: CRC Press, 2011.

R. K. Amineh, A. Khalatpour, H. Xu, Y. Baskharoun, and N. K. Nikolova, "Three-dimensional near-field microwave holography for tissue imaging," *Int. J. Biomed. Imag.*, article ID 291494, 2012.

R. K. Amineh, M. Ravan, N. K. Nikolova, and A. Khalatpour, "Three-dimensional near-field microwave holography using reflected and transmitted signals," *IEEE Trans. Antennas Propag.*, vol. 59, no. 12, pp. 4777−4789, Dec. 2011.

R. K. Amineh, M. Ravan, A. Trehan, and N. K. Nikolova, "Near-field microwave imaging based on aperture raster scanning with TEM horn antennas," *IEEE Trans. Antennas Propag.*, vol. 59, no. 3, pp. 928−940, Mar. 2011.

R. K. Amineh, J. J. McCombe, A. Khalatpour, and N. K. Nikolova, "Microwave

holography using point-spread functions measured with calibration objects," IEEE Trans. Instrument. Meas., vol. 64, no. 2, pp. 403−417, Feb. 2015.

M. J. Burfeindt, N. Behdad, B. D. VanVeen, and S. C. Hagness, "Quantitative microwave imaging of realistic numerical breast phantoms using an enclosed array of multiband, miniaturized patch antennas," *IEEE Antennas Wireless Progag. Lett.*, vol. 11, pp. 1626−1629, Oct. 2012.

M. Bassi, M. Caruso, M. S. Khan, A. Bevilacqua, A.-D. Capobianco, and A. Neviani, "An integrated microwave imaging radar with planar antennas for breast cancer detection," *IEEE Trans. Microw. Theory Tech.*, vol. 61, no. 5, pp. 2108−2118, May 2013.

J. B. Campbell, *Introduction to Remote Sensing*, 3rd ed., New York: Guilford Press, 2002.

W. C. Chew, *Waves and Fields in Inhomogeneous Media*, New York: IEEE Press, 1995.

W. C. Chew and Y. M. Wang, "Reconstruction of two-dimensional permittivity distribution using the distorted Born iterative method," *IEEE Trans. Med. Imag.*, vol. 9, no. 2, pp. 218−225, June 1990.

A. J. Devaney, *Mathematical Foundations of Imaging, Tomography and Wavefield Inversion*, Cambridge UK: Cambridge University Press, 2012.

O. Dietrich, J. G. Raya, S. B. Reeder, M. F. Reiser, and S. O. Schoenberg, "Measurement of signal-to-noise ratios in MR images: influence of multichannel coils. Parallel imaging, and reconstruction filters," *J. Magn. Reson. Imaging*, vol. 26, no. 2, pp. 375−385, Aug. 2007.

M. S. Dadash, N. K. Nikolova, and J. W. Bandler, "Analytical adjoint sensitivity formula for the scattering parameters of metallic structures," *IEEE Trans. Microw. Theory Tech.*, vol. 60, no. 9, pp. 2713−2722, Sept. 2012.

Emerson&Cuming Microwave Products, Inc., Randolph, MA, US.

M. Elsdon, D. Smith, M. Leach, and S. J. Foti, "Experimental investigation of breast tumor imaging using indirect microwave holography," *Microw. Opt. Technol. Letters,* vol. 48, no. 3, pp. 480−482, Mar. 2006.

FEKO suite 6.0 EM Software & System, Inc. USA, www.feko.info

M. J. Firbank, A. Coulthard, R. M. Harrison, and E. D. Williams, "A comparison of two methods for measuring the signal to noise ratio on MR images," *Phys. Med. Biol.*, vol. 44, no. 12, pp. N261−N264, 1999.

E. C. Fear, X. Li, S. C. Hagness, and M. A., “Confocal microwave imaging for breast cancer detection: localization of tumors in three dimensions,” *IEEE Trans. Biomed. Eng.*, vol. 49, no. 8, pp. 812−822, Aug. 2002.

R. W. Y. Habash, *Bioeffects and Therapeutic Applications of Electromagnetic Energy*, Boca Raton, FL: CRC Press, 2008.

T. M. Habashy, R. W. Groom, and B. R. Spies, “Beyond the Born and Rytov approximations: a nonlinear approach to electromagnetic scattering,” *J. Geophys. Res.*, vol. 98, no. B2, pp. 1759−1775, Feb. 1993.

P. Kosmas and C. M. Rappaport, “Time reversal with the FDTD method for microwave breast cancer detection,” *IEEE Trans. Microw. Theory Tech.*, vol. 53, no. 7, pp. 2317−2323, July 2005.

P. Kosmas and C. M. Rappaport, “FDTD-based time reversal for microwave breast cancer detection-localization in three dimensions,” *IEEE Trans. Microw. Theory Tech.*, vol. 54, no. 4, pp. 1921−1927, Apr. 2006.

M. Klemm, I. J. Craddock, J. A. Leendertz, A. Preece, and R. Benjamin, “Radar-based breast cancer detection using a hemispherical antenna aray—experimental results,” *IEEE Trans. Antennas Propag.*, vol. 57, no.6, pp. 1692−1704, June 2009.

D. J. Kurrant and E. C. Fear, “An improved technique to predict the time-of-arrival of a tumor response in radar-based breast imaging,” *IEEE Trans. Biomed. Eng.*, vol. 56, no. 4, pp. 1200−1208, 2009.

L. Kaufman, D. M. Kramer, L. E. Crooks, and D. A. Ortendahl, “Measuring signal-to-noise ratios in MR imaging,” *Radiology*, vol. 173, no. 1, pp. 265−267, Oct. 1989.

S. Khorram, F. H. Koch, C. F. van der Wiele, and S. A. C. Nelson, *Remote Sensing*, Springer, 2012.

L. E. Larsen and J. H. Jacobi, *Medical Applications of Microwave Imaging*, New York: IEEE, 1986.

H. B. Lim, N. T. T. Nhung, P. E. Li, and N. D. Thang, “Confocal microwave imaging for breast cancer: delay-multiply-and-sum image reconstruction algorithm,” *IEEE Trans. Biomed. Eng.*, vol. 55, no. 6, pp. 1697−1704, June 2008.

L. Liu, A. Trehan, and N. K. Nikolova, “Near-field detection at microwave frequencies based on self-adjoint response sensitivity analysis,” *Inverse Problems*, vol. 26, 105001, 2010.

The MathWorks, MATLAB. Natick, MA, USA, Feb. 2010, [Online] http://www.mathworks.com/products/matlab

P. M. Meaney, M. W. Fanning, D. Li, S. P. Poplack, and K. D. Paulsen, “A clinical prototype for active microwave imaging of the breast,” *IEEE Trans. Microw. Theory Tech.*, vol. 48, no. 1, pp. 1841−1853, Nov. 2000.

J. J. McCombe and N. K. Nikolova, “SNR assessment of microwave imaging systems,” *IEEE AP-S/URSI Int. Symp. on Antennas and Propagation*, Memphis, TN, US, July 2014.

J. J. McCombe, “Noise reduction in microwave imaging and detection,” M.A.Sc., Dept. Elect. Comput. Eng., McMaster Univ., Hamilton, ON, Canada, 2014.

A. J. Nanzer, *Microwave and Millimeter-Wave Remote Sensing for Security Applications*, Norwood, MA: Artech House, 2011.

N. K. Nikolova, “Microwave imaging for breast cancer,” *IEEE Microw. Mag.*, vol. 12, no. 7, pp. 78−94, Dec. 2011.

N. K. Nikolova, “Microwave biomedical imaging,” *Wiley Encyclopedia of Electrical and Electronics Engineering*, pp. 1−22, Apr. 2014.

N. K. Nikolva, X. Zhu, Y. Song, A. Hasib, and M. H. Bakr, “*S*-parameter sensitivities for electromagnetic optimization based on volume field solutions,” *IEEE Trans. Microw. Theory Tech.*, vol. 57, no. 6, pp. 1526−1538, June 2009.

M. Ostadrahimi, P. Mojabi, C. Gilmore, A. Zakaria, S. Noghanian, S. Pistorius, and J. LoVetri, "Analysis of incident field modeling and incident/scattered field calibration techniques in microwave tomography," *IEEE Antennas Wireless Progag. Lett.*, vol. 10, pp. 900−903, Sept. 2011.

M. Ostadrahimi, A. Zakaria, J. LoVetri, and L. Shafai, "A near-field dual polarized (TE-TM) microwave imaging system," *IEEE Trans. Microw. Theory Tech.*, vol. 61, no. 3, pp. 1376−1384, Mar. 2013.

D. M. Pozar, *Microwave Engineering*, 2nd ed., Hoboken, NJ: John Wiley & Sons, Inc., 1998.

M. Pastorino, *Microwave Imaging*, Hoboken, NJ: John Wiley & Sons, Inc., 2010.

K. D. Paulsen, P. M. Meaney, and L. C. Gilman (Eds.), *Alternative Breast Imaging: Four Model Based Approaches*, Springer, 2005.

M. Ravan, R. K. Amineh, and N. K. Nikolova, "Two-dimensional near-field microwave holography," *Inverse Problems*, vol. 26, 055011, 2010.

D. M. Sheen, D. L. McMakin, and T. E. Hall, "Three-dimensional millimeter-wave imaging for concealed weapon detection," *IEEE Trans. Microw. Theory Tech.*, vol. 49, no. 9, pp. 1581−1592, Sept. 2001.

D. Sheen, D. McMakin, and T. Hall, "Near-field three-dimensional radar imaging techniques and applications," *Applied Optics*, vol. 49, no. 19, pp. E83−E93, 2010.

Y. Song and N. K. Nikolova, "Memory-efficient method for wideband self-adjoint sensitivity analysis," *IEEE Trans. Microw. Theory Tech.*, vol. 56, no. 8, pp. 1917−1927, Aug. 2008.

T. Sakamoto, T. G. Savelyev, P. Aubry, and A. G. Yarovoy, "Fast range point migration method for weapon detection using ultra-wideband radar," *The 9th European Radar Conf. (EuRAD 2012)*, pp. 230−233, Oct. 2012.

T. G. Savelyev and A. G. Yarovoy, "Fast image by 3-D deconvolution in short-range UWB radar for concealed weapon detection," *The 9th European Radar Conf. (EuRAD 2012)*, pp. 26−29, Oct. 2012.

J. D. Taylor (Editor), *Ultra-wideband Radar Technology*, FL: CRC Press, Sept. 2000.

A. N. Tikhonov and V. Y. Arsenin, *Solutions of Ill-Posed Problems*, New York, NY: Wiley, 1977.

S. Tu, J. McCombe, D. S. Shumakov and N. K. Nikolova, "Fast quantitative microwave imaging with resolvent kernel extracted from measurements," *Inverse*

Problem, vol. 31, 045007, 2015.

S. Tu, Y. Zhang, J. J. McCombe, and N. K. Nikolova, "Sensitivity-based quantitative imaging using planar raster scanning," *IEEE AP-S/URSI Int. Symp. on Antennas and Propagation*, Memphis, TN, US, July 2014.

S. Tu, Y. Zhang, J. J. McCombe, and N. K. Nikolova, "Sensitivity-based reconstruction in microwave imaging using near-field calibration measurements," *European Microwave Conference (EuMC) 2014*, Rome, Italy, Oct. 2014.

I. Walterscheid, A. R. Brenner, and J. H. G. Ender, "Results on bistatic synthetic aperture radar," *IEEE Electron. Lett.*, vol. 40, no. 19, pp. 1224−1225, 2004.

Y. M. Wang and W. C. Chew, "An iterative solution of the two-dimensional electromagnetic inverse scattering problem," *Int. J. Imag. Syst. Technol.*, vol. 1, no. 1, pp. 100−108, Feb. 1989.

C. Yu, M. Yuan, Y. Zhang, J. Stang, R. T. George, G. A. Ybarra, W. T. Joines, and Q. H. Liu, "Microwave imaging in layered media: 3-D image reconstruction from experimental data," *IEEE Trans. Antennas Propag.*, vol. 58, no. 2, pp. 440−448, Feb. 2010.

R. Zoughi, *Microwave Non-destructive Testing and Evaluation*, Dordrecht, The

Netherlands: Kluwer Academic, 2000.

M. S. Zhdanov and S. Fang, “Quasi-linear approximation in 3-D electromagnetic modeling,” *Geophysics*, vol. 61, no. 3, pp. 646−645, May 1996.

M. S. Zhdanov and Sheng Fang, “Three-dimensional quasi-linear electromagnetic inversion,” *Radio Sci.*, vol. 31, no. 4, pp. 741−754, July 1996.

M. Zhdanov and G. Hursan, “3D electromagnetic inversion based on quasi-analytical approximation,” *Inverse Problems*, vol. 16, pp. 1297−1322, 2000.

Y. Zhang, S. Tu, R. K. Amineh, and N. K. Nikolova, “Sensitivity-based microwave imaging with raster scanning,” *2012 IEEE MIT-S Int. Microw. Symp. Dig.*, pp. 1-3, June 2012.

Y. Zhang, S. Tu, R. K. Amineh and N. K. Nikolova, “Resolution and robustness to noise of the sensitivity-based method for microwave imaging with data acquired on cylindrical surfaces,” *Inverse Problems*, vol. 28, 115006, 2012.